THREE-DIMENSIONAL NONEQUILIBRIUM VISCOUS SHOCK-LAYER FLOW OVER THE SPACE SHUTTLE ORBITER

by

Moo Do Kim

Dissertation submitted to the Faculty of the
Virginia Polytechnic Institute and State University
in partial fulfillment of the requirements for the degree of
DOCTOR OF PHILOSOPHY
in
Aerospace Engineering

APPROVED:

Clark H. Lewis

Joseph A. Schetz

A. K. Jakubowski

W. L. Neu

K. B. Hannsgen

May, 1983
Blacksburg, Virginia

THREE-DIMENSIONAL NONEQUILIBRIUM VISCOUS SHOCK-LAYER FLOW OVER THE SPACE SHUTTLE ORBITER

by

Moo Do Kim

(ABSTRACT)

A numerical method has been developed to predict the three-dimensional nonequilibrium flowfield past the space shuttle orbiter at high angles-of-attack (up to 50-deg). An existing viscous shock-layer method for perfect gas flows has been extended to include finite-rate chemical reactions of multi-component ionizing air. A general nonorthogonal computational grid system was introduced to treat the nonaxisymmetric geometry. At shuttle reentry flight conditions, nonequilibrium real gas effects on the surface-measurable quantities are significant. Computational solutions have been obtained for chemically reacting flowfields over the entire windward surface of the space shuttle orbiter at high angles-of-attack. Boundary conditions studied include noncatalytic wall, finite-catalytic wall, fully-catalytic wall, and nonequilibrium slip conditions at the wall and/or shock. The nonequilibrium solutions with a finite-catalytic wall are compared to both fully-catalytic and noncatalytic wall solutions. The present solutions are also compared to chemical equilibrium air solutions, perfect gas solutions, and

the shuttle flight heating and pressure data. The comparisons show good agreement and correlations with flight-derived surface heat-transfer and pressure distributions. Three-dimensional effects are clearly shown in the flight-derived data for the first time based upon the results of this study.

ACKNOWLEDGEMENTS

First of all, the author wishes to express his deep appreciation to Dr. Clark H. Lewis, his major advisor, for conceiving, directing and supporting this research, and also for his incessant guidance, corrections and abundant computational-facility support throughout the period.

The author also expresses his thanks to Dr. Joseph A. Schetz, Dr. A. K. Jakubowski, Dr. W. L. Neu and Dr. K. B. Hannsgen for their review and comments on this thesis, their previous efforts for the author's fellowship awards, and also serving as members of the advisory committee.

In particular, thanks are due to Mrs. Joyce Lewis for her various administrative help and kind concern for his graduate study. Thanks are also due to S. Swaminathan for his valuable help and technical discussions during this research work. Finally the author is sincerely grateful to his wife, Younghee, for her understanding, patience and encouragement throughout the period.

TABLE OF CONTENTS

Appendix

LIST OF TABLES

LIST OF FIGURES

NOMENCLATURE

C_i	concentration of species i, ρ_i/ρ
C_p	specific heat at constant pressure
D_i	binary diffusion coefficient, $D_i^* \rho_\infty / \mu_{ref}$
FINCAT	nonequilibrium solution with finite-catalytic wall
FULCAT	nonequilibrium solution with fully-catalytic wall
g	determinant of coordinate metric tensor
g^i	vector orthogonal to g_j and g_k
g^{ij}	coordinate metric tensor, $g^i \cdot g^j$; i,j = 1,2,3
g_{ij}	coordinate metric tensor, $g_i \cdot g_j$; i,j = 1,2,3
$\underline{g}_1$	vector in streamwise (ξ_1) direction
$\underline{g}_2$	vector in normal (ξ_2) direction
$\underline{g}_3$	vector in circumferential (ξ_3) direction
h	static enthalpy, h^*/U_∞^2
H	total enthalpy, H^*/U_∞^2
k	thermal conductivity, $k^*/(\mu_{ref} C_{p\infty})$
k_{fr}	forward reaction rate constant
k_{br}	backward reaction rate constant
k_w	surface catalytic recombination rate
L	shuttle body total length (32.84 m)
Le_i	Lewis number, $C_p^* \rho^* D_i^*/k^*$
M_i	species molecular weight
$\bar{M}$	mixture molecular weight, $1/(\Sigma C_i/M_i)$
M_∞	freestream Mach number

n_{sh}	shock stand-off distance, n_{sh}^*/R_n
NJ	number of species plus catalytic third bodies, NS+NZ
NR	number of chemical reaction
NS	number of species
NZ	number of catalytic third bodies
NONCAT	nonequilibrium solution with noncatalytic wall
NONEQL	nonequilibrium flow solution
NSH	shock stand-off distance, n_{sh}^*/R_n
p	pressure, $p^*/(\rho_\infty U_\infty^2)$
p_i	partial pressure of species i
PG	denotes perfect gas solution
PHI	same as ϕ in cylindrical coordinates
Pr	Prandtl number, $C_p^* \mu^*/k^*$
PW/PINF	p_w^*/p_∞
QW	heating rate due to conduction and diffusion, MW/m^2
R	universal gas constant
Re_∞	freestream unit Reynolds number, m^{-1}
R_n	dimensional shuttle nose radius, 62.23 cm (24.5 in)
SHTNEQ	shuttle-nonequilibrium, the present numerical method
STS	space transportation system
S/RN	surface distance along body nondimensionalized by R_n
T	temperature, T^*/T_{ref}
T_{ref}	dimensional reference temperature, $U_\infty^2/C_{p\infty}$
t	shuttle entry time from 122 km altitude interface
u,v,w	streamwise, normal and circumferential velocity

tensor components nondimensionalized by U_∞

U_∞	dimensional freestream velocity
U/UINF	streamwise velocity, u^*/U_∞
$\underline{V}$	local velocity vector
$\dot{w}_i$	species production term
Y/RN	distance in body-normal direction, ξ_2^*/R_n
z,r,ϕ	reference cylindrical coordinates
Z/L	axial distance along body divided by L, same as z/L
α	angle-of-attack, degree
α_{rj}	forward stoichiometric coefficients
β_{rj}	backward stoichiometric coefficients
ε	Reynolds number parameter, $\varepsilon^2=\mu_{ref}/(\rho_\infty U_\infty R_n)$
γ	ratio of specific heats
γ_i	catalytic recombination coefficient
θ	molecule-surface accommodation coefficient
μ	viscosity, μ^*/μ_{ref}
μ_{ref}	reference viscosity evaluated at T_{ref}
ϕ	cylindrical coordinate
ξ_1,ξ_2,ξ_3	body-generator computational coordinates
ξ,η,ζ	normalized computational coordinates
ρ	density, ρ^*/ρ_∞
σ	shock angle with respect to freestream velocity vector

Superscript

*	dimensional quantity

(-) quantity normalized by shock value

Subscript

i	species i
ref	dimensional reference quantity
s	slip value at the edge of Knudsen layer
sh	value behind the shock
w	wall value
∞	dimensional freestream value

Chapter I

INTRODUCTION

Recently the nonequilibrium effects on the shuttle reentry flowfield have been widely investigated to reduce the surface heating by employing a proper surface material. Various numerical methods have been applied to solve the nonequilibrium viscous flowfield over the windward surface of the space shuttle during reentry. For instance, Miner and Lewis (Ref. 1) developed a two-dimensional nonequilibrium viscous shock-layer method and applied it to solve the flowfield on the windward symmetry plane of the space shuttle using an"equivalent axisymmetric body" concept. They followed the formulations of the nonequilibrium viscous shock-layer method by Davis (Refs. 2,3) and Moss (Ref. 4), and further extended for nonanalytic blunt bodies like the shuttle. Their solutions showed that their two-dimensional viscous shock-layer method using nonequilibrium multi-component ionizing air produced better predictions compared to the more approximate integral method for the thin viscous shock-layer equations. The equivalent axisymmetric body was obtained by taking the shuttle windward centerline and making a body of revolution around the wind axis which passes the physical stagnation point on the shuttle geometry at high angle-of-attack.

Shinn, Moss and Simmonds (Ref. 5) analyzed the effect of finite-catalytic wall on the heating rate along the shuttle windward symmetry plane using a two-dimensional nonequilibrium viscous shock-layer method. They also used the equivalent axisymmetric body concept. Their results indicate that the nonequilibrium effects persist throughout most of the shuttle entry heating pulse down to an altitude of approximately 50 km. The agreement between the flight data and their nonequilibrium (finite-catalytic wall) calculations using the extrapolated relations of Scott's recombination rates (Ref. 6) was good for the orbiter forward region but not as good for the aft region.

Rakich and Lanfranco (Refs. 7,8) used a more approximate axisymmetric analogue of a boundary-layer method to solve the nonequilibrium flow over the shuttle windward surface. The necessary boundary-layer edge conditions were provided from the inviscid Euler equations for chemically reacting air-flow around the shuttle. They also investigated the catalytic efficiency of the space shuttle heat shield using shuttle flight test data and arc-heated wind-tunnel experment, and they determined that the heat shield tiles are almost noncatalytic. The space shuttle, unlike most previous reentry vehicles, has a radiatively cooled thermal protection system (TPS). The lower surface of the shuttle is covered

with a light weight, rigidized fibrous ceramic with a glassy coating called reaction cured glass (RCG). This material is called high-temperature reusable-surface insulation (HRSI). If the surface is highly catalytic, dissociated air tends to recombine near the relatively cold wall (1400 K), and the released heat due to recombination substantially increases the surface heating. The current shuttle TPS, however, has a very low surface catalycity as verified by the experimental test results of Rakich et al. (Ref. 8).

Scott and Derry (Ref. 6) calculated the shuttle windward centerline heating using a method of combining three-dimensional inviscid flow solutions with reacting two-dimensional axisymmetric analogue boundary-layer calculations including the finite-catalytic wall effect. Temperature-dependent energy-transfer catalytic recombination coefficients measured by Scott for nitrogen and oxygen recombination on the HRSI coating were used as wall boundary conditions. They discussed some possible reasons for the overprediction of their calculated temperatures compared to the flight data on the forward part of the body. They also discussed possible effects of the actual three-dimensional geometry of the shuttle orbiter, overprediction in the arc-jet catalysis measurements due to contamination of the jet-flow, uncertainty in gas-phase reaction rates, and finally contamination of shuttle lower-surface due to the microphone-cap oxides.

However, none of the foregoing could solve the three-dimensional reacting viscous flowfield at high angle-of-attack without a major approximation like the axisymmetric analogue or the equivalent axisymmetic body concept.

The purpose of the present work is to develop a numerical method to predict the three-dimensional nonequilibrium viscous flowfield past general nonaxisymmetric bodies at high angles-of-attack (up to 50-deg), and accurately predict the three-dimensional nonequilibrium flowfield over the entire windward-surface of the space shuttle orbiter. The computational results obtained are compared with the flight heating rate and pressure data.

The present numerical method (SHTNEQ) has been developed based on the two-dimensional nonequilibrium flowfield code by Miner and Lewis (Ref. 1) and the three-dimensional perfect gas code by Szema and Lewis (Ref. 9). The three-dimensional viscous shock-layer equations for perfect gas flows have been extended to include finite-rate chemical reactions of multi-component ionizing air. It is assumed that the chemical reactions proceed at a finite rate, and a chemical model which includes seven species and seven reaction equations is used to calculate the rate of production terms. The reaction equations and reaction rate constants are taken

from Blottner (Ref. 10). A general nonorthogonal computational grid system was introduced to treat the nonaxisymmetric shuttle geometry. This coordinate system is similar to the one defined by Helliwell (Ref. 11), except that the second coordinate ξ_2 of the present system is a straight line in the body-normal direction. The three velocity components are tensor quantities and are defined in the nonorthogonal coordinate directions. Since the viscous shock-layer equations are parabolic in both the streamwise and crossflow directions, the equations are solved by a highly efficient finite-difference scheme given by Murray and Lewis (Ref. 12), which requires much less computing time than PNS or time-dependent methods. The present method can solve both subsonic and supersonic flows and requires the shock shape as input data. When the input shock is not accurate and the output shock is substantially different from the input shock, a global iteration is required to refine the final solution (once or twice in general). The shock shapes for the present shuttle calculations were provided by the inviscid HALIS method of Weilmuenster and Hamilton (Ref. 13).

It is known that the nonequilibrium real gas effects persist throughout a wide range of the shuttle reentry trajectory (altitudes of 122 to 50 km). In the present work, three points along the trajectory of the second space shut-

tle flight (STS-2) are chosen, and the numerical solutions are obtained over the entire windward surface of the body. Case 1 is for t = 250 sec of trajectory time counted from the entry interface, at an altitude of 85.74 km, with a Mach number of 26.6 and angle-of-attack of 41-deg. The next point for Case 2 is at t = 460 sec, altitude of 74.98 km, Mach number of 25.5 and angle-of-attack of 40-deg. The conditions for Case 3 are t = 650 sec, altitude of 71.29 km, Mach number of 23.4 and angle-of-attack of 39.4-deg. The nose radius used as reference length is 0.62318 m. Reynolds number parameter ε is 0.10766 for Case 1, 0.04394 for Case 2, and 0.03286 for Case 3. For each test case, computational predictions have been obtained for the following chemical models: (i) nonequlibrium air with finite-catalytic wall, (ii) nonequilibrium air with noncatalytic wall, (iii) nonequilibrium air with fully-catalytic wall, (iv) equilibrium air, (v) perfect gas. All the predictions are compared among themselves and also with flight measurement data. The nonequilibrium solutions for finite-catalytic wall conditions were obtained using the surface-catalysis relations given by Scott (Ref. 6).

The present numerical scheme was further extended to include the capability to treat the nonequilibrium wall- and shock-slip conditions. At high altitude, low Reynolds num-

ber flight, the Knudsen number is finite, and the continuum model of the gas breaks down in the Knudsen-layer where large gradients of properties exist. The nonequilibrium wall-slip relations derived by Hendricks (Ref. 14) are extended for the present coordinate system. The nonequilibrium shock-slip equations given by Davis (Ref. 3) are applied to the present numerical method.

In the present analysis, the computational results of the surface heating rate are compared with the STS-2 flight data, and the surface pressure results are compared with the flight data and also with the inviscid HALIS solution. The comparisons show good agreement. Variations of some shock-layer profiles along the body are presented for different catalytic wall conditions. In order to demonstrate the "three-dimensional effect" on the surface heating rate as well as the other surface-measurable quantities, the present SHTNEQ method has also been applied to the "equivalent axisymmetric body" of the space shuttle orbiter at high angle-of-attack. The equivalent axisymmetric body is obtained by taking the windward center-line on the shuttle surface and making a body of revolution around the wind axis passing the physical stagnation-point of the shuttle at high angle-of-attack. The resulting body has a similar shape to a sphere-cone of about 45-deg half-cone angle.

In the following chapters, analyses of theoretical development and numerical formulations are presented, and discussions of various computational results and comparisons are also presented. In the appendices, detailed governing equations and boundary conditions are given, and a description of the developed computer code (SHTNEQ) and a procedure for the generation of shock-shape input are also presented.

Chapter II

ANALYSIS

In this chapter a description of the theoretical background and development is given. For a general three-dimensional vehicle like the shuttle orbiter, an accurate geometry definition is a prerequisite for any analysis of the flowfield over the vehicle. Using the QUICK method developed by Vachris and Yaeger (Ref. 15), the geometry of the orbiter was represented by a series of analytical functions in a cylindrical coordinate system (z,r,ϕ). A moving map axis was necessary to define the center of the coordinate system as a function of z to ensure a unique value of r for a given angle ϕ around the body. The primary region of interest was the windward surface of the shuttle. Using QUICK, two versions of the space shuttle orbiter were obtained. The first conformed as close as possible to the actual vehicle (Fig. 1), with the exception that the canopy and tail-sections were removed. The second is a modified shuttle-like geometry which has the same lower surface and upper-symmetry plane profile (Fig. 2). For both geometries the wing was swept back to 55-deg from the design value of 45-deg to avoid an imbedded subsonic region at the wing-body juncture which cannot be handled by the inviscid methods

used here. For the modified geometry, however, the region between the strake and wing leading edge and the upper symmetry-plane, was filled in with elliptic curves. Nevertheless, the windward side geometry is a good representation of the space shuttle up to about ϕ = 80-deg. Because the region of interest was the windward surface only, the latter modified geometry has been used in this analysis. Large changes in transverse curvature are present at the wing leading-edge as seen in cross-sections of the modified shuttle-like geometry (Fig. 3). It must also be mentioned here that the location of the transverse curvature discontinuity moves from ϕ = 65-deg to about ϕ = 80-deg in the latter half of the vehicle.

For the present nonequilibrium 3-D viscous flow prediction, a shock shape is required as an input. The shock shape may be obtained from an inviscid solver, and the modified shuttle geometry is used in order to obtain an entire inviscid flowfield solution past the shuttle. At low angle-of-attack less than 25-deg, an inviscid time-dependent method called BLUNT (Ref. 16) developed by Moretti can be used to obtain a solution over the non-spherical nose and an initial data plane is obtained at a station (z/Rn = 3.), where the axial Mach number is entirely supersonic. Then an inviscid marching method STEIN developed by Marconi and Yaeger

(Ref. 17) can be used to solve the downstream inviscid flowfield over the entire shuttle-like geometry using the initial data plane from BLUNT. In the case of high angle-of-attack (larger than 25-deg), the inviscid HALIS method developed by Weilmuenster and Hamilton (Ref. 13) must be used to obtain necessary shock-shape data. The following sections describe the present coordinate system and the governing equations.

2.1 COORDINATE SYSTEM

The coordinate system used in the present analysis is depicted in Fig. 4. The ξ_1 coordinate starts from the body nose-tip and is directed along the body on the body surface. According to the definition of coordinate system, the values of ξ_2 and ξ_3 are constant along the ξ_1 coordinate line. As shown in Fig. 4, the present coordinate system is a typical surface-oriented nonorthogonal coordinate system. In this coordinate system, the coordinate metric tensor, g_{ij} is a measure of the length scale and the angle between the coordinate lines. The ξ_3 coordinate starts from the windward symmetry plane and is directed around the body. At the body surface the ξ_3 coordinate is chosen to coincide with the ϕ coordinate of the reference cylindrical coordinate system. The ξ_2 coordinate is a straight line which starts from the

body surface and ends at the shock surface. The ξ_2 coordinate lines are always normal to the local body surface. In the present analysis, the ξ_2 coordinate is normalized by the local shock stand-off distance. In this normalized coordinate system, all the ξ_2 coordinate lines have unit length in the shock layer. Therefore,

$$\xi_2 = 0 \quad \text{at body surface, and}$$
$$\xi_2 = 1 \quad \text{at shock surface,} \tag{1}$$

and further,

$$g_{22} = 1. \quad \text{everywhere.} \tag{2}$$

In addition, the ξ_2 coordinate is always orthogonal to both the ξ_1 and ξ_3 coordinates at every grid point, which gives

$$g_{12} = g_{23} = 0. \tag{3}$$

But, in general, g_{13} is non-zero which indicates that the ξ_1 coordinate is not orthogonal to the ξ_3 coordinate. The Christoffel symbol and the determinant of coordinate metric tensor, g, are important factors in the governing equations written in this coordinate system. A detailed description of the procedure for coordinate and grid generations for a similar coordinate system is given in Ref. 11.

2.2 GOVERNING EQUATIONS

The governing equations are derived from the steady Navier-Stokes equations for a reacting gas mixture as given by Bird, Stewart and Lightfoot (Ref. 18) or Williams (Ref. 19), and they are written in a surface-oriented general nonorthogonal coordinate system. The present analysis follows the formulations of two-dimensional reacting flow by Miner and Lewis (Ref. 1) and three-dimensional perfect gas flow by Szema and Lewis (Ref. 9). The continuity and momentum equations are not afected by multi-component chemical reactions of species. However, the energy and species conservation equations contain the chemical production and diffusion terms which will be discussed later.

In the governing equations written in a general coordinate system, the velocity components, u, v and w, are tensor quantities, and the corresponding physical components are obtained by multiplying the respective term by $\sqrt{g_{ii}}$. The metric terms g_{ij} are obtained numerically from the grid generation procedure. The governing equations are first nondimensionalized by variables of order one at the body surface (corresponding to high Reynolds number, boundary-layer flow). The equations are also normalized by variables of order one in the outer inviscid flow (corresponding the

shock region). In order to avoid dividing by near-zero shock-values, the normal and cross-flow velocities are not normalized. Also, temperature and species concentrations are not normalized. The normal velocity v and normal coordinate ξ_2 are assumed to be order of ε, and all terms which are of higher order than ε are neglected in the governing equations to obtain a single set of equations. Thus, the shock-layer equations are free from all the difficulties in the conventional two-layer (viscous boundary-layer and outer inviscid region) approaches, especially in low Reynolds number flows. The resulting set of shock-layer equations is uniformly second-order accurate in the inverse Reynolds number parameter, ε, from the body to the shock. The resulting equations are parabolic in both streamwise and transverse directions, and hence, the present numerical method uses the marching scheme in both directions. In the body-normal direction, the equations are elliptic and solved by an efficient implicit numerical scheme by Richtmyer (Ref. 20). Due to the parabolic character of the governing equations, a solution can not be obtained in flow-separated region in the axial- or cross-flow direction. Only laminar flow is considered in the present analysis. Detailed governing equations are presented in Appendix A.

2.3 BOUNDARY CONDITIONS

At high altitude (150 to 350 kft), low Reynolds number flight, the Knudsen number is finite, and the continuum model of the gas breaks down in the Knudsen layer where large gradients of the properties exist. At the body surface, the velocity-slip and temperature-jump boundary conditions can be used, if necessary, especially at high altitude, low density flight conditions. In the present analysis, the nonequilibrium wall-slip equations for a spherical geometry given by Hendricks (Ref. 14) have been rewritten for the present body-oriented general coordinate system and chemical model.

The calculated Reynolds number parameter ε was less than 0.108 for the present test cases which indicates that the slip effects on the heating rate and surface pressure will be small (see e.g. Ref. 2), but the slip effects on some shock-layer profiles are not negligible, and hence, are calculated over the nose region and presented. Wall temperature is an input which may be constant or a specified distribution. In the present calulations for the test cases, the wall temperature is specified by the STS-2 flight thermocouple data. The pressure at wall is obtained from the one-sided two-point differencing of the normal momentum equation.

In the present calculations, the wall species concentrations are dictated by non-catalytic, fully-catalytic, or finite-catalytic condition. For hypersonic nonequilibrium air flow, the surface heating rate is strongly affected by surface catalytic activity to the recombination of the dissociated oxygen and nitrogen atoms. Temperature-dependant energy-transfer catalytic recombination coefficients measured by Scott (Ref. 6) for nitrogen and oxygen recombination on the HRSI coating are used in the calculations for the finite-catalytic wall condition. At the low surface temperature of the shuttle, the equilibrium catalytic wall condition can be replaced by the fully catalytic wall condition. Detailed equations for the wall boundary conditions are given in Appendix B.

In the present method, shock shape information is necessary as an input which is used for the calculation of the shock-boundary condition. At low density flight conditions the bow shock may have a finite thickness. In that case, after-shock quantities must be obtained using modified shock-jump relations for reacting-gas flow as given by Davis (Ref. 3) and Cheng (Ref. 21). In the present analysis, the numerical iteration scheme of the three-dimensional shock-boundary conditions with slip for perfect gas by Murray and Lewis (Ref. 12) have been extended to include the finite-

rate chemistry and the nonorthogonal coordinate system. First, two-dimensional shock-normal coordinates are defined in the plane which contains both the freestream velocity vector and the vector which is normal to the local shock surface. Then, the freestream velocity vector is written in the shock-normal coordinates, and two-dimensional shock-crossing conditions are calculated in the shock-normal coordinates using an iteration scheme. The computed after-shock quantities are rotated into the directions of three-dimensional computational coordinates. The complete set of the conservation equations for the modified Rankine-Hugoniot shock-crossing conditions for reacting gas flow is given in Appendix B.

2.4 THERMODYNAMIC AND TRANSPORT PROPERTIES

The specific heat, C_p, and static enthalpy, h, are required for each of the species considered and for the gas mixture. Also required are the viscosity, μ, and the thermal conductivity, k. Since the multi-component ionizing air is considered to be a mixture of thermally perfect gases, the thermodynamic and transport properties for each species are calculated using the local temperature. The properties for the gas mixture are then determined in terms of the individual species properties. In this section all expres-

sions are presented in terms of dimensional quantities, and the superscript star will not be used to denote dimensional quantities. Since the present analysis follows the formulation of Miner and Lewis (Ref. 1), except the mixture viscosity and conductivity, more details beyond the descriptions given in this section can be found in Ref. 1.

The enthalpy and specific heat of each species are obtained from the thermodynamic data tabulated by Browne (Refs. 22-24). A second-order Lagrangian method is used to interpolate the values at a given temperature. For the mixture specific heat,

$$C_p = \Sigma \; C_i \; C_{pi} \tag{4}$$

The viscosity of the individual species is calculated from the curve-fit relation,

$$\mu_i = \exp(C_i) \; T_k \; (A_i \; \ln T_k + B_i) \quad ; \quad \text{gm/(cm-sec)} \tag{5}$$

where A_i, B_i and C_i are the curve-fit constants for species from Blottner (Ref. 25), and T_k is the local temperature in degrees-Kelvin. The unit of the species viscosity is converted to lbf-sec/ft^2.

The thermal conductivity of the individual species is calculated from the Eucken semi-empirical formula using the species viscosity and specific heat by the expression:

$$k_i = \frac{\mu_i R}{M_i}\left(\frac{C_{pi} M_i}{R} + \frac{5}{4}\right) \quad ; \quad \text{lbf/(sec-R)} \tag{6}$$

After the viscosity and thermal conductivity of the individual species are calculated, the viscosity and thermal conductivity of the gas mixture are calculated by the method suggested by Armaly and Sutton (Refs. 26,27). The mixture viscosity is obtained by

$$\mu = \sum_{i=1}^{NS} (X_i^2/H_{ii}) \tag{7}$$

where,

$$H_{ii} = X_i^2/\mu_i + \sum_{\substack{j=1 \\ j\neq i}}^{NS} \frac{2X_i X_j M_i M_j}{\mu_{ij}\,(M_i+M_j)^2}\,(5/3/A_{ij} + M_j/M_i) \tag{8}$$

$$\mu_{ij} = \frac{32\, M_i\, M_j/(M_i+M_j))^{1/2}}{((M_i^{1/4}/\mu_i^{1/2})\, F_{ij} + (M_j^{1/4}/\mu_j^{1/2})\, B_{ij})^2} \tag{9}$$

The mixture conductivity is given by

$$k = -4 \sum_{i=1}^{NS} (X_i^2/L_{ii}) \tag{10}$$

where,

$$L_{ii} = -4\, X_i^2/k_i - \sum_{\substack{j=1 \\ j\neq i}}^{NS} 2\, X_i X_j \frac{\frac{15}{2}M_i^2 + \frac{5}{2}M_j^2 + 4\, M_i M_j A_{ij}}{(M_i + M_j)^2\, A_{ij}\, k_{ij}} \tag{11}$$

$$k_{ij} = k_i \frac{\sqrt{8\,(M_i + M_j)/M_j}}{(F_{ij} + (k_i/k_j)^{1/2}(M_i/M_j)^{1/4} B_{ij})^2} \tag{12}$$

For both viscosity and conductivity,

X_i : mole fraction of the i-th component.

μ_i : viscosity of the pure i-th component.

k_i : conductivity of the pure i-th component.

M_i : molecular weight of i-th component.

$A_{ij} = 1.25$ for all reactions.

$F_{ij} = 1.0$ for all reactions.

$B_{ij} = 0.15$ for reactions between NO^+ and others.

$B_{ij} = 1.0$ for reaction between NO^+ and NO^+.

$B_{ij} = 0.78$ for all other reactions.

It is known that Armaly's method gives more accurate predictions than the well-known Wilke's semi-empirical relations, especially at high temperatures.

In the present work, the diffusion model is limited to binary diffusion with the binary diffusion coefficient specified by the Lewis number of 1.4.

2.5 CHEMICAL REACTION MODEL

It is assumed that the chemical reactions proceed at a finite rate, and the rate of production terms $\dot{w}_i$ of the individual species are included in the energy equation and the species continuity equations. The $\dot{w}_i$ terms are functions of

both the temperature and the species concentrations, and they must be rewritten so that the temperature or the species concentrations appear as one of the unknowns as given in Ref. 1.

For a multi-component gas with NS distinct chemical species and NR simultaneous chemical reactions, the chemical reaction equations are written in the general stoichiometric form:

$$\sum_{i=1}^{NJ} \alpha_{ri} X_i \underset{k_{br}}{\overset{k_{fr}}{\rightleftharpoons}} \sum_{i=1}^{NJ} \beta_{ri} X_i \qquad (13)$$

where $r = 1,2, \ldots$ NR and NJ is equal to the sum of the number of species and the number of catalytic third bodies. The symbols X_i represent the chemical species and the catalytic third bodies, and the α_{ri} and β_{ri} are the stoichiometric coefficients for reactants and products. The rates at which the forward and backward reactions occur are specified by the forward and backward rate constants which are given by the equations:

$$k_{fr} = T_k^{(C2_r)} \exp(C0_r - C1_r/T_k) \qquad (14)$$

and

$$k_{br} = T_k^{(D2_r)} \exp(D0_r - D1_r/T_k) \qquad (15)$$

where T_k is the temperature in degrees-Kelvin. The constants $C0_r$, $C1_r$, $C2_r$, $D0_r$, $D1_r$ and $D2_r$ depend in part on the spe-

cific reaction equations chosen. In the present calculations, the chemical reaction model and the reaction-rate constants are taken from Blottner (Ref. 10). The seven (7) reaction equations for seven (7) species (O, O_2, NO, N, NO^+, N_2, e^-) are given in Table 2, and the third-body catalytic efficiencies are also given. The reaction rate constants are given in Table 3.

The chemical production terms are calculated from the rate constants and species mass fractions, and detailed relations are given in Ref. 1. Since the rate of production terms are for nonequilibrium flows, the present method encounters difficulty in obtaining a converged solution whenever the flow conditions approach equilibrium. The difficulty is severe, particularly at the stagnation point.

2.6 NUMERICAL SOLUTION

Davis (Ref. 2) presented an implicit finite-difference method to solve the viscous shock-layer equations for axially symmetric flows, and Murray and Lewis (Ref. 12) further developed the scheme for three-dimensional flows. In the present work, the method is extended to the chemically reacting three-dimensional flowfield solution in a surface-oriented nonorthogonal coordinate system. Since the viscous

shock-layer equations are parabolic in both the streamwise and crossflow directions, the equations are solved by a highly efficient finite-difference scheme. The continuity and normal momentum equations are solved in a coupled form to promote convergence. The shock stand-off distance is evaluated by integrating the continuity equation.

The solution begins on the spherically blunted nose by obtaining an axisymmetric solution in the wind-fixed coordinate system. The axisymmetric solution is rotated into the body-fixed coordinates and is used as the initial profile for the three-dimensional solution. The three-dimensional solution begins in the windward plane and marches around the body obtaining a converged solution at each ξ_3-step. After completing a sweep at a ξ_1 marching station, the procedure then steps downstream in ξ_1 and begins the next ξ_3-sweep. At each point the equations are solved in the following order: (i) species continuity, (ii) w-momentum, (iii) energy, (iv) u-momentum, (v) integration of continuity for shock-layer thickness, and (vi) coupled continuity and normal momentum equations.

A solution may fail to converge when a geometry is complex and/or the angle-of-attack is high. In order to overcome the convergence problem, a more refined shock input may

be used. Applying a larger damping factor during a local iteration may also help the convergence. In the present analysis, the explicit pressure gradient model has been applied over the winged section of the shuttle to promote convergence.

Chapter III

RESULTS AND DISCUSSION

In order to predict the shuttle reentry flowfield, three test cases were chosen, and the viscous windward flowfield solutions were obtained using various chemical models. For the wide range of the shuttle reentry conditions (above 50 km altitude), the nonequilibrium effects can occur, and the nonequilibrium effects are largest near the nose of the body and around t = 450 sec on the trajectory (Ref. 8). The altitudes selected for the present calculations are 81, 70 and 60 km (t = 250, 460, 630 sec, respectively). Detailed freestream conditions for the three test cases are given in Table 1. A shuttle geometry close to the actual configuration is shown in Fig. 1, and the geometry modified for the inviscid solution is shown in Fig. 2. The cross-sections of the modified shuttle orbiter which have been used for the inviscid and the present viscous solutions are depicted in Fig. 3. Surface temperature data used in the present calculations are specified by the STS-2 flight thermocouple data, and are shown in Fig. 5.

The inviscid input shock shapes for the present calulations have been provided by the HALIS method for an angle-of-attack of 40-deg for both perfect gas and equilibrium

air, and the inviscid HALIS shock was available only up to z/L = 0.5. The viscous flowfield solutions for both perfect gas and equilibrium air have been obtained up to z/L = 0.5 in order to compare with the nonequilibrium solutions. The nonequilibrium solutions, however, were obtained for the entire windward surface up to the body end using an extrapolated shock. The shock extension was done using the STEIN (Ref. 17) solution of the shock shape for an angle-of-attack of 25-deg. The extrapolated shock was scaled and smoothed before being used as input data. In order to enhance the accuracy of the nonequilibrium viscous solution, a global iteration was performed using the viscous output shock as an input. Figures 6 and 7 show the three-dimensional shock stand-off distance and shock-slope distributions along the body for Case 1, which have been used as input data for the first global iteration (not zeroth iteration).

The nonequilibrium solutions have been obtained for noncatalytic, finite-catalytic and also fully-catalytic wall conditions for the purpose of comparison. Presented results include the surface heating rate, surface pressure, shock shapes, a few shock-layer profiles, and finally slip effects over the nose region. The orbiter Development Flight Instrumentation (DFI) includes thermocouples mounted within the thermal protection system (TPS) at many locations. The measured temperature-time histories are used in an inverse,

one-dimensional, transient heat-transfer analysis by Throckmorton (Ref. 28) to determine convective heating-rates to the surface. These flight heating-rate data are used for the comparison with the present computational results. The flight measurement data of wall pressure are used for comparison with the present surface-pressure predictions.

3.1 SURFACE HEATING RATE

The heating-rate predictions along the windward centerline are compared with each other in Fig. 8 for Case 1. The nonequilibrium solution with noncatalytic wall condition agrees well with the flight data for most of the region. The agreement is excellent considering the uncertainty of 10 % in the flight data (Ref. 8) and also the uncertainty of the gas-phase reaction rates. The nonequilibrium solution with fully catalytic wall condition shows quite close agreement with the equilibrium air solution. The heating-rate prediction from the perfect gas model is below the equilibrium air soluiton but well above the noncatalytic wall solution for the entire body. The reason for the local mismatch with flight data around $z/L = 0.2$ is not currently known. At $z/L = 0.4$, the perfect gas solution is 20 % lower than the equilibrium solution and 50 % higher than the noncatalytic wall solution. In fact, the surface finite cata-

lytic effect for Case 1 is negligible compared to that for Cases 2 and 3 due to the altitude dependence of the surface catalytic activity (low density effect, see Ref. 5). This effect will be clearly observed in the latter section for surface catalysis. The decrease of the heating after z/L = 0.8 is due to the slope change of the body surface.

For Cases 2 and 3, the general trends of the computed heating rates are similar to the result of Case 1, but the noncatalytic wall solution underpredicts the flight data, especially on the nose region as shown in Figs. 9 and 10. The result from finite-catalytic wall condition using Scott's relation agree well with the flight data for most of the region. However, the reason for the local mismatch around z/L = 0.2 for Case 2 is not clearly known. For Case 3, the finite-catalytic wall solution overpredicts the flight data by about 10 % on the forward half of the body, and agree well on the rear half of the body. The mismatch may be partially due to the uncertainty of the surface catalytic recombination rate data. In Ref. 6, Scott discussed the possibility of overprediction in the arc-jet catalysis measurements due to contamination of the jet-flow. The average uncertainty of his measurement of surface-catalysis was about 100 %, although there were many fluctuations in the uncertainties at each data point. In Fig. 11, the none-

quilibrium solution with noncatalytic wall condition along the body is shown for various ϕ-planes, together with the corresponding equilibrium air solution for Case 2. The equilibrium air solution is much higher than the noncatalytic wall solution for all the ϕ-planes. The sudden increase of the heating rate at ϕ = 80-deg and z/L = 0.5 is due to the spanwise slope change of the body surface along the body (see Fig. 3). At z/L = 0.6 and ϕ = 90-deg, the solution did not converge, due to the severe surface slope change of the wing tip section. The calculated spanwise heating rates for Case 2 at two axial stations (z/L = 0.2 and 0.44) are shown in Figs. 12 and 13. The comparisons among the various chemical models show similar trends and correlations for the spanwise heating rate distributions due to the flow expansion around the body. Figure 14 shows the altitude effect on the surface heating rate distribution around the body at z/L = 0.7.

3.2 SURFACE PRESSURE COMPARISON

In Figs. 15-18, the surface-pressure distributions over the entire shuttle windward surface are presented together with the available flight data for comparison. The ϕ-planes from 10-deg to 40-deg were omitted on the plots because the results for those planes were almost identical with the re-

sult for the windward centerline. The agreement with flight data is good especially on the windward centerline for Cases 2 and 3. The inviscid HALIS (Ref. 13) pressure is also compared to the present nonequilibrium SHTNEQ solution for Case 2 in Fig. 17. The inviscid data were available only up to $z/L = 0.46$ due to the very high angle-of-attack involved and the expanding wing. The agreement is good for most of the region. For $\phi > 70$ deg, agreement is not so good, and for this region the inviscid result may be more accurate, because the inviscid solution used more planes around the body considering the existence of the wing. The present SHTNEQ solution used 19 planes while the inviscid HALIS solution used 30 planes around the half-body (from 0 to 180 deg). In Figs. 19-21, the spanwise surface pressure distributions are shown at three axial stations ($z/L = 0.1$, 0.2 and 0.7). The present calculation tends to underpredict over the flow expansion region (off the centerline) compared to the flight data (e.g. about 20 % underprediction at $\phi = 67$-deg, $z/L = 0.1$). This disagreement may be partly due to the uncertainty of the flight data, or a calculation using a smaller ϕ-stepsize may reduce the discrepancy. The present solution by the SHTNEQ method used ϕ-stepsize of 10-deg around the body, and this stepsize may not be small enough for the noncircular cross-sections of the shuttle geometry (see Fig.

3). By including more ϕ-planes, however, the current relatively large storage requirement and computing time must be increased accordingly.

3.3 SHOCK-LAYER THICKNESS

A comparison is shown in Fig. 22 of the shock-layer thickness distribution along the body at the ϕ = 0 plane which has been obtained from various chemical models. All the viscous shock shape results except the inviscid shock are from the once globally iterated results. When an inviscid input shock is not a good prediction, the output shock shape is, in general, different from the input shock. In such a case, a global iteration is necessary in order to refine the entire flowfield solution. Thus, for the present three test cases, all the viscous flowfield solutions presented are from the first global iteration. The inviscid shock is from the HALIS code and was available only up to z/L = 0.5 as mentioned earlier. The inviscid HALIS shock for α = 40-deg has been extended by the inviscid shock of α = 25-deg from the STEIN method. The extended shock was scaled and smoothed and then used as the input shock data for the initial calculation (zeroth iteration). When the various viscous shock-layer thicknesses are compared to the inviscid perfect gas shock at z/L = 0.4, the viscous perfect

gas shock is 86.7 %, the nonequilibrium shock is 52.8 % and the equilibrium shock is 36.1 %. The shock from the fully catalytic wall condition is almost identical to the noncatalytic wall solution. The effect of global iteration on the shock-layer thickness distribution along the windward symmetry-plane is shown in Fig. 23 for Case 1. The 0th (zeroth) global iteration indicates the present SHTNEQ solution using the inviscid input shock. The 1st (first) global iteration indicates the SHTNEQ solution using the 0th iteration output shock. As shown in the figure, the 0th iteration output shock is quite different from the inviscid input shock. In such a case, a global iteration is necessary in order to refine the entire flowfield solution. Thus, for the present three test cases, all the presented results are from the first global iteration.

3.4 COMPARISON OF SHOCK-LAYER PROFILES

The nonequilibrium flowfield structure of the viscous shock-layer at a few selected axial stations on the windward centerline is depicted for both the noncatalytic and fully catalytic wall conditions in Figs. 24-27. The profiles include temperature, tangential velocity and mass fractions of oxygen and nitrogen atoms for Case 2 (t = 460 sec). The temperature and velocity profiles in Figs. 24 and 25 show

that the viscous effects are dominant across the entire shock-layer, especially on the forward part of the body. At the axial station of z/L = 0.046 in the plot of temperature profile, the wall temperature gradient of the fully catalytic wall solution is larger than that of the noncatalytic wall solution, which produced a 34 % larger conduction heating rate. At the same station the heating rate due to mass diffusion was 93 % of the conduction heating rate in the fully catalytic wall solution. The diffusive heating in the noncatalytic wall case was, of course, zero. The surface chemical catalycity has negligible effect on the velocity profile as shown in Fig. 25. The mass-fraction profiles of oxygen and nitrogen clearly show the effects of the noncatalytic and fully catalytic wall conditions. In the noncatalytic wall case, the oxygen atom concentration at the wall remains almost constant along the body, while the nitrogen atom concentration is reduced downstream due to more rapid recombination.

3.5 SLIP EFFECTS

The SHTNEQ method has been further extended to include the shock- and wall-slip conditions. In high altitude free-stream conditions, the conventional frozen shock crossing of Rankine-Hugoniot relations for nonequilibrium flows gives a

poor prediction of the after-shock quantities. It is known that the slip effects on surface-measurable quantities like heating rate and pressure are siginificant, especially for reentry bodies with a small nose radius at high altitude (150 to 350 kft). For the space shuttle at the test case freestream conditions, however, the calculated Reynolds number parameter ε was less than 0.108 which indicates that the slip effects on the surface-measurable quantities will not be significant (Ref. 2). But, the slip effects on some shock-layer profiles and skin friction are not negligible, and hence, are calculated over the nose region and presented.

In Fig. 28, the shock-slip effects on the temperature profile and mass fraction of oxygen and nitrogen atoms are shown at the stagnation point. The slip temperature at the shock is less than the no-slip temperature by 1500 deg-K. The shock-slip effect on the oxygen mass-fraction distribution across the shock-layer is limited to the region near the bow shock, but for nitrogen the shock-slip effect is propagated all throughout the shock-layer. Figure 29 shows the wall-slip effects on the surface temperature and axial flow velocity jumps over the nose region for Case 2. The amount of the temperature jump is about 200 deg-K at the stagnation point, and the slip velocity is 0.0056 times the

freestream velocity at s/Rn = 0.8. The wall-slip effect on the skin-friction coefficient on the nose region is also presented in Fig. 30 for Cases 1 and 2, and the effect is negligible for the present test cases.

3.6 EFFECT OF SURFACE FINITE-CATALYSIS

For hypersonic nonequilibrium flow, the surface heating-rate is strongly affected by surface catalytic activity to the recombination of the dissociated oxygen and nitrogen atoms. Previously, most investigators tended to assume fully catalytic or equilibrium catalytic walls in order to obtain a more conservative solution of the heating rate. Recently, however, Rakich (Ref. 8) determined that the shuttle RCG coating is almost noncatalytic through his analysis of flight experiment data. But, depending on altitude condition, the present computational analysis shows that the catalysis effect on the heating rate is not negligible especially on the nose-region, as already shown in a previous section. In this section, more detailed discussions focused on the surface-catalysis are presented.

Figure 31 shows a comparison of surface catalytic recombination-rates between the relation from Scott (Ref. 6) and the one from Rakich (Ref. 8). The catalycity for nitrogen

based on meaningful experiment data was available only from Scott. The recombination rates for oxygen agree well between the two curve-fit relations in the temperature region from 1000 deg-K to 1500 deg-K, but do not agree well at high and low temperatures. In Fig. 32, the recombination rate distributions along the body for Cases 1 and 3 are shown for both nitrogen and oxygen. It is noted that the nitrogen recombination rate is much higher than the oxygen rate for most of the region, although the recombination-rate data have relatively large uncertainty of about 100% (Ref. 6). Scott's curve for oxygen at low temperatures is an extrapolated one, so the curve from Rakich may be more accurate at the low temperatures. The effect on the heating-rate, however, should be negligible at these low recombination rates (k_w < 10 cm/sec).

In Figs. 33 and 34, the heating rates over the nose for various surface catalysis are presented for Cases 1 and 2, respectively. For Case 1, Scott's surface catalytic recombination rates were about 100 cm/sec for oxygen and about 400 cm/sec for nitrogen. For Caes 2, the rates were about 500 cm/sec for oxygen and about 600 cm/sec for nitrogen. The highest heating rate is obtained from the assumption of equilibrium air and the result for a fully-catalytic wall is quite close to the equilibrium air solution. For Case 1 (Fig. 33), the finite-catalytic wall solution is quite close

to the noncatalytic wall solution, which indicates that at the high altitude condition of Case 1 the catalytic recombination activity is small due to the very low density. In Fig. 34 the heating rate for a recombination rate of 200 cm/sec (for both oxygen and nitrogen) is also presented for comparison. At the stagnation point of Case 2, the heating rate from Scott's recombination rate is 1.8 times the noncatalytic wall solution, and the equilibrium air solution is 3.0 times the noncatalytic wall solution. Surface heating rate has also been computed using the Rakich's catalysis data, and the result obtained was 5 % higher than the result from Scott's data.

3.7 EQUIVALENT AXISYMMETRIC BODY CONCEPT

In order to demonstrate the "three-dimensional effect", the present method was also applied to the equivalent axisymmetric body, and the results are compared to the solution for the actual shuttle geometry. The equivalent axisymmetric body is obtained by taking the windward center-line on the shuttle surface and making a body of revolution around the wind axis passing the physical stagnation-point of the shuttle at high angle-of-attack. The resulting body has a similar shape to a sphere-cone of about 45-deg half-cone angle. Shinn et al. (Ref. 5) replaced the actual shuttle

windward center-line with an equivalent hyperboloid in order to apply the two-dimensional reacting viscous shock-layer method.

In the present analysis, the equivalent axisymmetric body is made using the actual shuttle windward center-line defined by QUICK geometry package, since the present SHTNEQ method can treat non-analytic geometries. At high angle-of-attack (about 40-deg in the test cases), the equivalent axisymmetric body has a very large cross-sectional diameter, especially in the after-body region, which may produce a solution different from the accurate three-dimensional solution for the original shuttle geometry.

The present method was applied to both the actual shuttle geometry and the equivalent axisymmetric body, and the results are compared with each other. Figure 35 shows the comparison of the surface heating rates. The result from two-dimensional viscous shock-layer by Shinn et al. (Ref. 5) is also included for comparison. Both solutions from the axisymmetric body concept underpredict by about 30 % compared to the present 3-D shuttle solution. Therefore, the equivalent axisymmetric body should not be used to simulate the actual three-dimensional shuttle geometry at high angle-of-attack. The result from the second global iteration is

also presented for the forward part of the axisymmetric body, which indicates that the result from the first global iteration is already well converged solution. In Fig. 36 the solutions for the skin-friction coefficient are also presented, and there is about 50 % difference between the two solutions. Surface-pressure distributions along the body are compared in Fig. 37, and the axisymmetric body solution overpredict about 5 to 10 % compared to the 3-D shuttle geometry solution. Figure 38 presents the comparison for the shock-layer thickness distributions along the body. The shock-layer thickness from the axisymmetric body concept is much thicker than the one from the 3-D shuttle geometry (about 1.5 times at the body-end), as can be expected. Thus, the present analysis shows that the actual shuttle geometry must be used in the three-dimenisonal numerical simulation in order to obtain an accurate prediction of the shuttle nonequilibrium flowfield, especially in the case of high angle-of-attack.

3.8 COMPUTING TIMES

The computing times required for the flowfield computations of all the test cases are listed in Table 4. The computing times are based on an IBM 370/3081 general purpose computer. The nonequilibrium computations took about one

and half hour CPU times for solving the entire shuttle windward surface. When an input shock data is not accurate, generally a global iteration is required, thus consuming more computing time than the tabulated one. The computing times for the perfect gas and equilibrium air are for the solution of the first half of the body (up to z/L = 0.5). The solution of the perfect gas or equilibrium air flows took relatively small computing times (less than 20 % of non-equilibrium case).

The axial marching step-sizes are controlled internally in the code considering the number of local iterations taken. A fixed input of 51 or 101 grid points were used in the surface-normal direction and 10 planes were used around the body for the windward surface (10 deg step-size). The leeward surface of the space shuttle was not considered, because a solution can not be obtained by the present method due to strong crossflow separation. The storage requirement of the present SHTNEQ code is 852 kilo-bites in IBM 370/3081 computer.

Chapter IV

CONCLUSIONS

In general, the computional results of surface heating rate for the three-dimensional nonequilibrium flowfield over the space shuttle compare well with the available flight data. The flight heating rate data agree well with the noncatalytic wall solution for Case 1 and are lower than or agree well with the finite-catalytic wall solution for Cases 2 and 3. The nonequilibrium solution with fully catalytic wall gives quite close agreement with the chemical equilibrium heating rate prediction. The perfect gas solution of surface heating rate is less than the equilibrium solution but higher than the flight data for the entire region.

The calculated pressure distribution also shows good agreement with the flight data. The calculated nonequilibrium shock- and wall-slip effects on the heating rate and surface pressure were negligible for the present test cases. The present parametric study on the surface catalysis effect shows that proper chemical model and accurate catalytic recombination rate data are very important for an accurate prediction of the shuttle surface heat-transfer.

From the numerical analysis using the equivalent axisymmetric qeometry, it is demonstrated that the three-dimensional effect on the surface-measurable quantities is not negligible in the case of high angle-of-attack, and hence, a three-dimensional solver like SHTNEQ should be used for an accurate nonequilibrium flow prediction. The computing times taken for the nonequilibrium calculation are reasonable considering the large size of computational grid due to the complex shuttle geometry and the chemical reactions of seven species.

REFERENCES

1. Miner, E. W. and Lewis, C. H., "Hypersonic Ionizing Air Viscous Shock-Layer Flows over Nonanalytic Blunt Bodies," NASA CR-2550, May 1975.
2. Davis, R. T., "Numerical Solution of the Hypersonic Viscous Shock-Layer Equations," AIAA Journal, May 1970, pp. 843-851.
3. Davis, R. T., "Hypersonic Flow of a Chemically Reacting Binary Mixture Past a Blunt Body," AIAA Paper No. 70-805, July 1970.
4. Moss, J. N., "Solutions for Reacting and Nonreacting Viscous Shock-Layers with Multicomponent Diffusion and Mass Injection," PhD Dissertation, Virginia Polytechnic Institute and State University, Blacksburg, Virginia, October 1971.
5. Shinn, J. L., Moss, J. N., and Simmonds, A. L., "Viscous Shock-Layer Heating Analysis for the Shuttle Windward Plane with Surface Finite Catalytic Recombination Rates," AIAA Paper No. 82-0842, June 1982.
6. Scott, C. D. and Derry, S. M., "Catalytic Recombination and The Space Shuttle Heating," AIAA Paper No. 82-0841, June 1982.
7. Rakich, J. V. and Lanfranco, M. J., "Numerical Computation of Space Shuttle Laminar Heating and Surface

Streamlines," Journal of Spacecraft and Rocket, Vol. 14, No. 5, pp. 265-272, May 1977.

8. Rakich, J. V., Stewart, D. A., and Lanfranco, M. J., "Results of a Flight Experiment on the Catalytic Efficiency of the Space Shuttle Heat Shield," AIAA Paper No. 82-0944, June 1982.
9. Szema, K. Y. and Lewis, C. H., "Three-Dimensional Viscous Shock-Layer Flows Over Lifting Bodies at High Angles of Attack," AIAA Paper No. 81-1146, June 1981.
10. Blottner, F. G., Johnson, M., and Ellis, M., "Chemically Reacting Viscous Flow Program for Multi-Component Gas Mixtures," Sandia Laboratories Report SC-RR-70-754, Dec. 1971.
11. Helliwell, W. S., Dickinson, R. P., and Lubard, S. C., "Viscous Flow over Arbitrary Geometries at High Angle of Attack," AIAA Paper No. 80-0064, Jan. 1980.
12. Murray, A. L. and Lewis, C. H., "Hypersonic Three-Dimensional Viscous Shock-Layer Flow over Blunt Bodies," AIAA Journal, Vol. 16, No. 12, pp. 1279-1286, December 1978.
13. Weilmuenster, K. James and Hamilton, H. Harris, II, "A Method for Computation of Inviscid Three-Dimensional Flow Over Blunt Bodies Having Large Embedded Subsonic Regions," AIAA Paper No. 81-1203, June 1981.
14. Hendricks, W. L., "Slip Conditions with Wall Catalysis

and Radiation for Multicomponent Nonequilibrium Gas Flow," NASA TM X-64942, June 1974.

15. Vachris, A. F. and Yaeger, L. S., "QUICK-GEOMETRY: A Rapid Response Method for Mathematically Modeling Configuration Geometry," NASA SP-390, 1975, pp.49-73.
16. Moretti, G. and Bleich, G., "Three-Dimensional Flow Around Blunt Bodies," AIAA Journal, Vol. 5, 1967.
17. Marconi, F. and Yaeger, L., "Development of a Computer Code for Calculating the Steady Super/Hypersonic Inviscid Flow Around Real Configurations," NASA CR-2675, April 1976.
18. Bird, R. B., Stewart, W. E., and Lightfoot, E. N., "Transport Phenomena," John Wiley and Sons, Inc., 1960.
19. Williams, F., "Combustion Theory," Addison Wesley Book Co., Inc., 1965.
20. Richtmyer, R. D., "Difference Methods for Initial-Value Problems," Interscience Publishers, Inc., New York, 1957.
21. Cheng, H. K., "The Blunt-Body Problem in Hypersonic Flow at Low Reynolds Number," IAS Paper No. 63-92, Jan. 1963, also Cornell Aeronautical Laboratory Report No. AF-1285-A-10, June 1963.
22. Browne, W. G., "Thermodynamic Properties of Some Atoms and Atomic Ions," MSD Engineering Physics TM2, General Electric Co., Philadelphia, Pa., 1962.
23. Browne, W. G., "Thermodynamic Properties of Some Diatomic

and Linear Polyatomic Molecules," MSD Engineering Physics TM3, General Electric Co., Philadelphia, Pa., 1962.

24. Browne, W. G., "Thermodynamic Properties of Some Diatoms and Diatomic Ions at High Temperature," MSD Advanced Aerospace Physics TM8, General Electric Co., Philadelphia, Pa., May 1962.

25. Blottner, F. G., "Non-equilibrium Laminar Boundary-Layer Flow of Ionized Air," General Electric Report R64SD56, November 1964.

26. Armaly, B. F. and Sutton, K., "Viscosity of Multicomponent Partially Ionized Gas Mixtures Associated with Jovian Entry," Aerothermodynamics and Planetary Entry, Progress in Astronautics and Aeronautics, Vol. 77, edited by A. L. Crosbie, AIAA, New York, 1981, pp. 335-350.

27. Armaly, B. F. and Sutton, K., "Thermal Conductivity of Partially Ionized Gas Mixtures," Thermophysics of Atmospheric Entry, Progress in Astronautics and Aeronautics, Vol. 82, edited by Thomas E. Horton, AIAA, New York, 1982, pp. 53-67.

28. Throckmorton, D. A., "Benchmark Aerodynamic Heat Transfer Data from the First Flight of the Space Shuttle Orbiter," AIAA Paper No. 82-0003, Jan. 1982.

29. Swaminathan, S., Kim, M. D., and Lewis, C. H., "Nonequilibrium Viscous Shock-Layer Flows over Blunt Sphere-Cones at Angle-of-Attack," AIAA Paper No. 82-0825, June 1982.

Appendix A

DERIVATION OF GOVERNING EQUATIONS

The governing equations for three-dimensional shock-layer flows of reacting multicomponent gases are derived from the steady Navier-Stokes equations and chemical conservation equations, and they are written in a nonorthogonal curvilinear coordinate system. The shock-layer equations are nondimensionalized using freestream or reference quantities as follows:

$$u^* = u\,U_\infty \qquad v^* = v\,U_\infty$$

$$w^* = w\,U_\infty \qquad T^* = T\,T_{ref} = T\,U_\infty^2/C_{p\infty}$$

$$p^* = p\,\rho_\infty\,U_\infty^2 \qquad \rho^* = \rho\,\rho_\infty$$

$$C_p^* = C_p\,C_{p\infty} \qquad \mu^* = \mu\,\mu_{ref} = \mu\,\mu^*(T_{ref})$$

$$h^* = h\,U_\infty^2 \qquad k^* = k\,k_{ref} = k\,\mu_{ref}\,C_{p\infty}$$

$$\dot{w}_i^* = \dot{w}_i\,\rho_\infty\,U_\infty/R_n \qquad \xi_1^* = \xi_1\,R_n$$

$$\xi_2^* = \xi_2\,R_n \qquad \xi_3^* = \xi_3\,R_n \tag{A1}$$

The nondimensional parameters which appear in the shock-layer equations are given by the following relations:

$$Pr = C_p^*\,\mu^*\,/\,k^* \tag{A2}$$

$$\varepsilon^2 = \mu_{ref}/(\rho_\infty\,U_\infty\,R_n) \tag{A3}$$

$$Le_i = \rho^*\,C_p^*\,D_i^*\,/\,k^* \tag{A4}$$

The normal velocity v and normal coordinate ξ_2 are assumed to be order of ε, and all terms which are of higher order than ε are neglected in the governing equations. The nondimensionalized governing equations written in general body-oriented tensor form are given as follows:

Mass-averaged velocity vector

$$\underline{V} = u\underline{g}_1 + v\underline{g}_2 + w\underline{g}_3 \tag{A5}$$

Continuity equation

$$\frac{\partial}{\partial \xi_1}(\rho u g^{1/2}) + \frac{\partial}{\partial \xi_2}(\rho v g^{1/2}) + \frac{\partial}{\partial \xi_3}(\rho w g^{1/2}) = 0 \tag{A6}$$

u-momentum

$$\rho u \frac{\partial u}{\partial \xi_1} + \rho v \frac{\partial u}{\partial \xi_2} + \rho w \frac{\partial u}{\partial \xi_3} + \rho u^2 \left\{ {1 \atop 1\ 1} \right\} + 2\rho uv \left\{ {1 \atop 1\ 2} \right\}$$

$$+ 2\rho uw \left\{ {1 \atop 1\ 3} \right\} + \rho v^2 \left\{ {1 \atop 2\ 2} \right\} + 2\rho vw \left\{ {1 \atop 2\ 3} \right\} + \rho w^2 \left\{ {1 \atop 3\ 3} \right\}$$

$$+ \frac{g_{22}}{g}\left(g_{33} \frac{\partial p}{\partial \xi_1} - g_{13} \frac{\partial p}{\partial \xi_3} \right) = \frac{\varepsilon^2}{g_{22}}\left(\frac{\partial \mu}{\partial \xi_2} \frac{\partial u}{\partial \xi_2} + \mu \frac{\partial^2 u}{\partial \xi_2^2} \right) \tag{A7}$$

v-momentum

$$\rho u \frac{\partial v}{\partial \xi_1} + \rho v \frac{\partial v}{\partial \xi_2} + \rho w \frac{\partial v}{\partial \xi_3} + \rho u^2 \left\{ {2 \atop 1\ 1} \right\} + 2\rho uv \left\{ {2 \atop 1\ 2} \right\}$$

$$+ 2\rho uw \left\{ {2 \atop 1\ 3} \right\} + \rho v^2 \left\{ {2 \atop 2\ 2} \right\} + 2\rho vw \left\{ {2 \atop 2\ 3} \right\} + \rho w^2 \left\{ {2 \atop 3\ 3} \right\}$$

$$+ \frac{1}{g_{22}} \frac{\partial p}{\partial \xi_2} = 0 \tag{A8}$$

w-momentum

$$\rho u \frac{\partial w}{\partial \xi_1} + \rho v \frac{\partial w}{\partial \xi_2} + \rho w \frac{\partial w}{\partial \xi_3} + \rho u^2 \left\{ {3 \atop 1\,1} \right\} + 2\rho uv \left\{ {3 \atop 1\,2} \right\}$$

$$+ 2\rho uw \left\{ {3 \atop 1\,3} \right\} + \rho v^2 \left\{ {3 \atop 2\,2} \right\} + 2\rho vw \left\{ {3 \atop 2\,3} \right\} + \rho w^2 \left\{ {3 \atop 3\,3} \right\}$$

$$+ \frac{g_{22}}{g} \left(g_{11} \frac{\partial p}{\partial \xi_3} - g_{13} \frac{\partial p}{\partial \xi_1} \right) = \frac{\varepsilon^2}{g_{22}} \left(\frac{\partial \mu}{\partial \xi_2} \frac{\partial w}{\partial \xi_2} + \mu \frac{\partial^2 w}{\partial \xi_2^2} \right) \quad \text{(A9)}$$

Energy equation

$$\rho u C_p \frac{\partial T}{\partial \xi_1} + \rho v C_p \frac{\partial T}{\partial \xi_2} + \rho w C_p \frac{\partial T}{\partial \xi_3} - \left(u \frac{\partial p}{\partial \xi_1} + v \frac{\partial p}{\partial \xi_2} + w \frac{\partial p}{\partial \xi_3} \right)$$

$$= \frac{\varepsilon^2}{g_{22}} \frac{\partial}{\partial \xi_2} \left(k \frac{\partial T}{\partial \xi_2} \right) + \varepsilon^2 \mu \left\{ \frac{g_{11}}{g_{22}} \left(\frac{\partial u}{\partial \xi} \right)^2 + 2 \frac{g_{13}}{g_{22}} \frac{\partial u}{\partial \xi_2} \frac{\partial w}{\partial \xi_2} + \frac{g_{33}}{g_{22}} \left(\frac{\partial w}{\partial \xi_2} \right)^2 \right\}$$

$$+ \varepsilon^2 \left(\sum_{i=1}^{NS} C_{pi} \frac{\mu Le}{Pr} \frac{\partial Ci}{\partial \xi_2} \right) \frac{\partial T}{\partial \xi_2} - \sum_{i=1}^{NS} h_i \dot{w}_i \quad \text{(A10)}$$

Species continuity

$$\rho u \frac{\partial Ci}{\partial \xi_1} + \rho v \frac{\partial Ci}{\partial \xi_2} + \rho w \frac{\partial Ci}{\partial \xi_3} = \frac{\varepsilon^2}{g_{22}} \frac{\partial}{\partial \xi_2} \left(\frac{\mu Le}{Pr} \frac{\partial Ci}{\partial \xi_2} \right) + \dot{w}_i \quad \text{(A11)}$$

Equation of state

$$p = \frac{\rho RT}{\overline{M} C_{p\infty}} \quad \text{(A12)}$$

The species mass-fractions are given by

$$C_i = \rho_i / \rho \quad \text{(A13)}$$

The frozen specific-heat of the mixture is given by

$$C_p = \sum C_i C_{pi} \tag{A14}$$

The mixture molecular weight is given by

$$\bar{M} = 1 / \sum (C_i/M_i) \tag{A15}$$

The Christoffel symbols in the momentum equations can be expanded by the definition:

$$\left\{ \begin{matrix} i \\ j\ k \end{matrix} \right\} = \frac{1}{2} \sum_m g^{im} \left\{ \frac{\partial g_{mk}}{\partial \xi_j} + \frac{\partial g_{mj}}{\partial \xi_k} - \frac{\partial g_{jk}}{\partial \xi_m} \right\} \tag{A16}$$

Considering that $g_{12} = g_{21} = g_{23} = g_{32} = 0$ in the present coordinate system, the momentum equations become:

u-momentum

$$\rho u \frac{\partial u}{\partial \xi_1} + \rho v \frac{\partial u}{\partial \xi_2} + \rho w \frac{\partial u}{\partial \xi_3} + \frac{\rho u^2}{2}\left(g^{11}\frac{\partial g_{11}}{\partial \xi_1} + 2g^{13}\frac{\partial g_{13}}{\partial \xi_1} - g^{13}\frac{\partial g_{11}}{\partial \xi_3}\right)$$
$$+ \rho uv\left(g^{11}\frac{\partial g_{11}}{\partial \xi_2} + g^{13}\frac{\partial g_{31}}{\partial \xi_2}\right) + \rho uw\left(g^{13}\frac{\partial g_{33}}{\partial \xi_1} + g^{11}\frac{\partial g_{11}}{\partial \xi_3}\right)$$
$$+ \frac{\rho v^2}{2}\left(-g^{11}\frac{\partial g_{22}}{\partial \xi_1} - g^{13}\frac{\partial g_{22}}{\partial \xi_3}\right) + \rho vw\left(g^{11}\frac{\partial g_{13}}{\partial \xi_2} + g^{13}\frac{\partial g_{33}}{\partial \xi_2}\right)$$
$$+ \frac{\rho w^2}{2}\left(2g^{11}\frac{\partial g_{13}}{\partial \xi_3} + g^{13}\frac{\partial g_{33}}{\partial \xi_3} - g^{11}\frac{\partial g_{33}}{\partial \xi_1}\right) + \frac{g_{22}}{g}\left(g_{33}\frac{\partial p}{\partial \xi_1} - g_{13}\frac{\partial p}{\partial \xi_3}\right)$$
$$= \frac{\epsilon^2}{g_{22}}\left(\frac{\partial \mu}{\partial \xi_2}\frac{\partial u}{\partial \xi_2} + \mu\frac{\partial^2 u}{\partial \xi_2^2}\right) \tag{A17}$$

v-momentum

$$\rho u \frac{\partial v}{\partial \xi_1} + \rho v \frac{\partial v}{\partial \xi_2} + \rho w \frac{\partial v}{\partial \xi_3} + \frac{\rho u^2}{2}\left(-g^{22}\frac{\partial g_{11}}{\partial \xi_2}\right) + \rho uv\left(g^{22}\frac{\partial g_{22}}{\partial \xi_1}\right)$$
$$- \rho uw\left(g^{22}\frac{\partial g_{13}}{\partial \xi_2}\right) + \frac{\rho v^2}{2}\left(g^{22}\frac{\partial g_{22}}{\partial \xi_2}\right) + \rho vw\left(g^{22}\frac{\partial g_{22}}{\partial \xi_3}\right)$$
$$+ \frac{\rho w^2}{2}\left(-g^{22}\frac{\partial g_{33}}{\partial \xi_2}\right) + \frac{1}{g_{22}}\frac{\partial p}{\partial \xi_2} = 0 \tag{A18}$$

w-momentum

$$\rho u\frac{\partial w}{\partial \xi_1} + \rho v\frac{\partial w}{\partial \xi_2} + \rho w\frac{\partial w}{\partial \xi_3} + \frac{\rho u^2}{2}\left(g^{31}\frac{\partial g_{11}}{\partial \xi_1} + 2g^{33}\frac{\partial g_{13}}{\partial \xi_1} - g^{33}\frac{\partial g_{11}}{\partial \xi_3}\right)$$

$$+ \rho uv\left(g^{31}\frac{\partial g_{11}}{\partial \xi_2} + g^{33}\frac{\partial g_{33}}{\partial \xi_2}\right) + \rho uw\left(g^{33}\frac{\partial g_{33}}{\partial \xi_1} + g^{31}\frac{\partial g_{11}}{\partial \xi_3}\right)$$

$$+ \frac{\rho v^2}{2}\left(-g^{31}\frac{\partial g_{22}}{\partial \xi_1} - g^{33}\frac{\partial g_{22}}{\partial \xi_3}\right) + \rho vw\left(g^{31}\frac{\partial g_{13}}{\partial \xi_2} + g^{33}\frac{\partial g_{33}}{\partial \xi_2}\right)$$

$$+ \frac{\rho w^2}{2}\left(2g^{13}\frac{\partial g_{13}}{\partial \xi_3} + g^{33}\frac{\partial g_{33}}{\partial \xi_3} - g^{31}\frac{\partial g_{33}}{\partial \xi_1}\right) + \frac{g_{22}}{g}\left(g^{11}\frac{\partial p}{\partial \xi_3} - g^{13}\frac{\partial p}{\partial \xi_1}\right)$$

$$= \frac{\epsilon^2}{g_{22}}\left(\frac{\partial \mu}{\partial \xi_2}\frac{\partial w}{\partial \xi_2} + \mu\frac{\partial w}{\partial \xi_2^2}\right) \qquad \text{(A19)}$$

The variables in the above governing equations, except v, w, T and C_i, are normalized by the local after-shock quantities as listed below.

$$\bar{u} = u/u_{sh} \qquad \bar{p} = p/p_{sh} \qquad \bar{\rho} = \rho/\rho_{sh}$$

$$\bar{\mu} = \mu/\mu_{sh} \qquad \bar{k} = k/k_{sh} \qquad \bar{C}_p = C_p/C_{p,sh}$$

$$\xi = \xi_1 \qquad \eta = \xi_2/n_{sh} \qquad \zeta = \xi_3 \qquad \text{(A20)}$$

Due to the normalization of the body-normal coordinate, the metric g_{22} becomes constant ($g_{22} = 1.$) and some derivatives can be rewritten as

$$\frac{\partial}{\partial \xi_1} = \frac{\partial}{\partial \xi} - \frac{\eta}{n_{sh}}\frac{\partial n_{sh}}{\partial \xi}\frac{\partial}{\partial \eta} \qquad \text{(A21)}$$

$$\frac{\partial}{\partial \xi_2} = \frac{1}{n_{sh}}\frac{\partial}{\partial \eta} \qquad \text{(A22)}$$

$$\frac{\partial^2}{\partial \xi_2^2} = \frac{1}{n_{sh}^2}\frac{\partial^2}{\partial \eta^2} \qquad \text{(A23)}$$

$$\frac{\partial}{\partial \xi_3} = \frac{\partial}{\partial \zeta} - \frac{\eta}{n_{sh}} \frac{\partial n_{sh}}{\partial \zeta} \frac{\partial}{\partial \eta} \tag{A24}$$

The u-momentum, w-momentum, species continuity, and energy equations can be rewritten in the following standard parabolic form which can be solved by the efficient numerical scheme from Richtmyer (Ref. 20).

$$A0\frac{\partial^2 W}{\partial \xi_2^2} + A1\frac{\partial W}{\partial \xi_2} + A2\ W + A3 + A4\frac{\partial W}{\partial \xi_1} + A5\frac{\partial W}{\partial \xi_3} = 0 \tag{A25}$$

where, W denotes the dependent variable in the corresponding equation.

In the windward and leeward planes, the crosssflow velocity w is zero, but the derivative with respect to ξ_3 is non-zero. This problem is solved by taking the ξ_3-derivative of the w-momentum equation and solving for a new dependent variable, $\partial w/\partial \xi_3$, the derivative of w. Because of the symmetry of the body, the ξ_3-derivatives of all dependent variables except w are zero, and the second derivative of w is zero. The equation for $\partial w/\partial \xi_3$ may also be written in the standard parabolic form (A25).

The v-momentum equation can be rearranged to give an explicit expression for $\partial p/\partial y$, and the one-sided two-point differencing of the $\partial p/\partial y$ at wall can provide the boundary condition for the wall pressure. The v-momentum equation

and the continuity equation are solved simultaneously in a coupled form (Ref. 12). All density terms are removed from both equations using the equation of state for reacting flow (A12), and the resulting equations are solved for v and p simultaneously.

The shock stand-off distance may be obtained using the continuity equation. Integrating the continuity equation from the wall to the shock gives:

$$\int_0^1 \frac{\partial}{\partial \xi}(n_{sh}\rho_{sh}u_{sh}\bar{\rho}\,\bar{u}\,g^{1/2}d\eta) = -\int_0^1 \frac{\partial}{\partial \xi}(R_n n_{sh}\rho_{sh}\bar{\rho}\,w\,g^{1/2})d\eta$$

$$-\left[\rho_{sh}\bar{\rho}\,v\,g^{1/2} - \eta\frac{\partial n_{sh}}{\partial \xi}\bar{\rho}\,\rho_{sh}\bar{u}\,u_{sh}g^{1/2} - R_n\eta\frac{\partial n_{sh}}{\partial \xi}\bar{\rho}\,\rho_{sh}w\,g^{1/2}\right]_0^1 \qquad \text{(A26)}$$

The term on the left-hand side may be rewritten as

$$\text{LHS} = \frac{A_i\,n_{sh,i} - A_{i-1}\,n_{sh,i-1}}{\Delta\xi} \qquad \text{(A27)}$$

Solving for the shock-stand-off distance, n_{sh}, to obtain:

$$n_{sh} = \frac{A_{i-1}\,n_{sh,i-1} - \Delta\xi/2\,(B_i + B_{i-1})}{A_i} \qquad \text{(A28)}$$

where,

$A_i = \rho_{sh}u_{sh}\int_0^1 \bar{\rho}\,\bar{u}\,g^{1/2}d\eta$ evaluated at i axial station.

$A_{i-1} = \rho_{sh}u_{sh}\int_0^1 \bar{\rho}\,\bar{u}\,g^{1/2}d\eta$ evaluated at i-1 axial station.

B_i = left side of eqn.(A26) evaluated at i station.

B_{i-1} = left side of eqn.(A26) evaluated at i-1 station.

The energy and species conservation equations include the rate of production terms, $\dot{w}_i$, of species i, and the terms are functions of both temperature and species concentrations. The rate of production terms need to be rewritten so that the temperature or the species concentration appears as one of the unknowns. For the energy equation, the production term is written so that the temperature appears as an unknown:

$$\{\dot{w}_i/\rho\}_{k+1} = \{\dot{w}_i/\rho\}_k + \{\frac{\partial}{\partial T}(\dot{w}_i/\rho)\}_k\{T_{k+1} - T_k\} \qquad (A29)$$

where k denotes the iteration for which the solution is known and k+1 the iteration for which a solution is sought. Accordingly, the production term in the energy equation was rewritten as

$$\sum_{i=1}^{NS} h_i \dot{w}_i = \dot{w}_1 + T\,\dot{w}_2 \qquad (A30)$$

For the species conservation equation, the production term was written so that the species mass fraction appears as an unknown:

$$\dot{w}_i/\rho = \dot{w}_i{}^0 - C_i\,\dot{w}_i{}^1 \qquad (A31)$$

The governing equations described for nonequilibrium flow can be solved together with the appropriate boundary conditions, the thermodynamic and transport properties, and the chemical reaction equations.

Appendix B

DERIVATION OF BOUNDARY CONDITIONS

At the body surface, no-slip boundary conditions are:

$$u = v = w = 0, \quad T = T_w \tag{B1}$$

where, T_w is either a constant or a specified distribution. The wall pressure is obtained from one-sided differencing of v-momentum equation. For the wall-slip case without mass-transfer, the equations for slip-velocity and slip-temperature are given by Hendricks (Ref. 14). The value of molecule-surface accommodation coefficient used is one ($\theta = 1$). The original equations are rewritten in the present general coordinate system as following:

$$u_s = \sqrt{\pi}\,(\mu_s \varepsilon^2 / p_w / M_\infty)\ \{\ \text{TERM1}/2 \sqrt{\frac{2T_s}{\gamma T_\infty}}\ \sqrt{g_{11}}\ \frac{\partial u}{\partial \xi_2}\ \}_s \tag{B2}$$

$$w_s = \sqrt{\pi}\,(\mu_s \varepsilon^2 / p_w / M_\infty)\ \{\ \text{TERM1}/2 \sqrt{\frac{2T_s}{\gamma T_\infty}}\ \sqrt{g_{33}}\ \frac{\partial w}{\partial \xi_2}\ \}_s \tag{B3}$$

$$T_s = (\text{SUM1} + \text{SUM2})/\text{SUM3} \tag{B4}$$

$$C_{i,s} = \frac{(2-\gamma_i)/(2\gamma_i)\ \varepsilon^2 M_\infty \text{Le}\ \mu_s/(\text{Pr}\ \rho_s)\sqrt{\frac{2\pi r M_i T_\infty}{\bar{M} T_s}}\,\text{TERM3}}{1 + \varepsilon^2 M_\infty^2 \mu\ \gamma\ M_i T_\infty\ \text{TERM2}\ /\ (3\ \rho\ T\ C_i\ \bar{M})} \tag{B5}$$

where,

$$\text{SUM1} = \sum_i T_w \rho\ C_i\ (\bar{M}/M_i)^{3/2}\ \{1 + (\mu\ \varepsilon^2/3/p_i)\ \text{TERM2}$$

$$+ (\sqrt{\pi}/C_i)\ \text{TERM1}\ (\varepsilon^2 M_\infty \text{Le}/\text{Pr})(M_i/\bar{M})(\mu/\rho)\sqrt{\frac{\gamma M_i T_\infty}{2\bar{M}T}}\ \text{TERM3}\}_s$$

$$SUM2 = TERM1\sqrt{\pi}\{(\varepsilon^2 M_\infty \mu/2/Pr)\ \gamma/(\gamma-1)\sqrt{\frac{\gamma T_\infty}{2T}}\ \frac{\partial T}{\partial \xi_2}$$

$$- (5p/2/\rho)\ \varepsilon^2 \mu\ M_\infty^{\ 3}\gamma\ T_\infty\sqrt{\frac{\gamma T_\infty}{2T}}\ (Le/Pr)\ TERM3\}_s$$

$$SUM3 = \{\sum_i \rho\ C_i\ (\bar{M}/M_i)^{3/2}\ (1 + TERM2\ \varepsilon^2\mu/2/p_i)\}_s$$

$$TERM1 = (2-\theta)/\theta$$

$$TERM2 = \frac{\partial u}{\partial \xi_1} + \frac{\partial w}{\partial \xi_3} - 2\frac{\partial v}{\partial \xi_2}$$

$$TERM3 = \sum_j \{\frac{\partial C_j}{\partial \xi_2}\}_s$$

In the present study, the species wall-slip is not included, but the surface catalysis effect are analyzed by the following method. For a nonequilibrium flow over a finite-catalytic wall, the wall species concentration is dictated by the catalytic recombination rate k_w^* in the following expression:

$$\partial C_i/\partial\eta - (k_{wi}\rho\ Pr/Le/\mu/\varepsilon^2)\ C_i = 0 \qquad (B6)$$

where $k_{wi} = k_{wi}^*/U_\infty$ is a nondimensionalized recombination rate. The catalytic recombination coefficient γ_i is related to k_w^* by

$$\gamma_i = \sqrt{2\pi M_i^*/R^*/T^*}\ \ k_{wi}^* \qquad (B7)$$

The recommended curve-fit expressions by Scott (Ref. 6) are:

$$\gamma_N = 0.071\ \exp(-2219/T_w),\quad 1670K > T_w > 950K \qquad (B8)$$

$$\gamma_O = 16.0 \exp(-10271/T_w), \quad 1650K > T_w > 1400K \tag{B9}$$

The above two equations may be rewritten for k_w as

$$k_{wN} = 69.484 \; T_w \exp(-2219/T_w) \; ; \text{(cm/sec)} \tag{B10}$$

$$k_{wO} = 14564. \; T_w \exp(-10271/T_w) \; ; \text{(cm/sec)} \tag{B11}$$

The curve-fit relations for oxygen given by Rakich (Ref. 8) are:

$$k_{wO} = 66000. \exp(-8017/T_w), \text{ for } 2000K > T_w > 862K \tag{B12}$$

$$k_{wO} = 53. \exp(-1875/T_w), \text{ for } 862K > T_w > 500K \tag{B13}$$

Using the calculated catalytic recombination rate, the equation (B4) may be used to provide the wall boundary conditions for the species. The one-sided two-point differencing gives the necessary coefficients for the finite-difference solution. For the concentration of oxygen molecules at the wall, the mass-diffusion balance with oxygen atoms may be used.

For a noncatalytic surface, the species boundary conditions are simple and given by

$$\partial C_i/\partial \eta = 0 \tag{B14}$$

The equilibrium-catalytic wall condition is specified by

$$C_{iw} = C_{iw}\,(T_w) \tag{B15}$$

For low surface temperatures, the equilibrium-catalytic wall condition may be approximated by a fully-catalytic surface condition specified by

$$C_{O_2} = 0.23456,\ C_{N_2} = 0.76544,$$

$$C_O = C_N = C_{NO} = C_{NO^+} = 0 \tag{B16}$$

The present method has also been extended to include the nonequilibrium shock-slip model. For shocks of finite thickness (called shock-slip condition), the shock properties are given by the modified Rankine-Hugoniot relations (Refs. 3,21). The shock-crossing equations are written in the shock surface-normal coordinate system. In this coordinate system, the shock crossing is reduced to the simple two-dimensional oblique shock crossing. The freestream velocity vector must be written in the shock surface-normal coordinate. In the following equations, u and v are the velocity components in the shock surface-normal coordinate system.

$$\hat{u}_{sh} = \frac{\cos\sigma}{1 + \dfrac{\varepsilon^2}{n_{sh}}\dfrac{\mu_{sh}}{\sin\sigma}\left(\dfrac{\partial \hat{u}}{\partial \eta}\right)} \tag{B17}$$

$$T_{sh} = \frac{0.5(\hat{u}_{sh}-\cos\sigma)^2 + 0.5(\sin^2\sigma-\hat{v}_{sh}^2) + \sum_{i=1}^{NS} C_{i_\infty} h_{i_\infty}}{\sum_{i=1}^{NS} C_{i_\infty}\left(\dfrac{h_{i_{sh}}}{\bar{T}_{sh}}\right) + \dfrac{\varepsilon^2}{n_{sh}}\dfrac{k_{sh}}{\sin\sigma}\left(\dfrac{\partial \bar{T}}{\partial \eta}\right)} \tag{B18}$$

$$p_{sh} = \frac{p_\infty}{\rho_\infty U_\infty^2} + \sin\sigma\,(\hat{v}_{sh} + \sin\sigma) \tag{B19}$$

$$\rho_{sh} = \frac{p_{sh}}{T_{sh}\left(\frac{R}{C_{p_{ref}}}\right)} \tag{B20}$$

$$\hat{v}_{sh} = -\frac{\sin\sigma}{\rho_{sh}} \tag{B21}$$

$$C_{i_{sh}} = C_{i_\infty} - \varepsilon^2\left(\frac{\mu Le_i}{Pr}\right)_{sh} \frac{1}{n_{sh}} \frac{\partial C_i}{\partial \eta} \frac{1}{\sin\sigma} \tag{B22}$$

Since some of the above equations are coupled with each other, an iterative method is used until a converged after-shock temperature is obtained. The after-shock species concentrations are obtained using the converged temperature. The solved after-shock velocity components in the shock-normal coordinate system are rotated into the nonorthogonal computational coordinate system.

Appendix C

DESCRIPTION OF DEVELOPED COMPUTER CODE

The FORTRAN computer code, SHTNEQ (shuttle-nonequilibrium), described in this appendix has been developed to predict the three-dimensional nonequilibrium flowfield past the space shuttle orbiter at high angles-of-attack (up to 50-deg). A previous perfect gas viscous shock-layer code by Szema and Lewis (Ref. 9) has been extended to include finite-rate chemical reactions of multi-component ionizing air. A general nonorthogonal computational grid system was used to treat the nonaxisymmetric shuttle geometry. The routines related to the chemical reactions are written based on the previous two-dimensional viscous shock-layer code by Miner and Lewis (Ref. 1). The flow over the axisymmetric nose-cap is solved by the VSLNEQ code which has been developed by Swaminathan, Kim, and Lewis (Ref. 29). The solution over the nose-cap is used to prepare an intial data plane which can be used to solve the three-dimensional main-body flowfield.

The viscous shock-layer equations are principally parabolic but have a slight elliptic effect from the downstream shock. This problem may be resolved by a few global iterations. The initial input shock is obtained from an inviscid

solution in general. The SHTNEQ code prints out the output shock shape on Unit 07 which may be used for global iterations after smoothing if necessary. The global iteration is not necessary if the inviscid solution yields a reasonable prediction of the shock.

Since the shock-layer equations are parabolic, they cannot accurately predict the crossflow separated region that occurs on the lee-side of the long bodies at high angles-of-attack. For this reason the code will drop ϕ-planes as it marches around the body into the separated region. The code has the option of automatically dropping a plane when it encounters a negative temperature or the user may avoid the separated region altogether by using the option which computes the flow over a specified number of ϕ-planes. For the shuttle geometry at high angle-of-attack, the solution is usually obtained up to 90-deg around the body.

As the solution approaches a separated region it becomes more sensitive to the streamwise pressure gradient. The pressure gradient may be specified in a number of ways. The first option is to assume zero pressure gradient. The second option uses an explicit determination of the pressure gradient using the pressures at the previous two axial stations. The third option allows an implicit calculation of

the pressure gradient using the pressures at the current station and the previous station. The fourth option uses the implicit calculation on the windward planes where the solution is not very sensitive to the streamwise pressure gradient, but assumes a zero pressure gradient in the leeward planes. In the case of very high angle-of-attack, a local convergence problem along the body with the implicit model may be resolved by using the explicit or zero pressure gradient model. Some oscillatory divergence problems may be resolved by applying a damping factor during the local iterations. In most cases, an accurate input shock is one of the most crucial factors for a convergent solution.

On the spherical nose a small s-stepsize is used. This is gradually increased on the afterbody in subroutine CHANGE. DS1 is the initial stepsize desired, and the stepsize is increased considering the number of iterations taken at each marching station. Careful adjustment of the marching stepsize is very important for both the stability and the accuracy of the solution.

The solution begins on the spherically blunted nose by obtaining an axisymmetric solution in the wind-fixed coordinate system. The axisymmetric solution is rotated into the body fixed coordinates and is used as the initial profile

for the three-dimensional solution. The three-dimensional solution begins in the windward plane and marches around the body. After completing a sweep around the body at a marching station, the procedure then steps downstream along the body, and begins the sweep again around the body. At each marching station the equations are solved in the following order: (i) species, (ii) w-momentum, (iii) energy, (iv) u-momentum, (v) integration of continuity for shock-layer thickness, and (vi) the coupled continuity and normal momentum equations. The program continues marching down the body until the last s-location is reached. A flow diagram of the solution procedure is shown in Sketch (C1).

The input data for the SHTNEQ code are on three separate units. The control and freestream variables and wall boundary conditions are input on Unit 01. The second unit (Unit 10) contains the shock shape and body geometry which is used in defining the shock-crossing and body boundary conditions. The chemical reaction rate data are read in on Unit 18. The output from the SHTNEQ code is on three major units (Units 06, 07 and 21). The major portion of the output is on Unit 06 which gives the complete flowfield solution and wall conditions. Unit 07 punches the calculated shock shape and the body geometry which can be used as input (Unit 10) for a later calculation for global iteration.

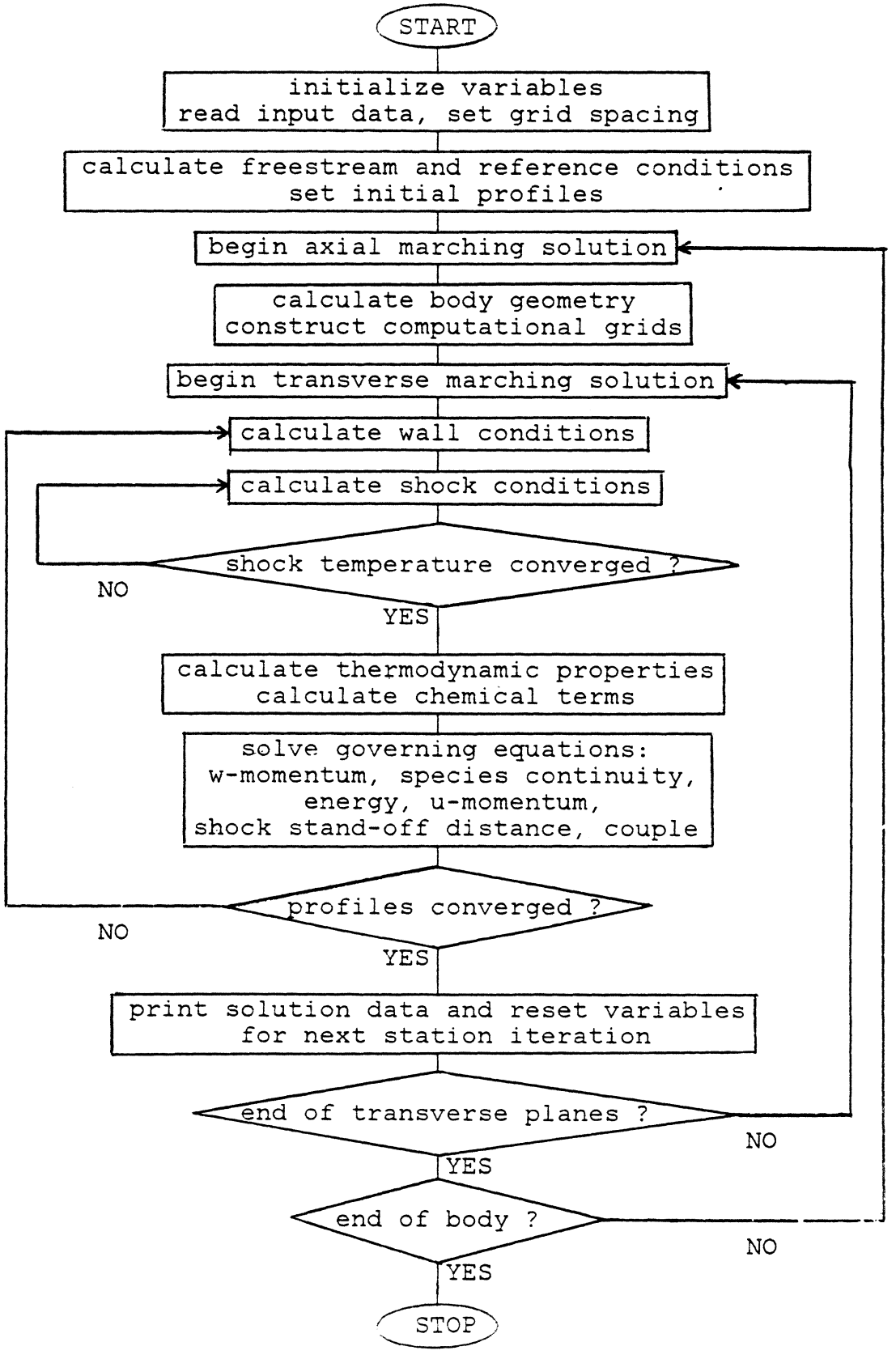
START
initialize variables
read input data, set grid spacing
calculate freestream and reference conditions
set initial profiles
begin axial marching solution
calculate body geometry
construct computational grids
begin transverse marching solution
calculate wall conditions
calculate shock conditions
shock temperature converged ?
NO
YES
calculate thermodynamic properties
calculate chemical terms
solve governing equations:
w-momentum, species continuity,
energy, u-momentum,
shock stand-off distance, couple
profiles converged ?
NO
YES
print solution data and reset variables
for next station iteration
end of transverse planes ?
NO
YES
end of body ?
NO
YES
STOP

Sketch (C1)

Unit 21 contains the wall-measurable quantities for plotting purposes. In addition to the above three output units, there are some optional output units (Units 11,22,23,26,27,30, and 31). Unit 11 contains the iteration informations (number of iterations taken at each marching step). Unit 22 has the same content as Unit 21, but it gives a punch file for plotting instead of a hard-copy print. Unit 23 gives an internally calculated shock angle distribution that can be used to check smoothness of input shock data. Units 26,27,30 and 31 are tapes for a restart solution.

The SHTNEQ code requires about 850 kilobites in IBM (361 kilo-octal-words in CDC) for excution. The core requirement varies according to the number of chemical species and also the number of grid-points used. The CPU execution time taken for the entire windward solution over the shuttle orbiter is about 90 minutes in an IBM 370/3081 (similar time on the CYBER-175). Typical grid-points used in the present analysis are 51 normal-grids, 10 planes around the body and 130 axial stations, and for the chemical reactions, seven(7) species are considered.

Since a complete nonequilibrium viscous flowfield solution for the entire windward surface of the shuttle geometry

takes more than one hour of computing time, one may need to obtain the solution for a part of the body and then restart the solution later for the rest of the body. Units 26,27,30 and 31 are output tapes for a future restart. When a solution is completed at a marching station along the body, the flowfield profile is automatically saved in the Unit 26 or 27, and the metric information data are saved in the Unit 30 or 31 alternatively. In order to restart a solution, the flowfield profile tape (Unit 26 or 27) should be copied to Unit 08 to be used as input data. Likewise, Unit 30 or 31 (metric data) is copied to Unit 35 to be used as input. For a restart, START in the Unit 01 should be set to the value of the s-station where the restart flowfield profile is saved. Also, the value of initial axial step-size DS1 must be set equal to the last step-size in the previous run. A complete description of the computational variables, subroutines, common blocks, input and output data, and some sample runs will be given in the SHTNEQ User's Manual.

Appendix D

METHODS OF SHOCK SHAPE GENERATION

The present method requires a shock shape over the entire body as input. Generally the necessary shock shape data are provided from an inviscid calculation using BLUNT-STEIN (Refs. 16,17) or HALIS (Ref. 13) code. The shock data for the present test cases at high angles-of-attack were provided by the HALIS method. The inviscid shock data need some interpolations and coordinate transformations in order to be used as input for SHTNEQ. For this purpose, the following five procesures can be used with a corresponding small code at each step.

1. GRVSL : This code reads in the shock shape from the nose part of the solution (e.g. BLUNT solution) and interpolates for RSH as a function of ZSH for a fixed number of planes (NOPHI) around the body.

2. SHUTINT : This code reads in the shock shape from the afterbody solution (e.g. STEIN solution) and interpolates for RSH as a function of ZSH for a fixed number of planes (NOPHI) around the body.

3. NSH3D : This code uses the SUBQUICK routines and the output of GRVSL and SHUTINT to find the shock stand-off dis-

tance, the shock angle and the surface distance for fixed Z steps. Unit 5 consists of the QUICK geometry input deck, then a card with NOPHI, ZEND, DZ, RNOSE (I5,3E10.5), and then the output of GRVSL and SHUTINT.

4. NSH3DI : This code interpolates the NSH3D output to obtain the values of the shock shape variables at constant values of S/RN. Unit 5 consists of the QUICK geometry input deck, then a card with NOPHI, NX, DS, SMAX, RNOSE (2I5,3E10.5), where NX is the number of axial stations of the input (i.e. NSH3D output), and then the NSH3D output.

5. NSH3DS : This code smooths the quantities previously computed by using a walking least squares fit. Unit 5 consists of the NSH3DI output.

Some of the above five codes use IMSL routines for curve-fits and interpolations. The input to each code is usually on Unit 5, while the output is on Unit 8. Generally Unit 6 contains some debugging information. The Unit 8 output usually goes to the next code as input along with some other data. Each code has a small size and simple procedure, and hence they may be combined together. But, it is desirable to plot all the quantities at the end of each step in order to ensure smoothness of shock shape.

Table 1. Test Case Freestream Conditions

Case No.	t sec	Alt. km	α deg	M_∞	Re_∞ m^{-1}	U_∞ km/s	T_∞ K	p_∞ atm
1	250	85.74	41.0	26.6	2726.	7.53	199.	3.587E-06
2	460	74.98	40.0	25.5	15686.	7.20	198.	2.142E-05
3	650	71.29	39.4	23.4	25756.	6.73	205.	3.965E-05

Table 2. Reaction Equations and Catalytic Third Bodies

Reaction Equations									
r = 1	O_2	+	M_1	=	2O	+	M_1		
2	N_2	+	M_2	=	2N	+	M_2		
3	N_2	+	N	=	2N	+	N		
4	NO	+	M_3	=	N	+	O	+	M_3
5	NO	+	O	=	O_2	+	N		
6	N_2	+	O	=	NO	+	N		
7	N	+	O	=	NO^+	+	e^-		

Catalytic Third Bodies Efficiencies Relative to Argon

		O	O_2	NO	N	NO^+	N_2
M_1	I I	25	9	1	1	0	2
M_2	I I	1	1	1	0	0	2.5
M_3	I I	20	1	20	20	0	1
e^-	I	0	0	0	0	1	0

Table 3. Reaction Rate Constants

T_k in degrees Kelvin

$$k_{fr} = T_k^{(C2_r)} \exp(C0_r - C1_r/T_k)$$

$$k_{br} = T_k^{(D2_r)} \exp(D0_r - D1_r/T_k)$$

Reaction No.	$C0_r$	$\exp(C0_r)$	$C1_r$	$C2_r$	$D0_r$	$\exp(D0_r)$	$D1_r$	$D2_r$
r = 1	42.7302	$3.61*10^{18}$	59,400	-1	35.6407	$3.01*10^{15}$	0	-1/2
r = 2	39.7963	$1.92*10^{17}$	113,100	-1/2	36.9275	$1.09*10^{16}$	0	-1/2
r = 3	52.0800	$4.15*10^{22}$	113,100	-3/2	49.1959	$2.32*10^{21}$	0	-3/2
r = 4	47.4305	$3.97*10^{20}$	75,600	-3/2	46.0617	$1.01*10^{20}$	0	-3/2
r = 5	21.8801	$3.18*10^{9}$	19,700	1	27.5933	$9.63*10^{11}$	3600	1/2
r = 6	31.8431	$6.75*10^{13}$	37,500	0	30.3391	$1.50*10^{13}$	0	0
r = 7	22.9238	$9.03*10^{9}$	32,400	1/2	44.3369	$1.80*10^{19}$	0	-1

Table 4. Computing Times[a] for Test Cases

Flow Model	Case No.	z/L from - to	Number of Grids in ξ_1	ξ_2	ξ_3	CPU time (H:M:S)
NONEQL (finite-catalytic)	1	0. - 0.93	127	51	10	1:22:47
	2	0. - 0.93	129	51	10	1:40:32
	3	0. - 0.93	142	51	10	1:43:03
NONEQL (non-catalytic)	1	0. - 0.93	127	51	10	1:20:34
	2	0. - 0.93	129	51	10	1:50:28
	3	0. - 0.93	142	51	10	1:51:50
NONEQL (fully-catalytic)	1	0. - 0.93	123	51	10	1:23:02
	2	0. - 0.93	124	51	10	1:26:53
	3	0. - 0.93	124	51	10	1:27:22
Perfect Gas	1	0. - 0.50	78	101	10	0:07:07
	2	0. - 0.50	78	101	10	0:07:06
	3	0. - 0.50	78	101	10	0:07:05
Equilibrium	1	0. - 0.453	72	101	10	0:08:32
	2	0. - 0.453	72	101	10	0:08:28
	3	0. - 0.453	72	101	10	0:08:27

a CPU time on IBM 370/3081, H=OPT2 compiler

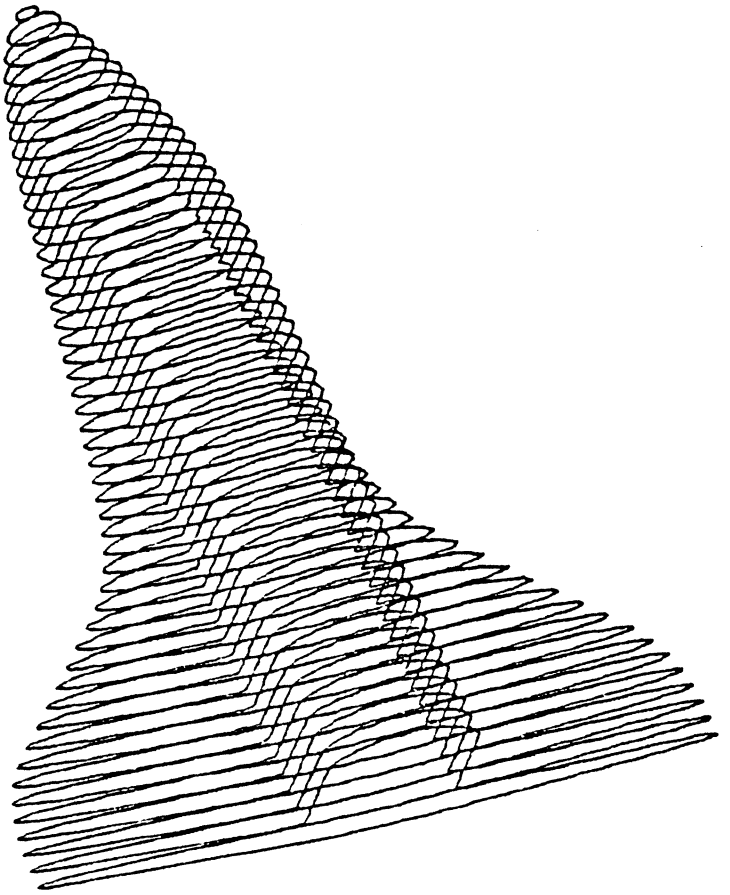

Figure 1. Shuttle orbiter geometry described by QUICK geometry package

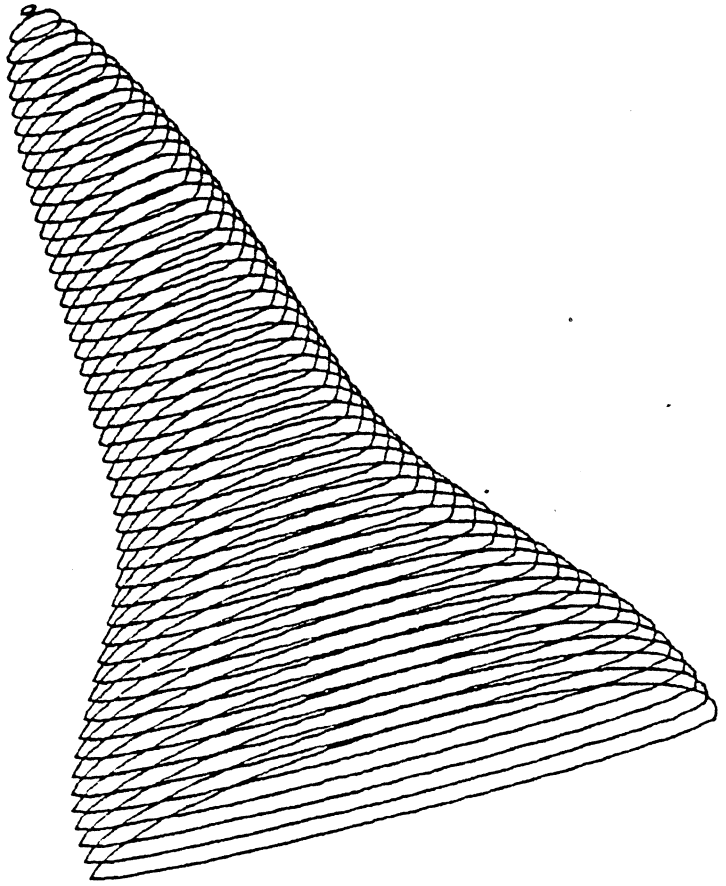

Figure 2. Modified shuttle orbiter geometry described by QUICK geometry package

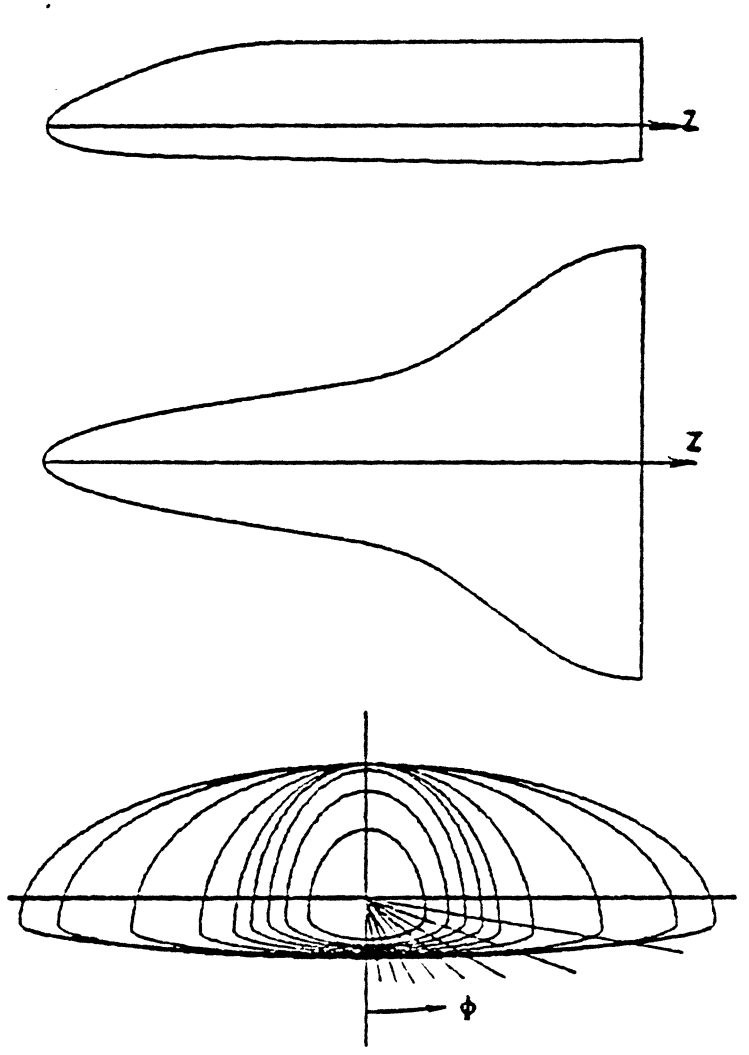

Figure 3. Cross-sections of the modified shuttle orbiter

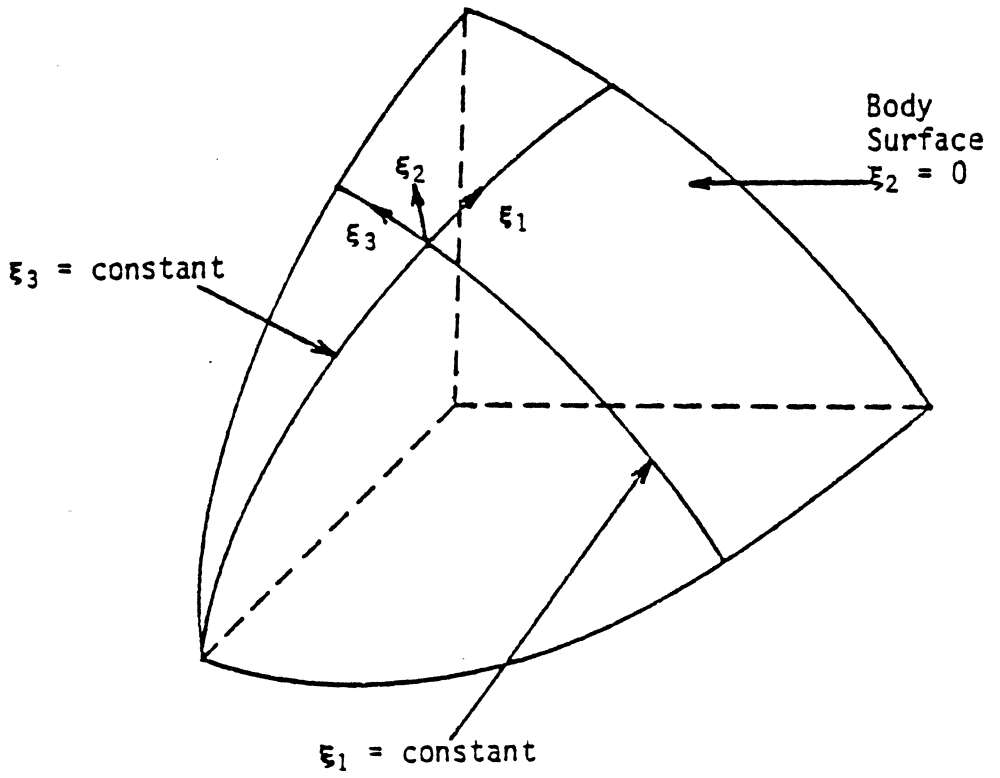

Figure 4. Body-generator nonorthogonal coordinate system

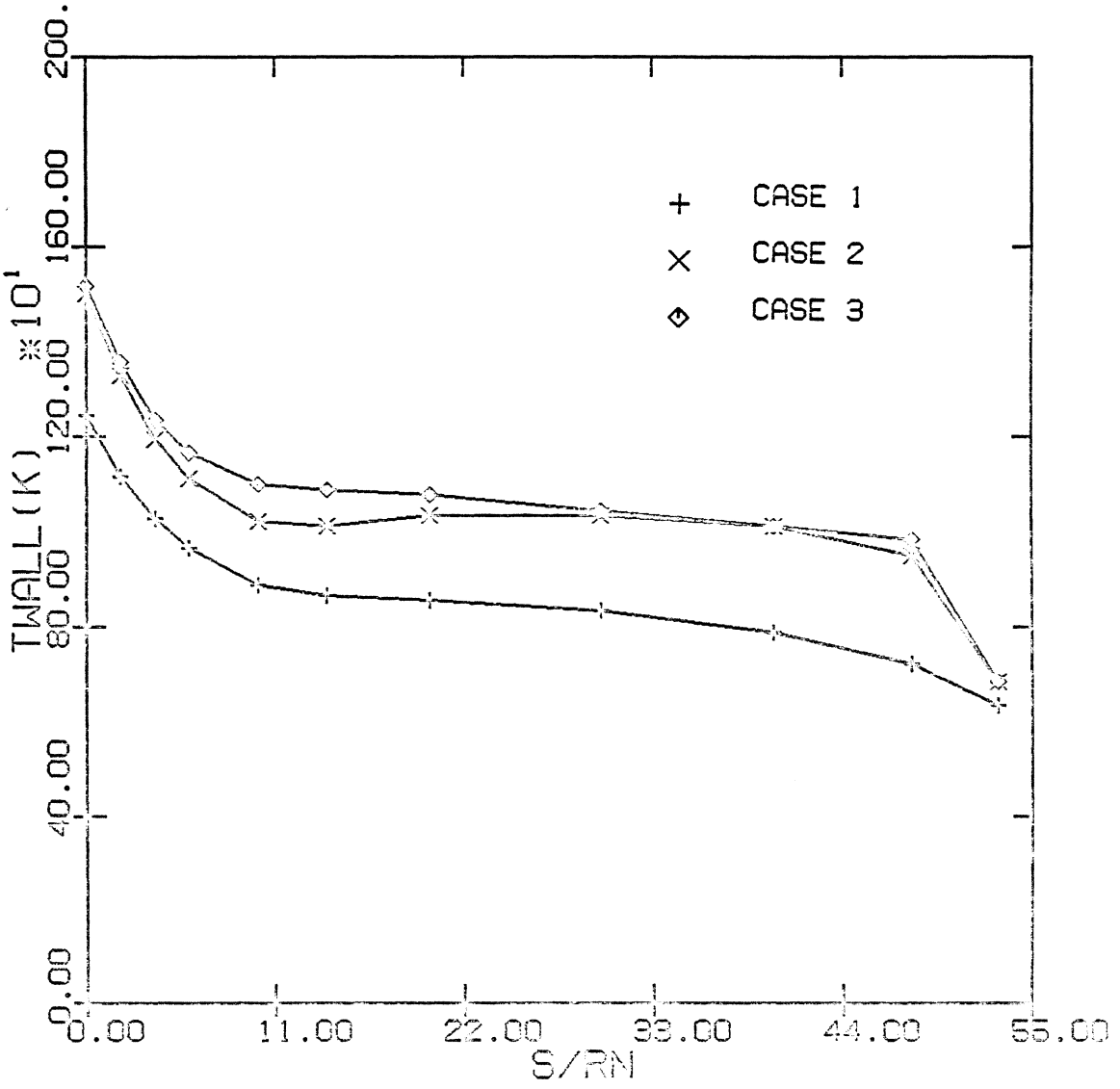

Figure 5. Surface temperature distributions for the test cases

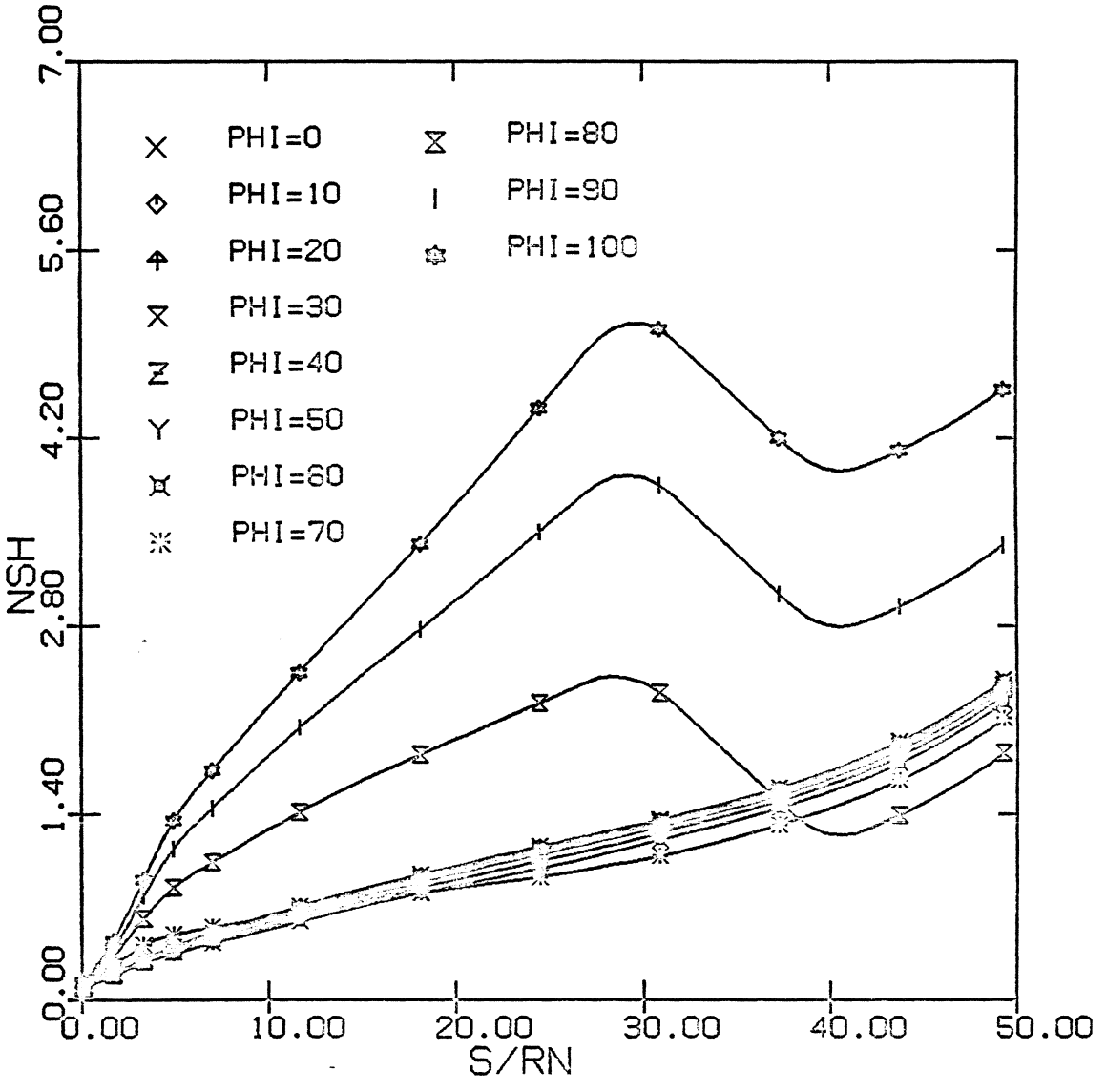

Figure 6. Distribution of shock stand-off distance used as input data for nonequilibrium solution for Case 1

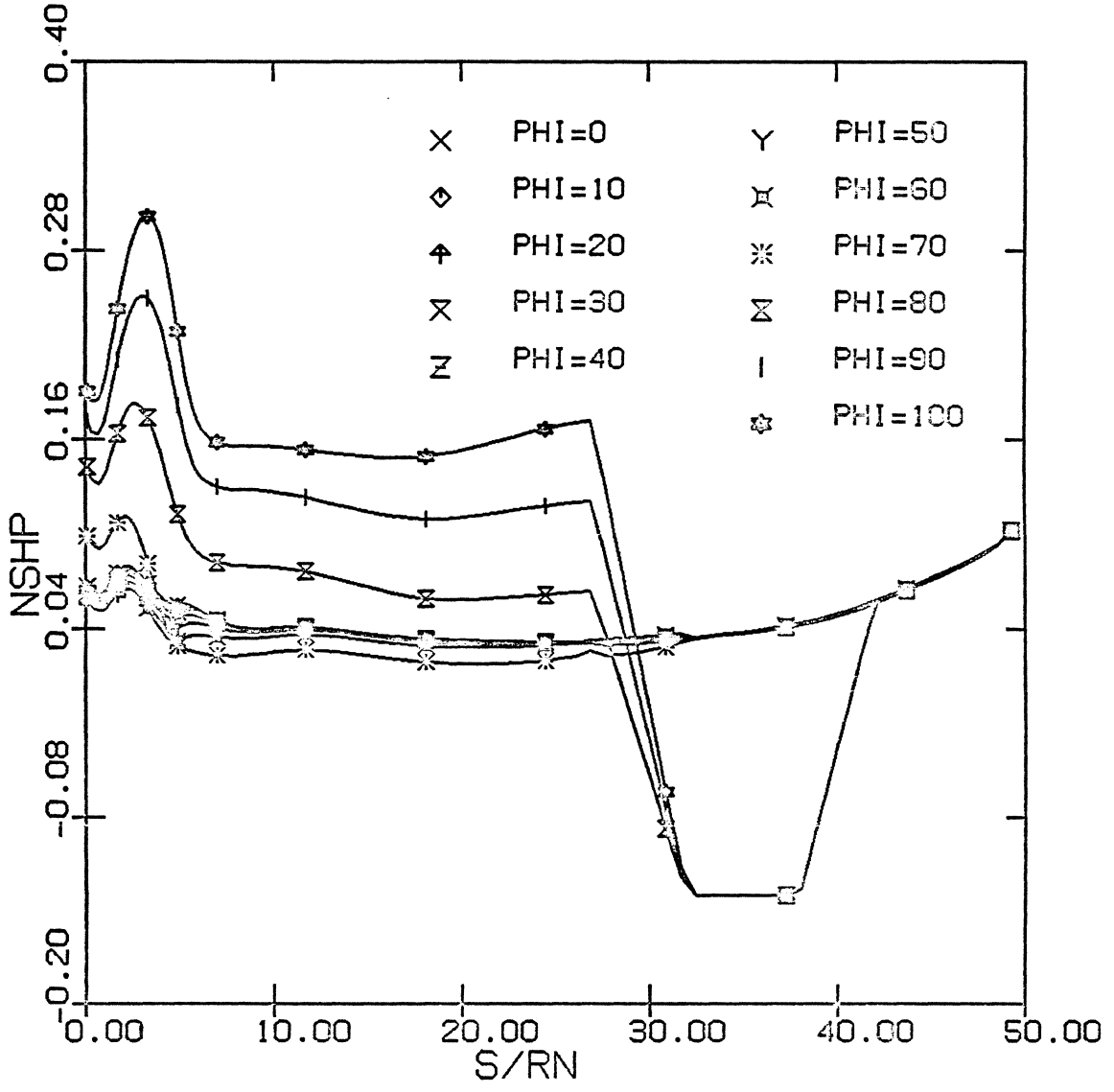

Figure 7. Distribution of shock slope along body used as input data for nonequilibrium solution for Case 1

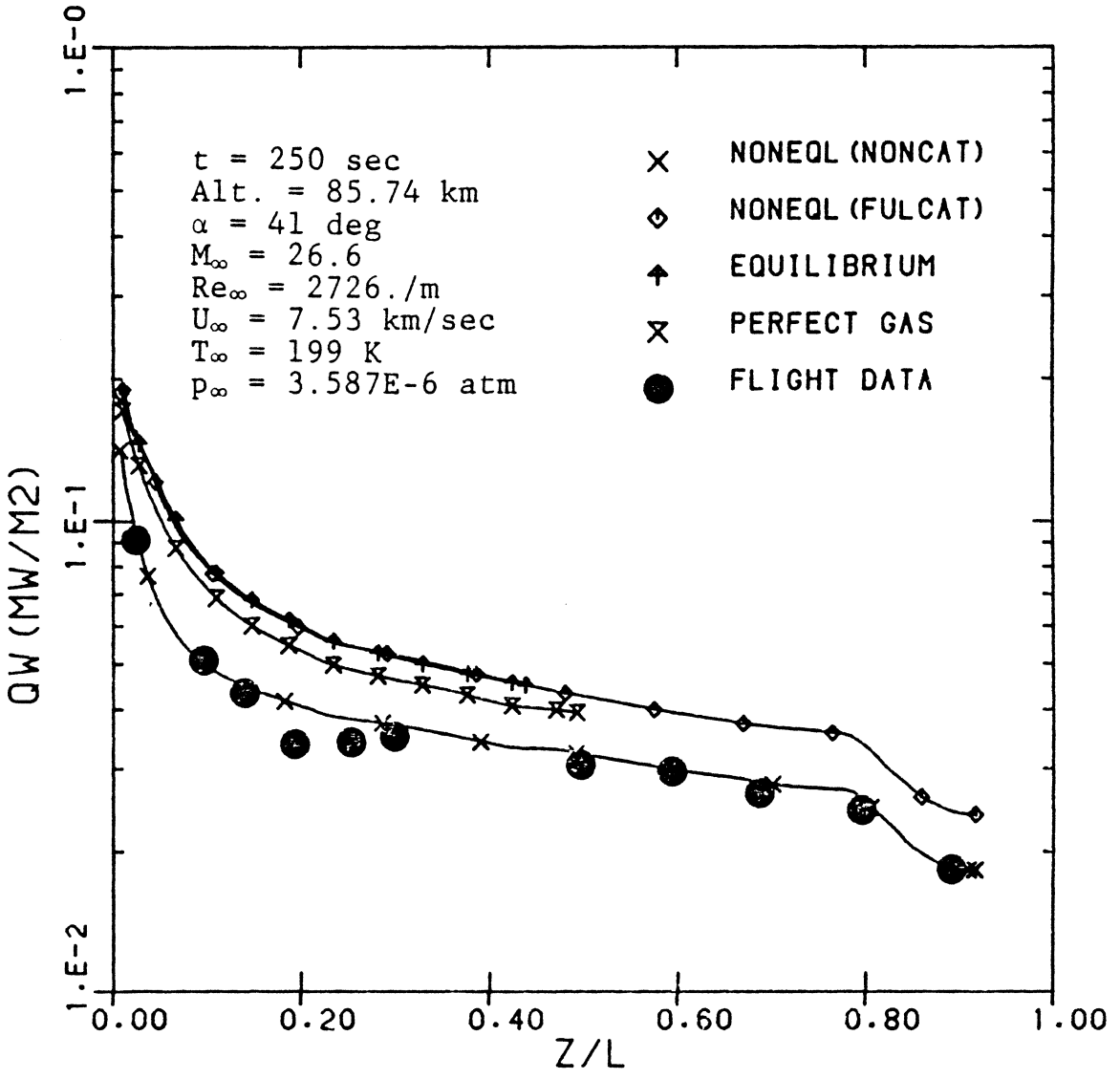

Figure 8. Comparison of measured and calculated heating rates along the windward centerline of Case 1

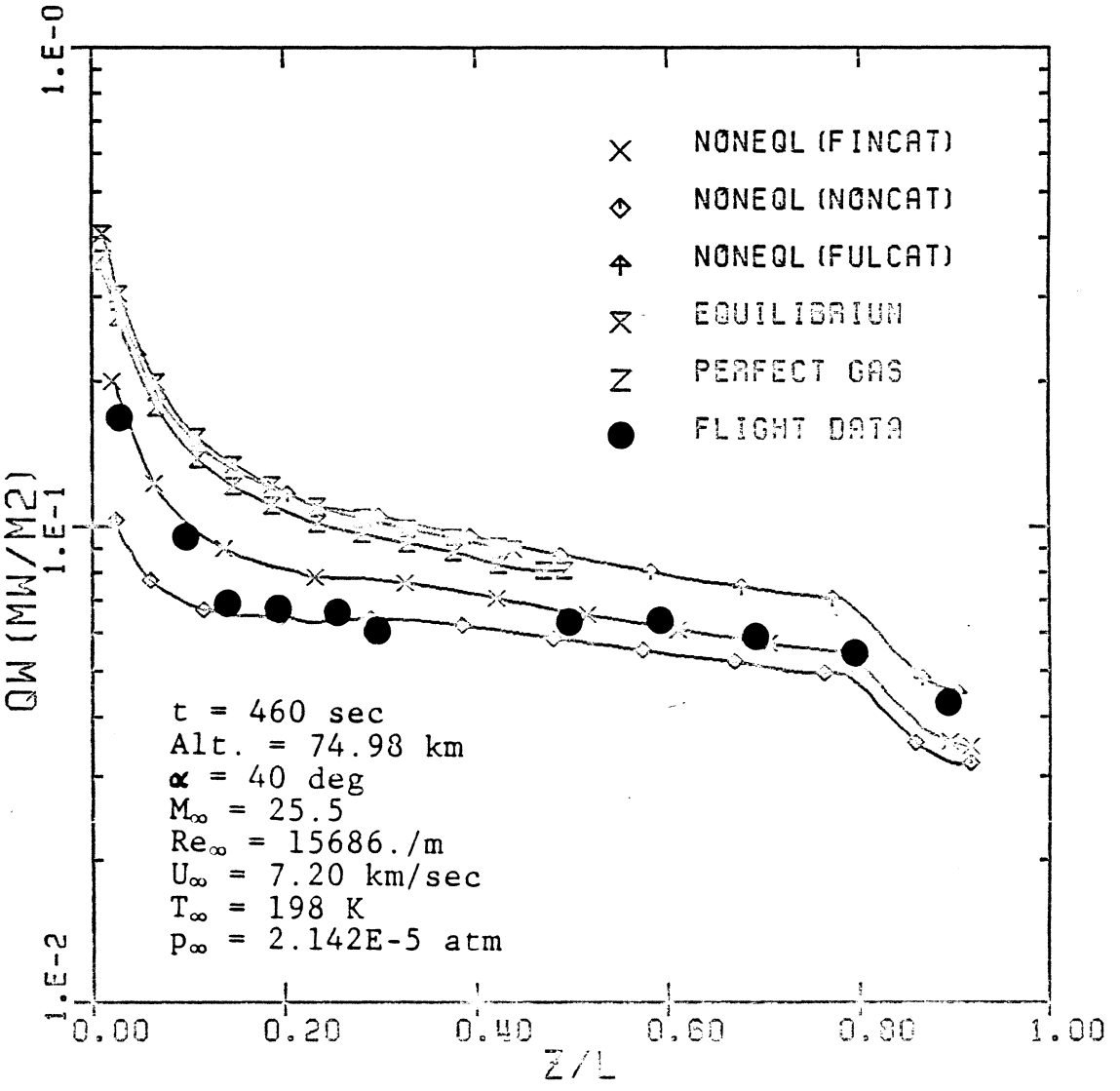

Figure 9. Comparison of measured and calculated heating rates along the windward centerline of Case 2

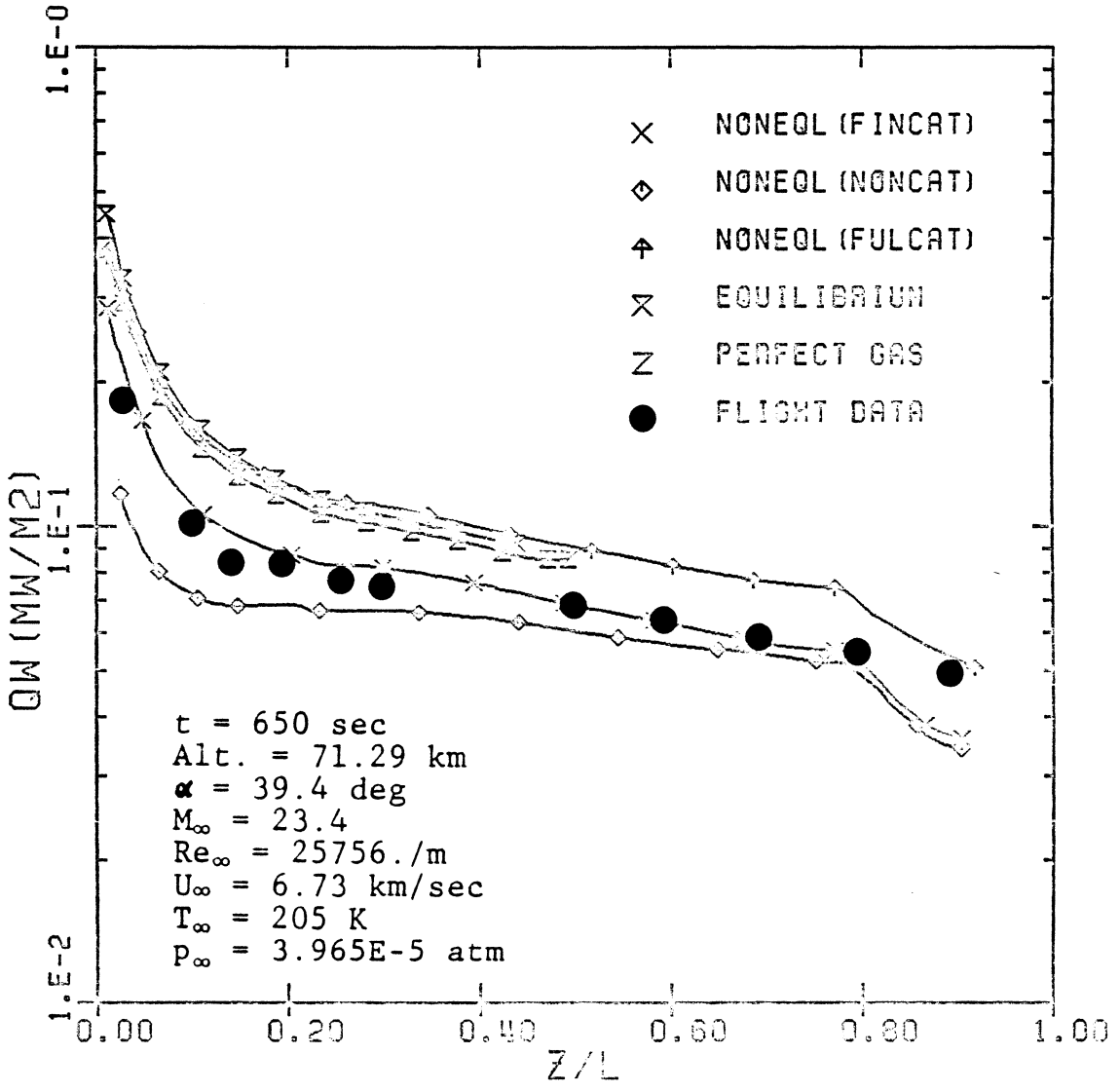

Figure 10. Comparison of measured and calculated heating rates along the windward centerline of Case 3

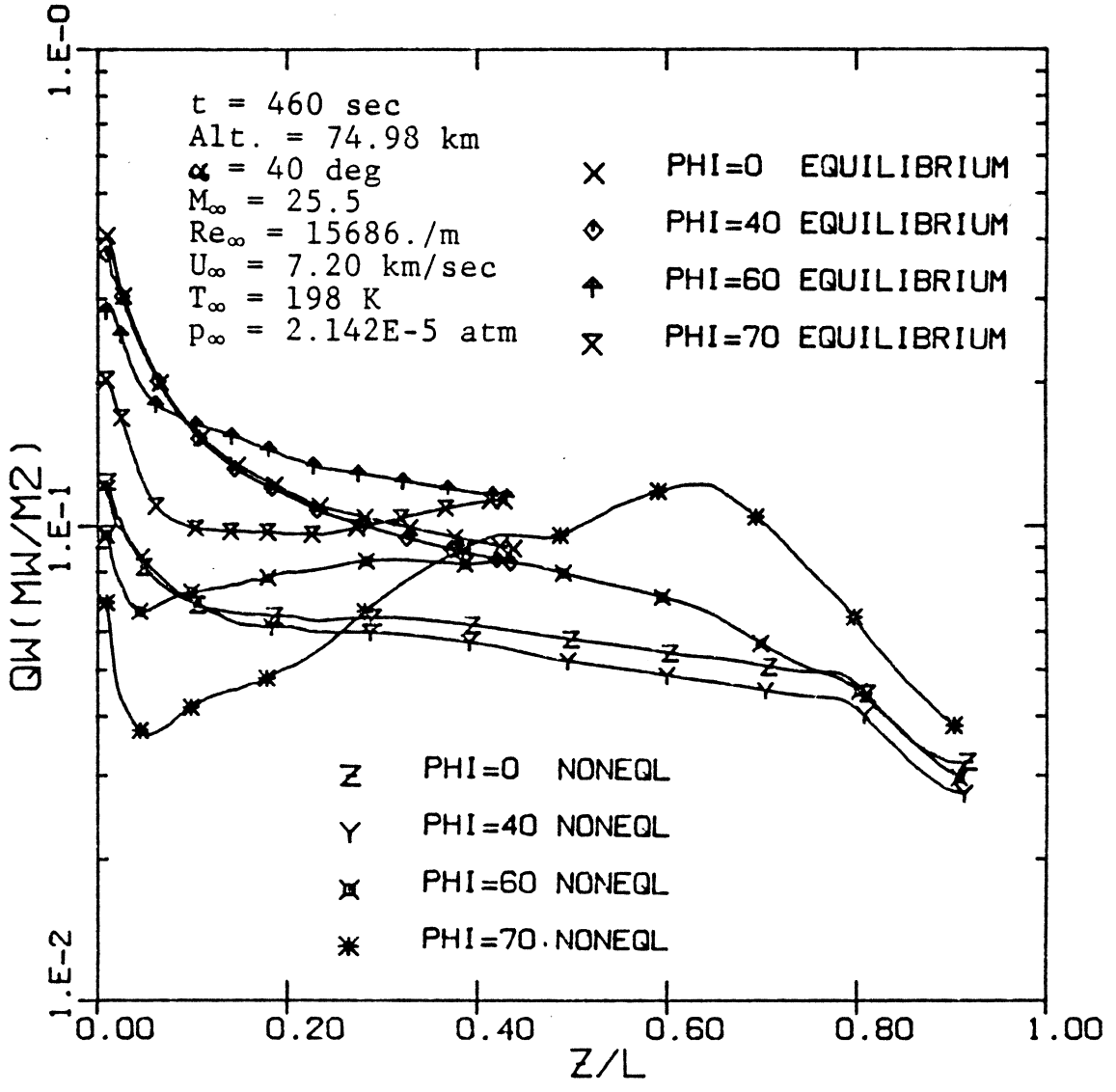

Figure 11. Surface heating-rate distributions along the body for different ϕ-planes for Case 2

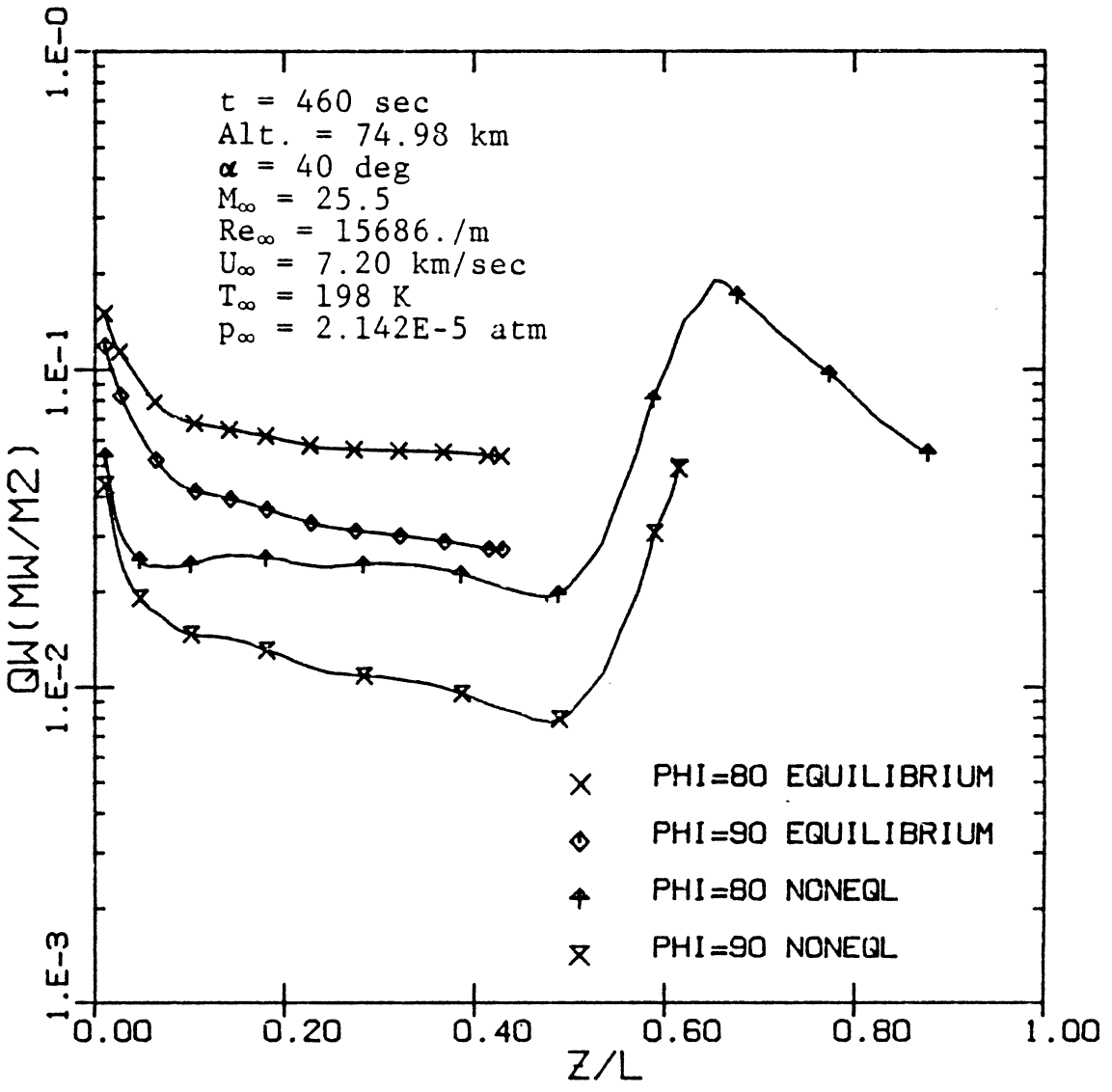

Figure 11. Surface heating-rate distributions along the body for different ϕ-planes for Case 2 (continued)

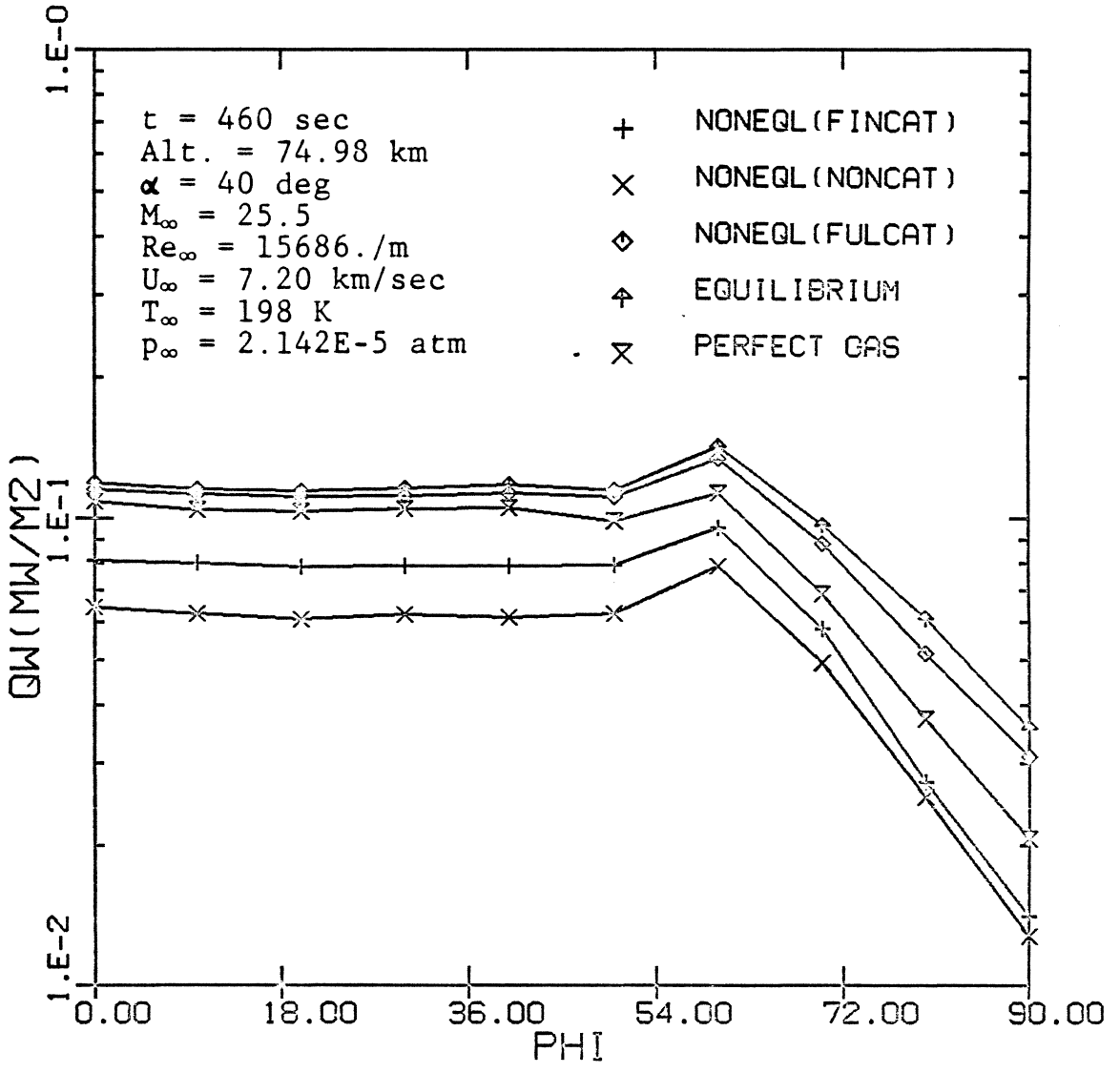

Figure 12. Comparison of spanwise heating-rate distributions at z/L = 0.2 for Case 2

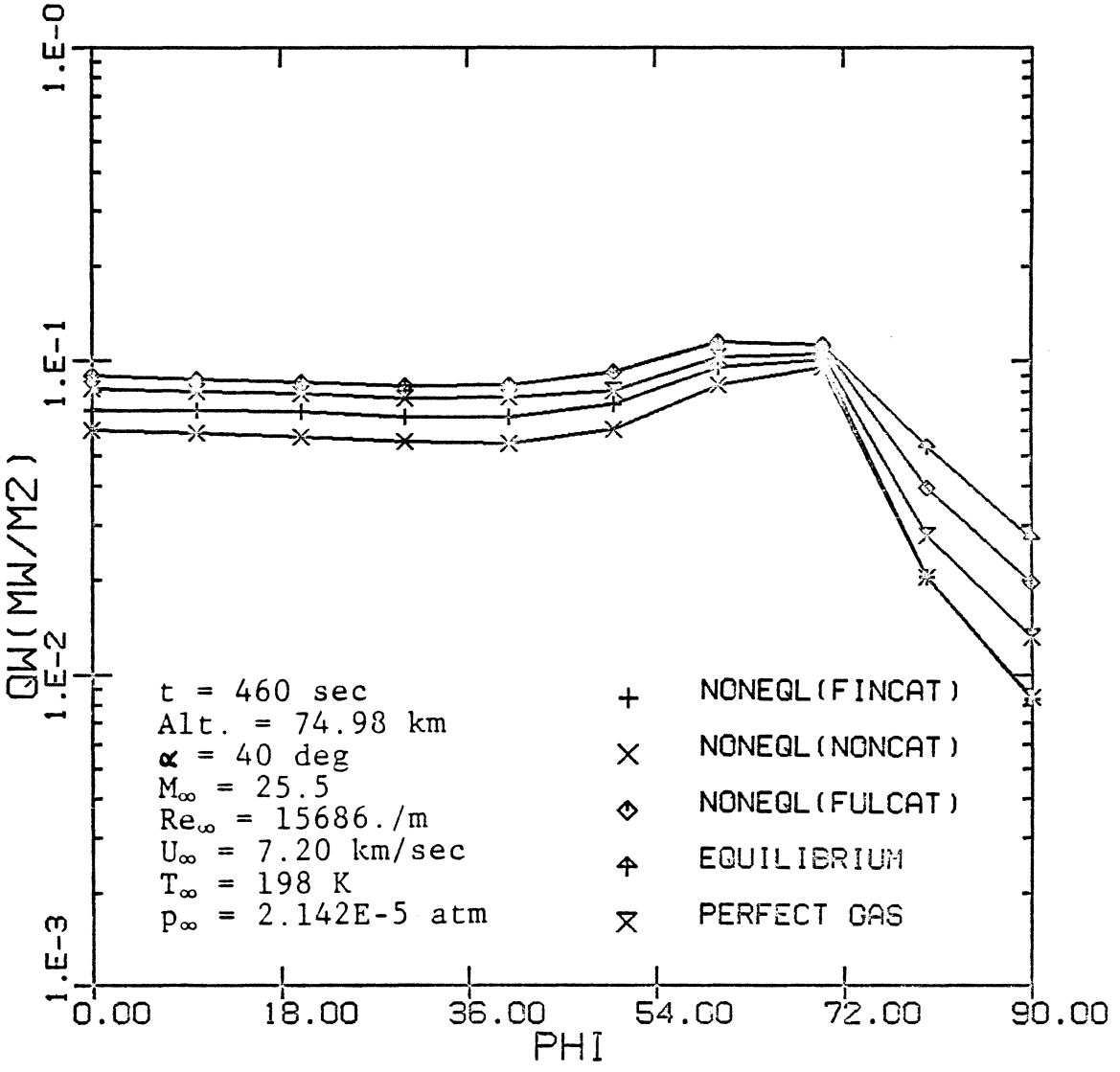

Figure 13. Comparison of spanwise heating-rate distributions at z/L = 0.44 for Case 2

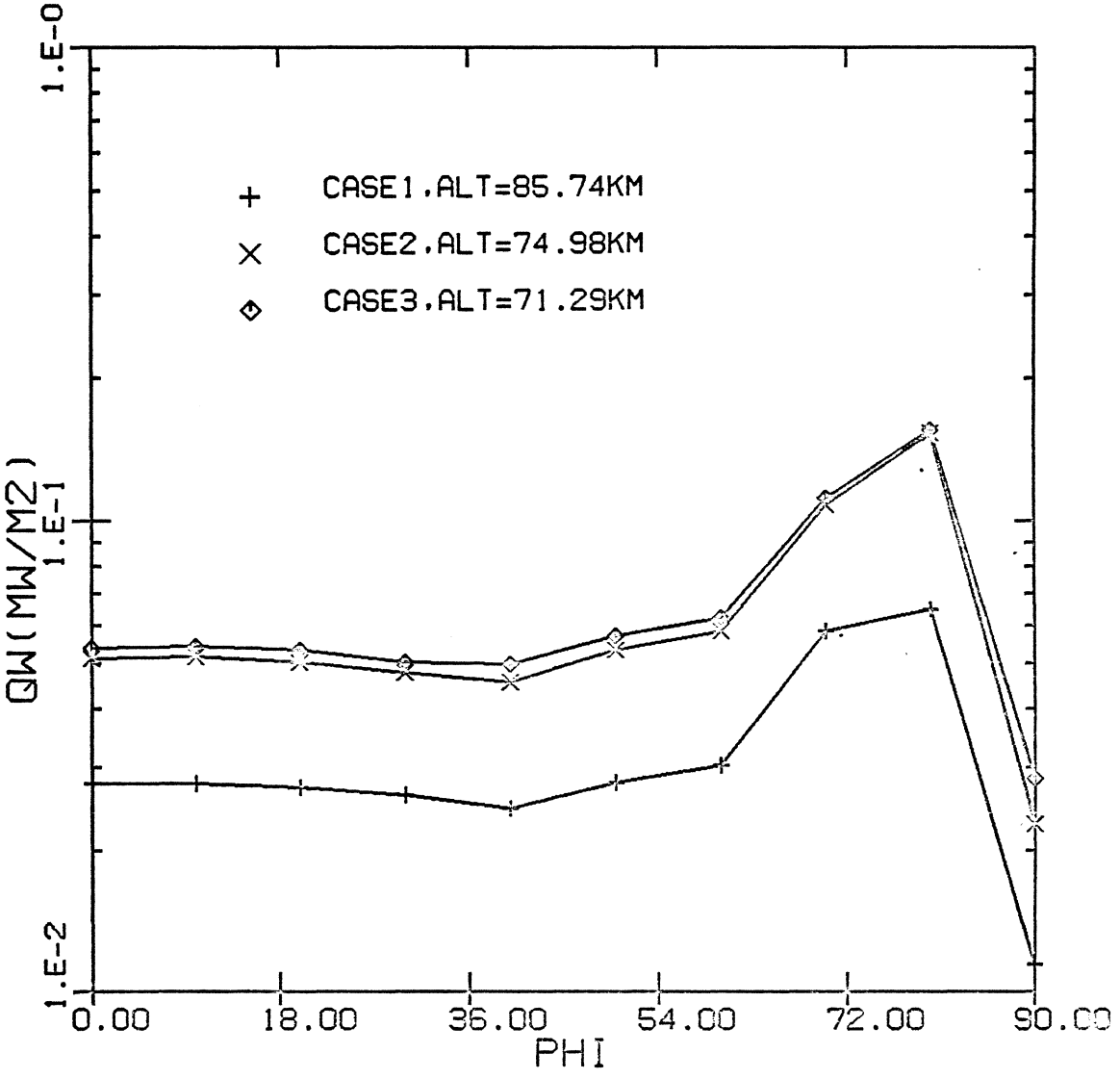

Figure 14. Spanwise heating-rate distributions for three test cases with noncatalytic wall at z/L = 0.7

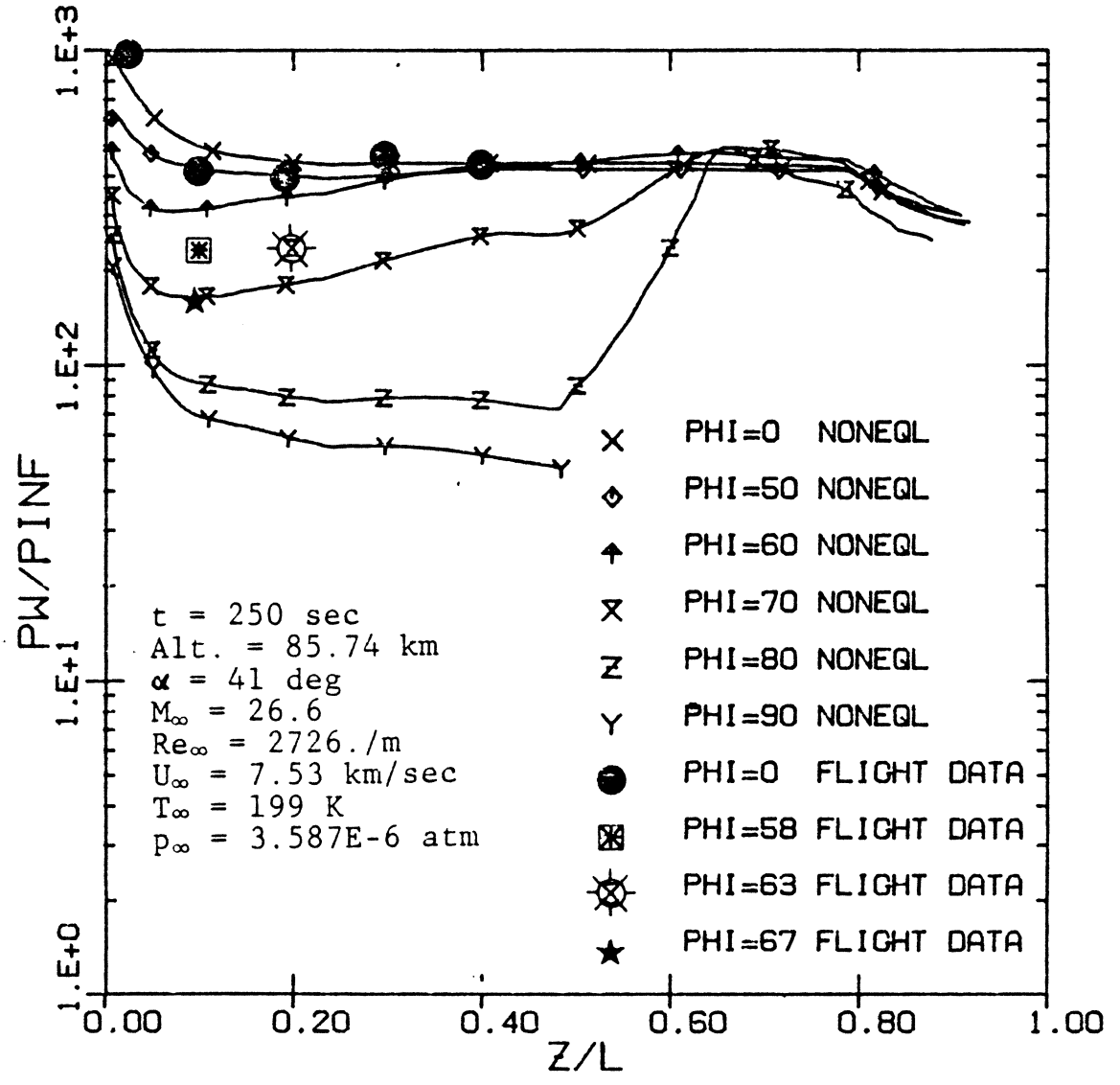

Figure 15. Comparison of surface pressure along the body with flight data for Case 1

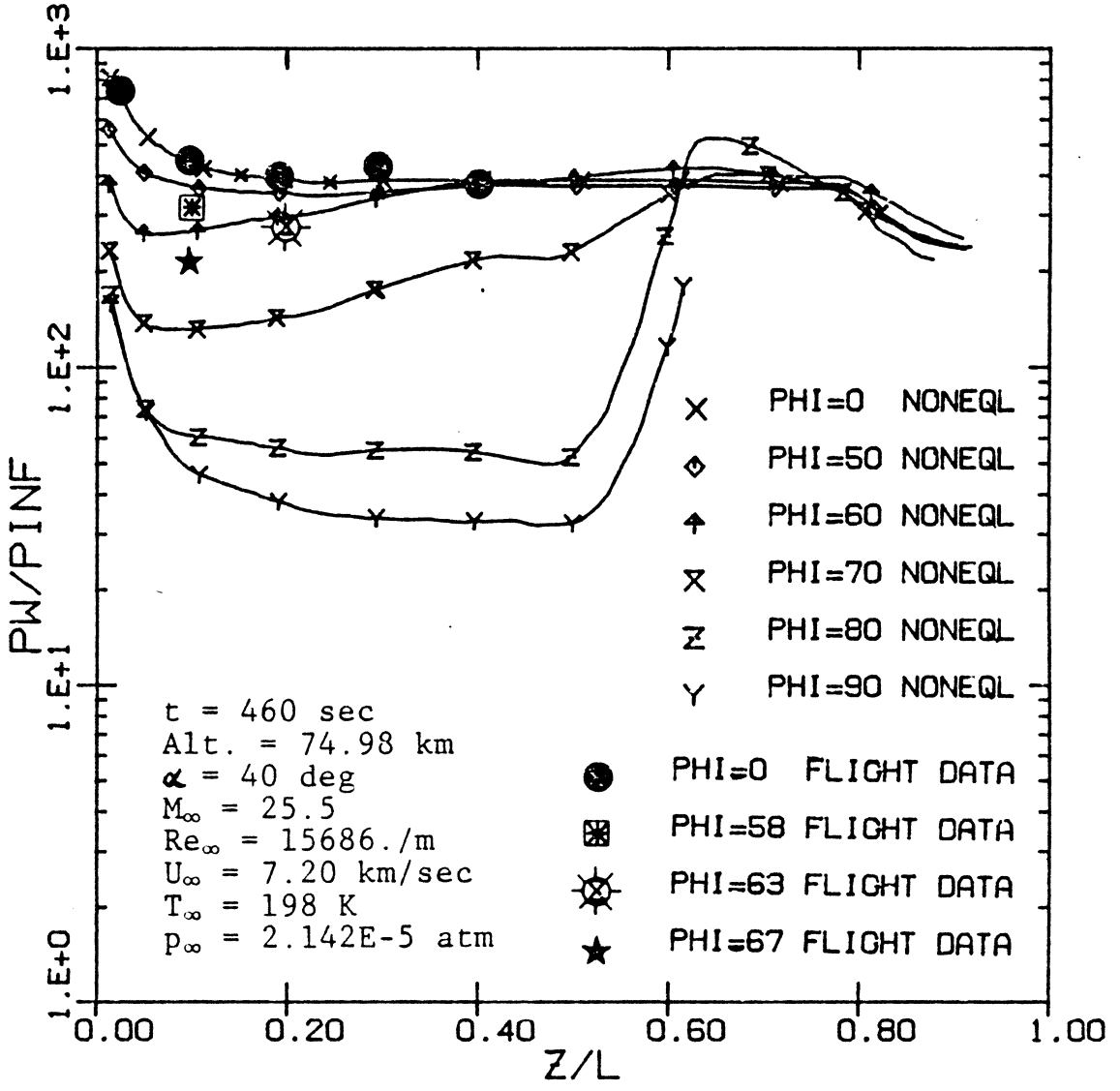

Figure 16. Comparison of surface pressure along the body with flight data for Case 2

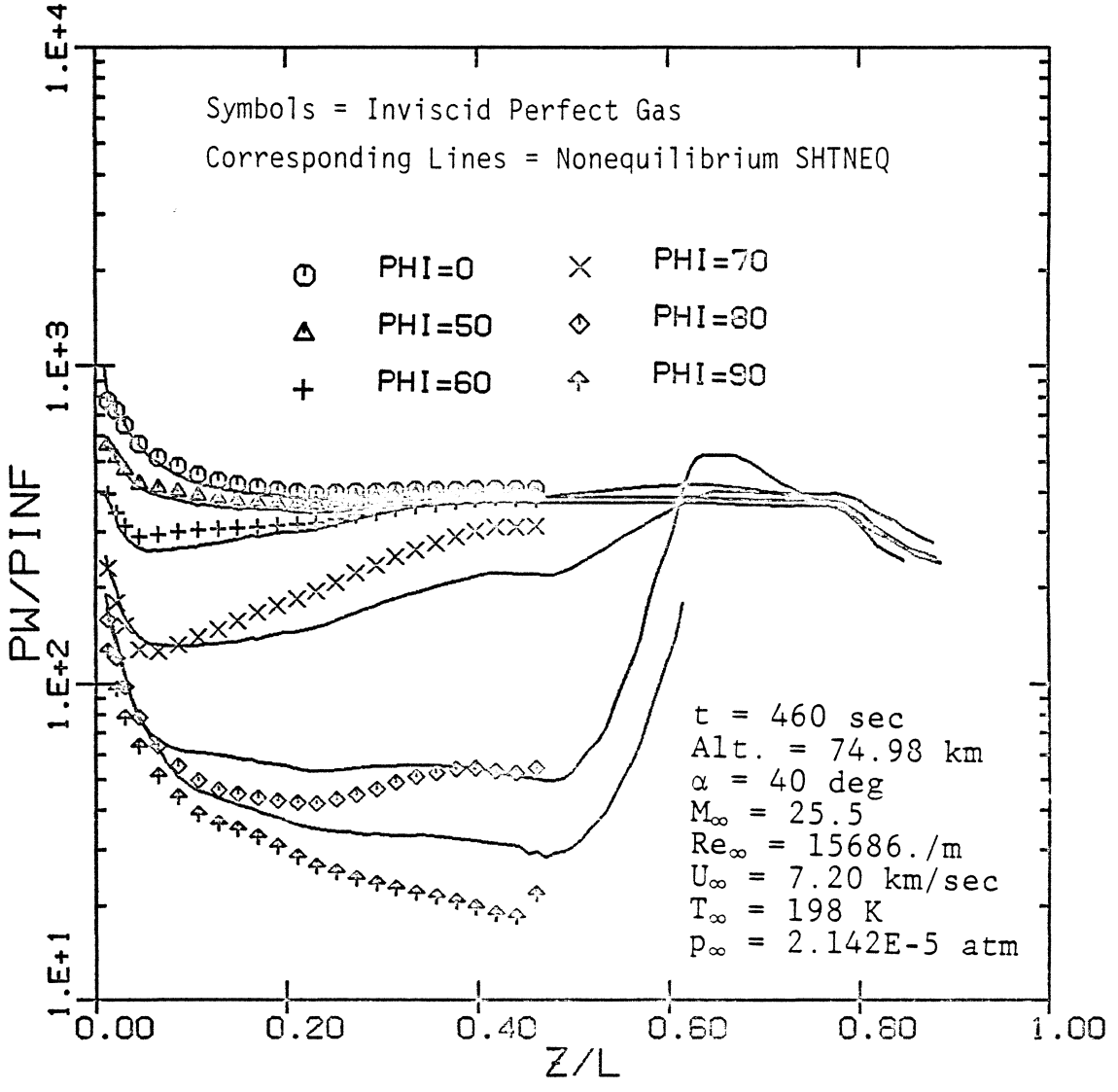

Figure 17. Comparison of surface pressure along the body with inviscid HALIS results for Case 2

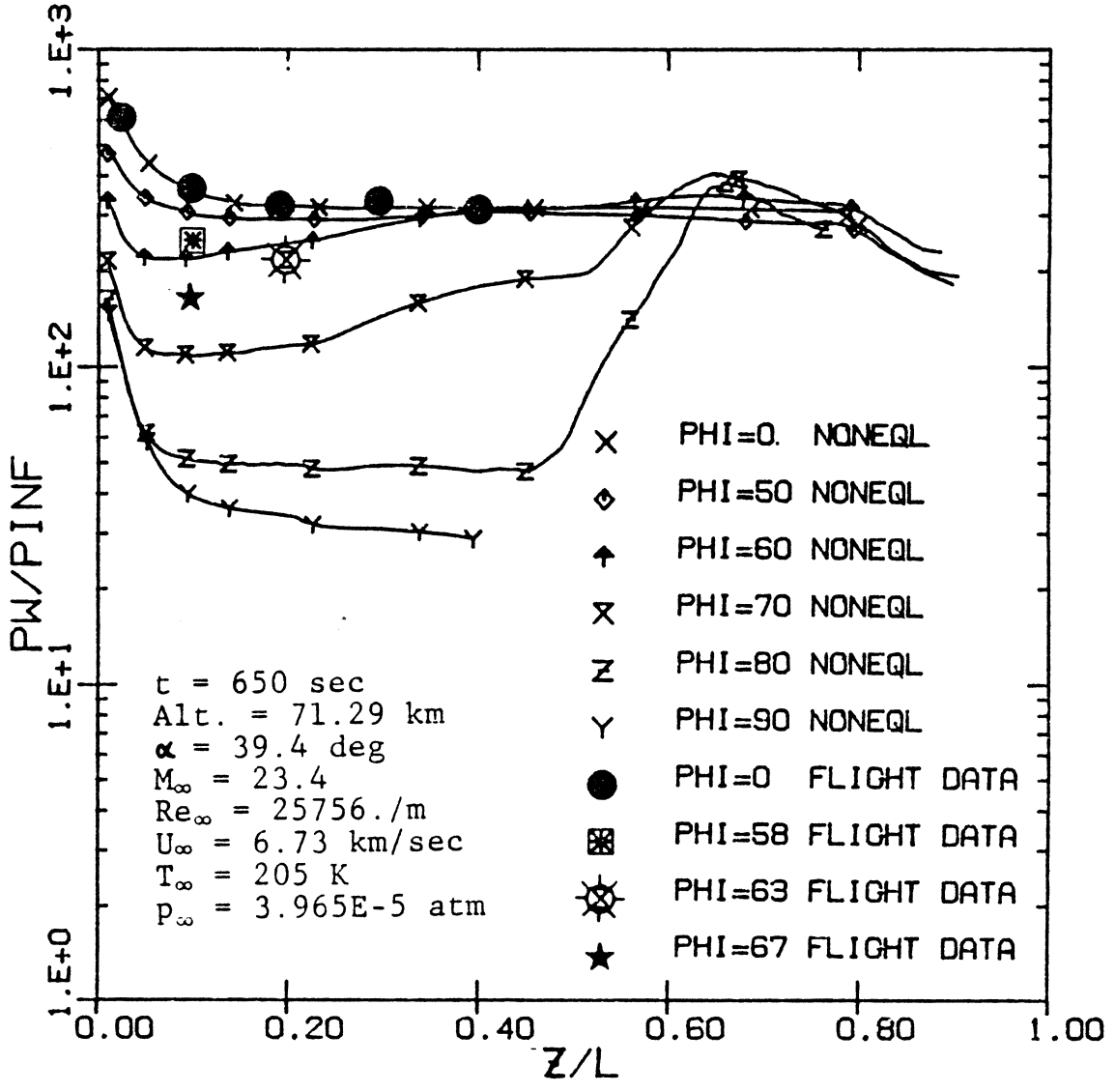

Figure 18. Comparison of surface pressure along the body with flight data for Case 3

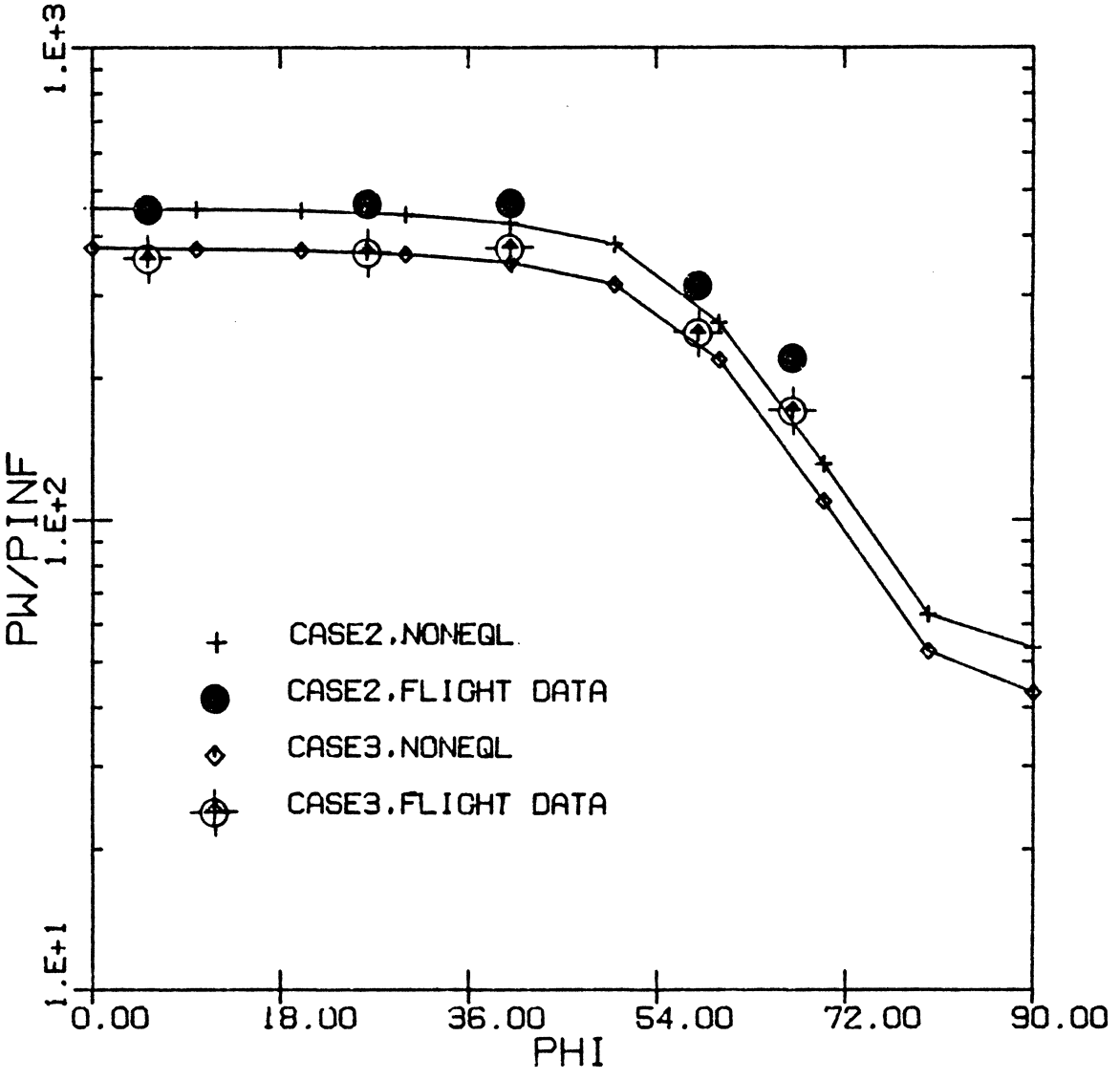

Figure 19. Comparison of surface pressure around the body with flight data at z/L = 0.1

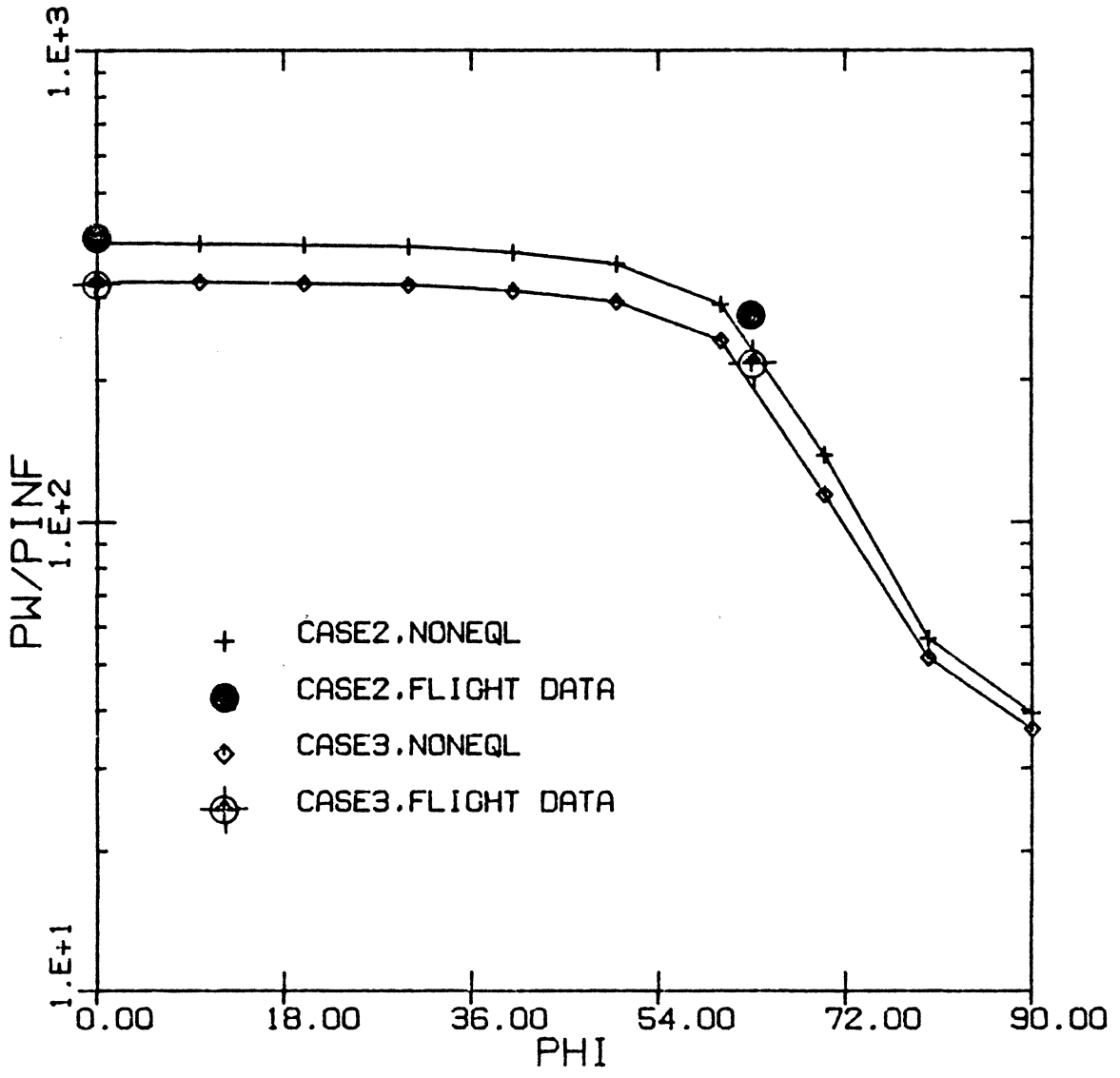

Figure 20. Comparison of surface pressure around the body with flight data at z/L = 0.2

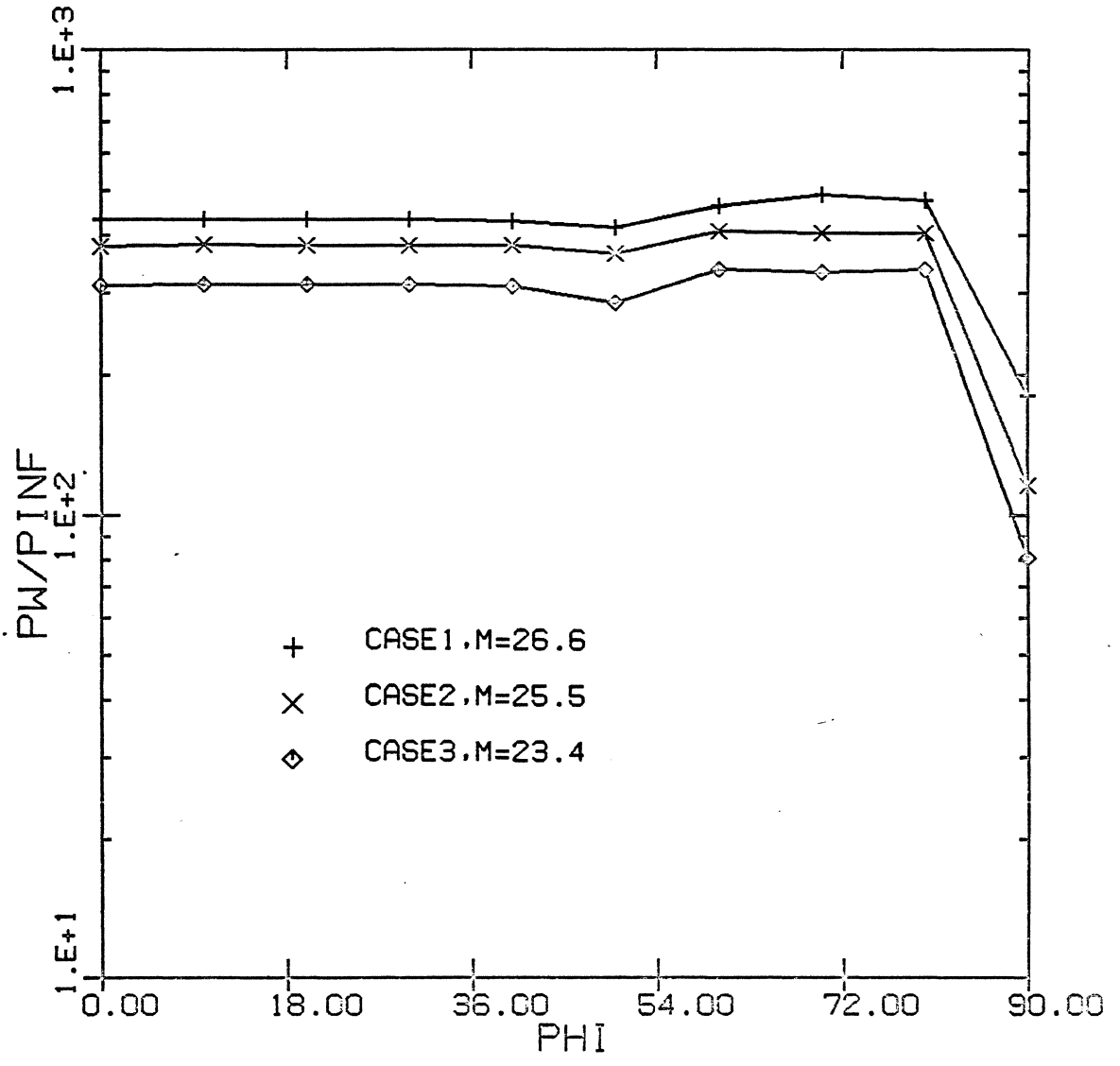

Figure 21. Surface-pressure distributions around the body for three test cases at z/L = 0.7

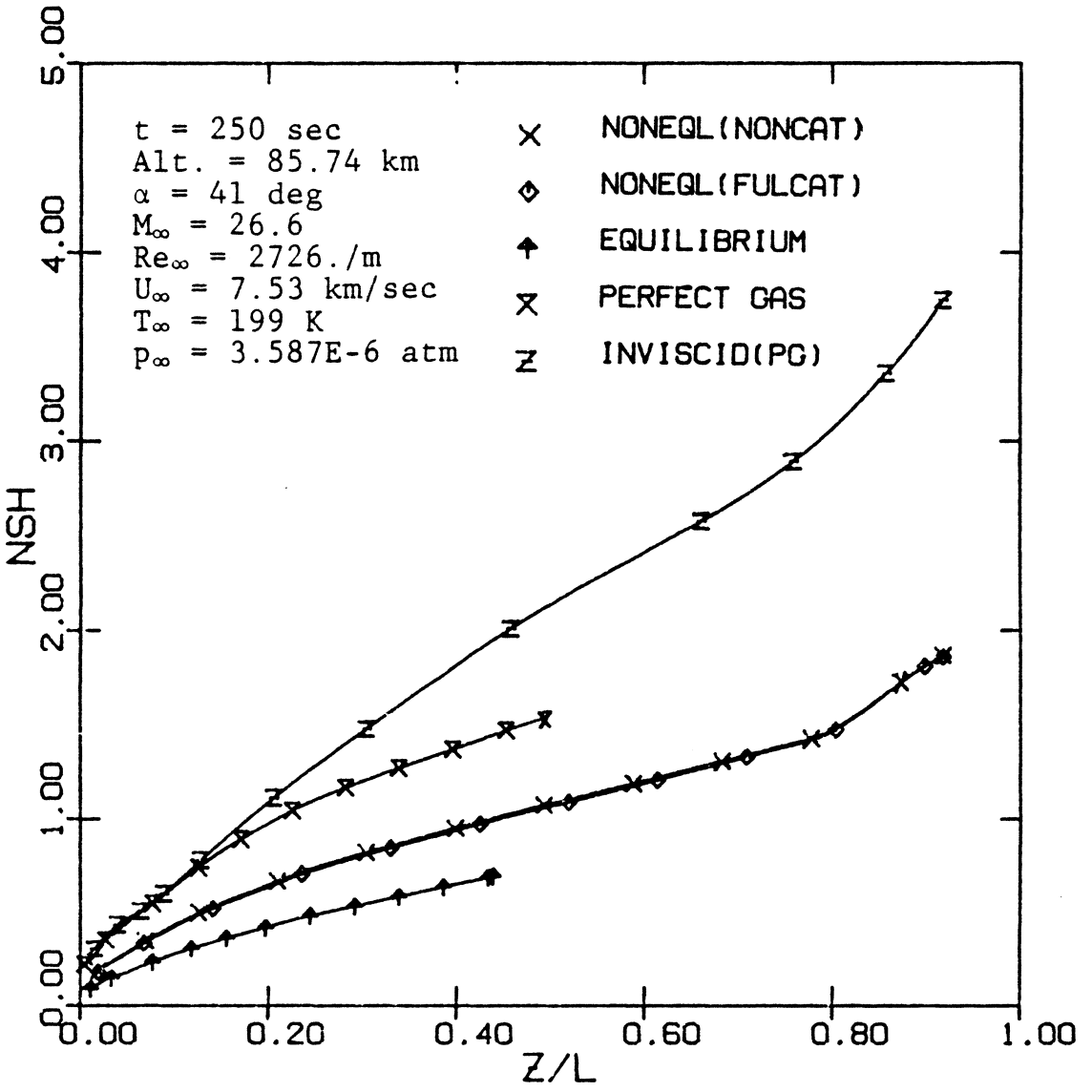

Figure 22. Comparison of globally iterated solutions of windward shock-layer thickness distribution for Case 1

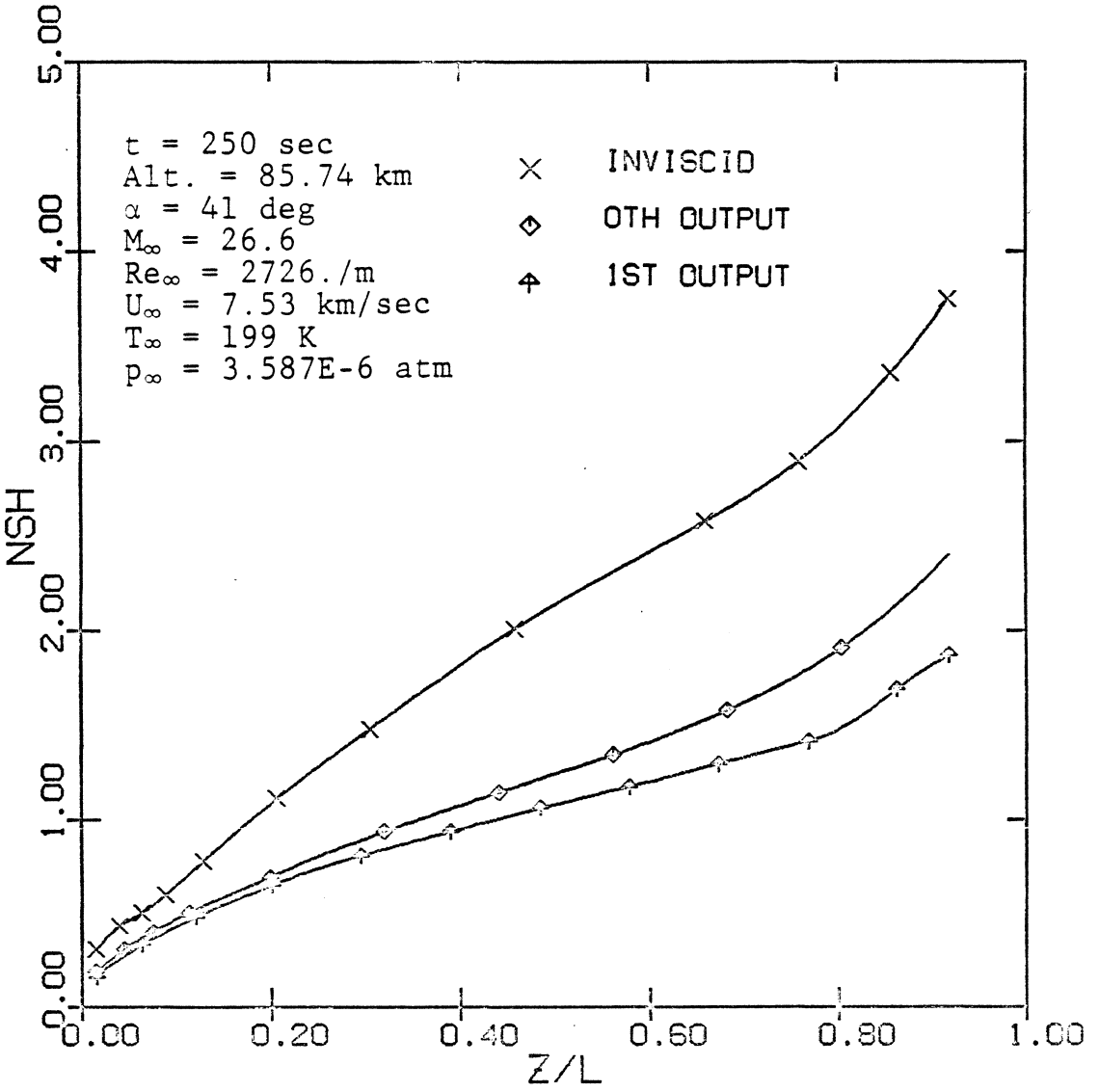

Figure 23. Effect of global iteration on shock-layer thickness distribution for Case 1

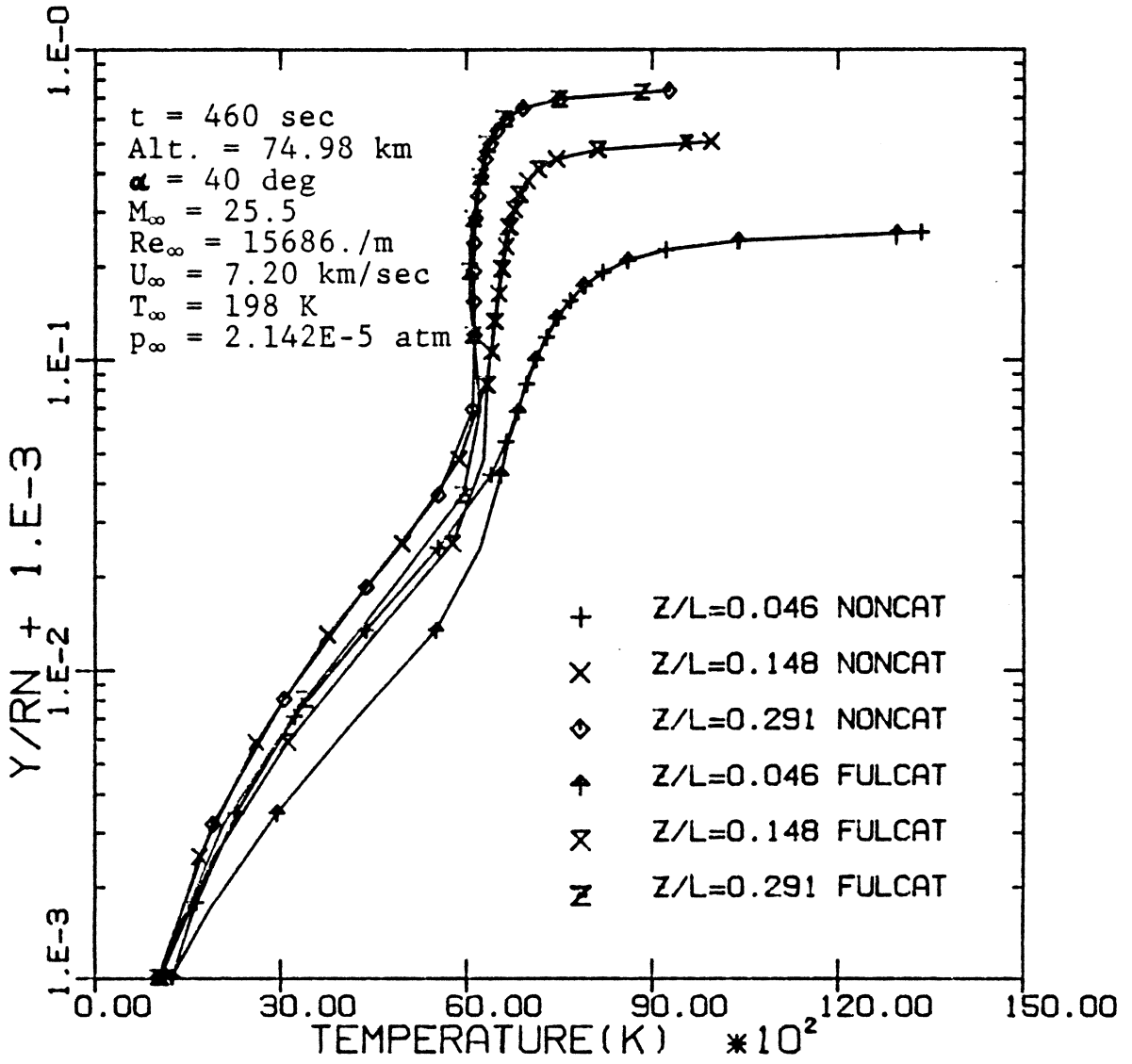

Figure 24. Shock-layer profiles of temperature at various body axial locations along windward centerline for Case 2

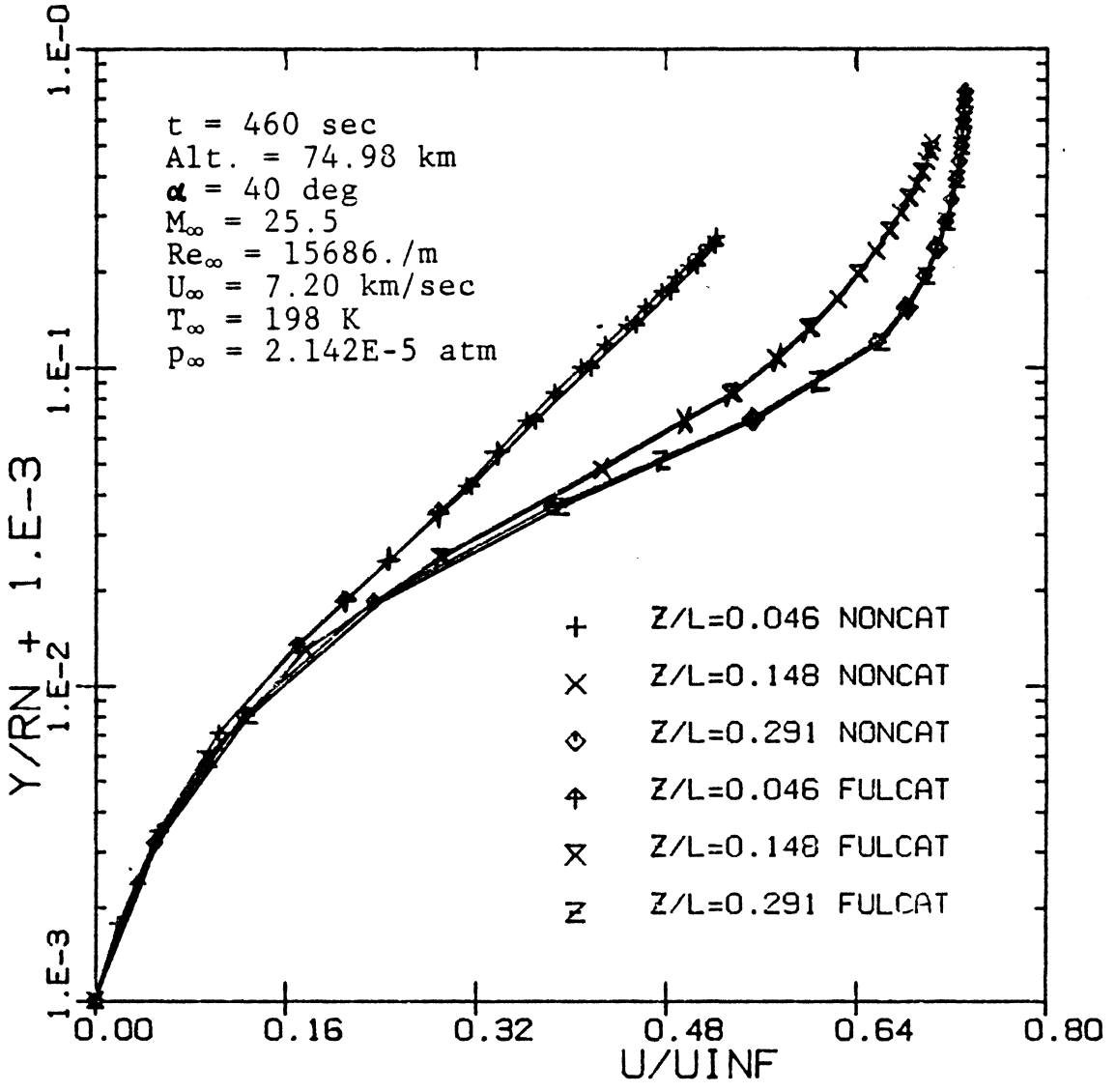

Figure 25. Shock-layer profiles of streamwise velocity at various body axial locations along windward centerline for Case 2

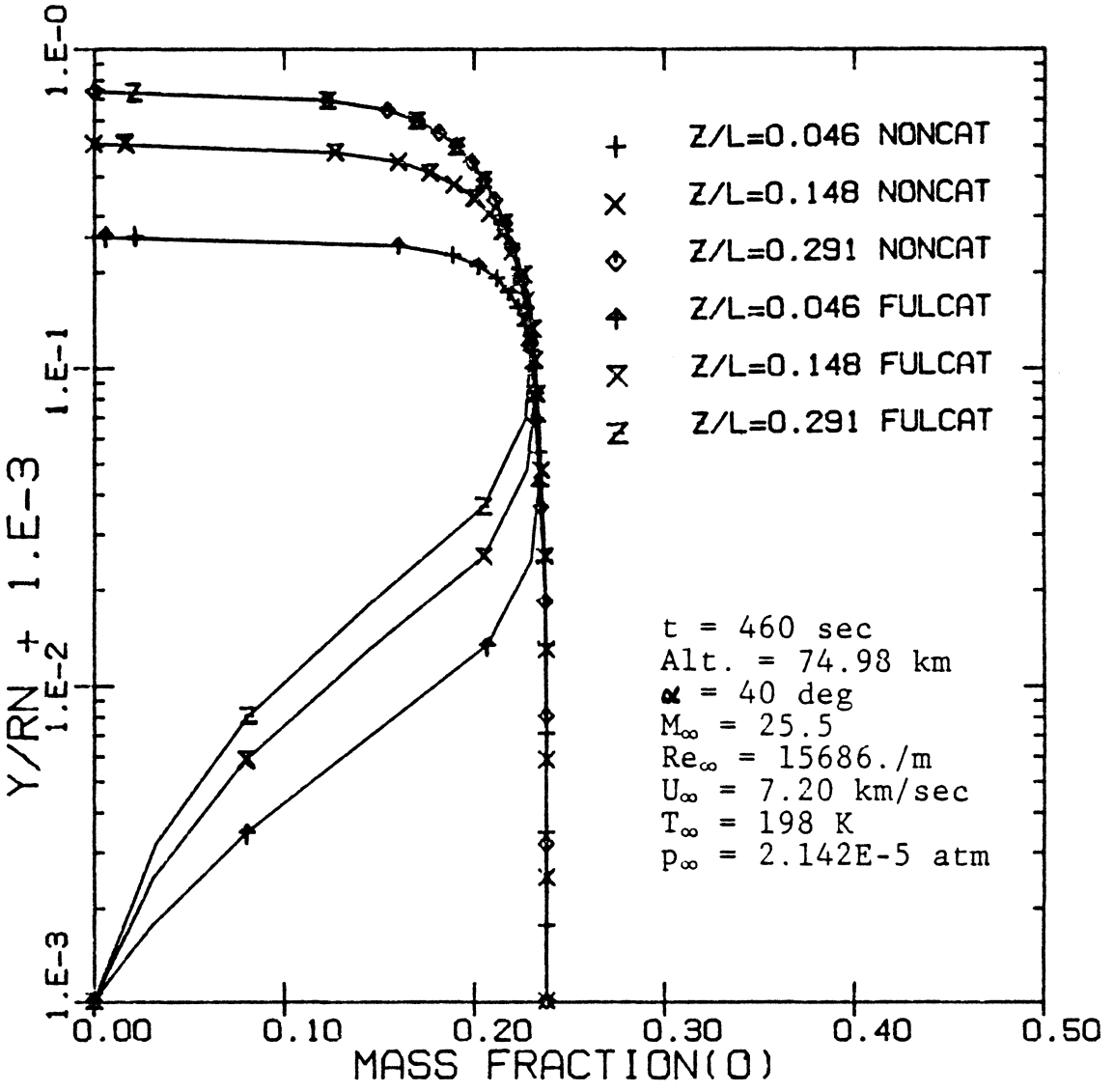

Figure 26. Shock-layer profiles of oxygen mass-fraction at various body axial locations along windward centerline for Case 2

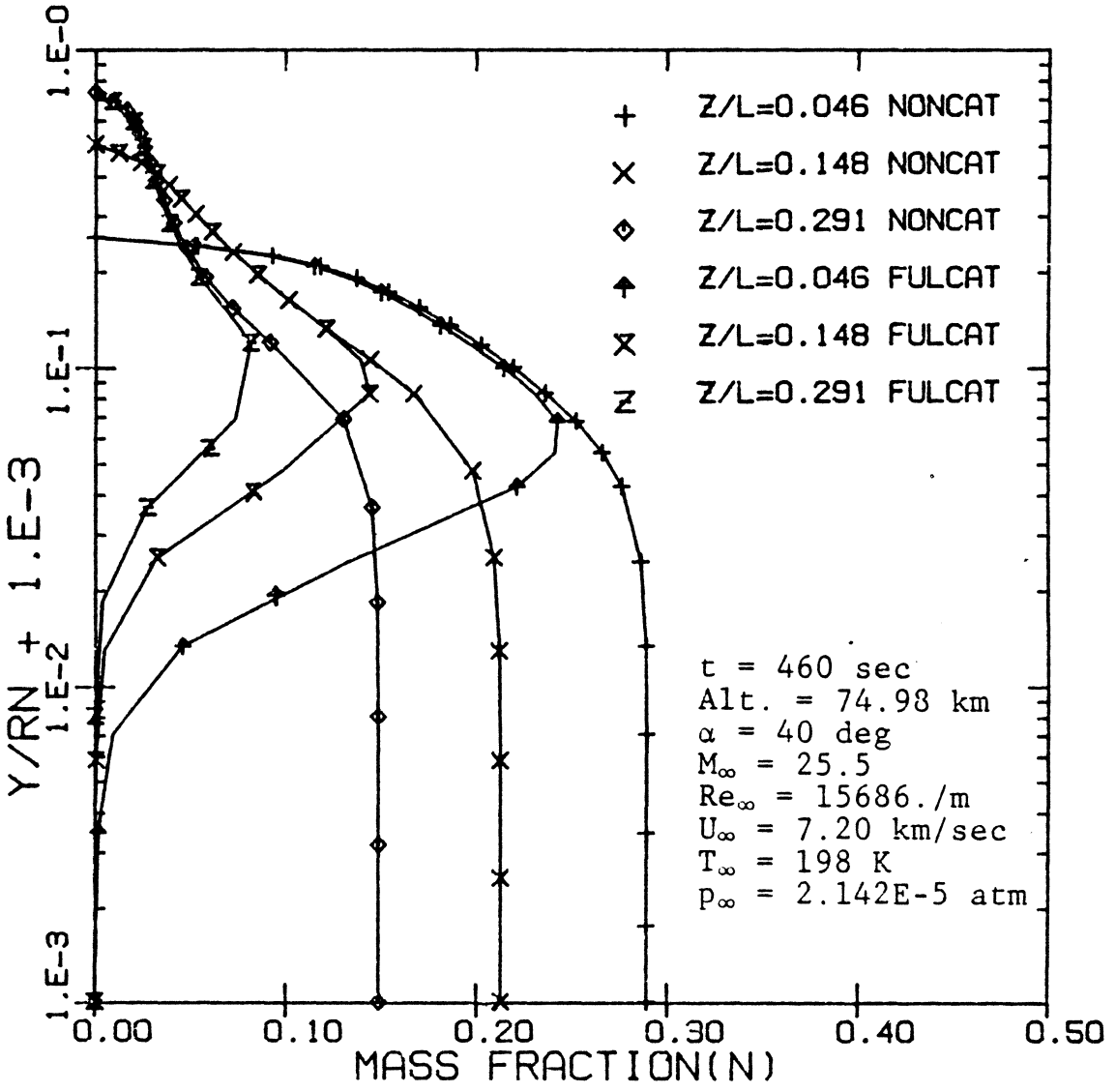

Figure 27. Shock-layer profiles of nitrogen mass-fraction at various body axial locations along windward centerline for Case 2

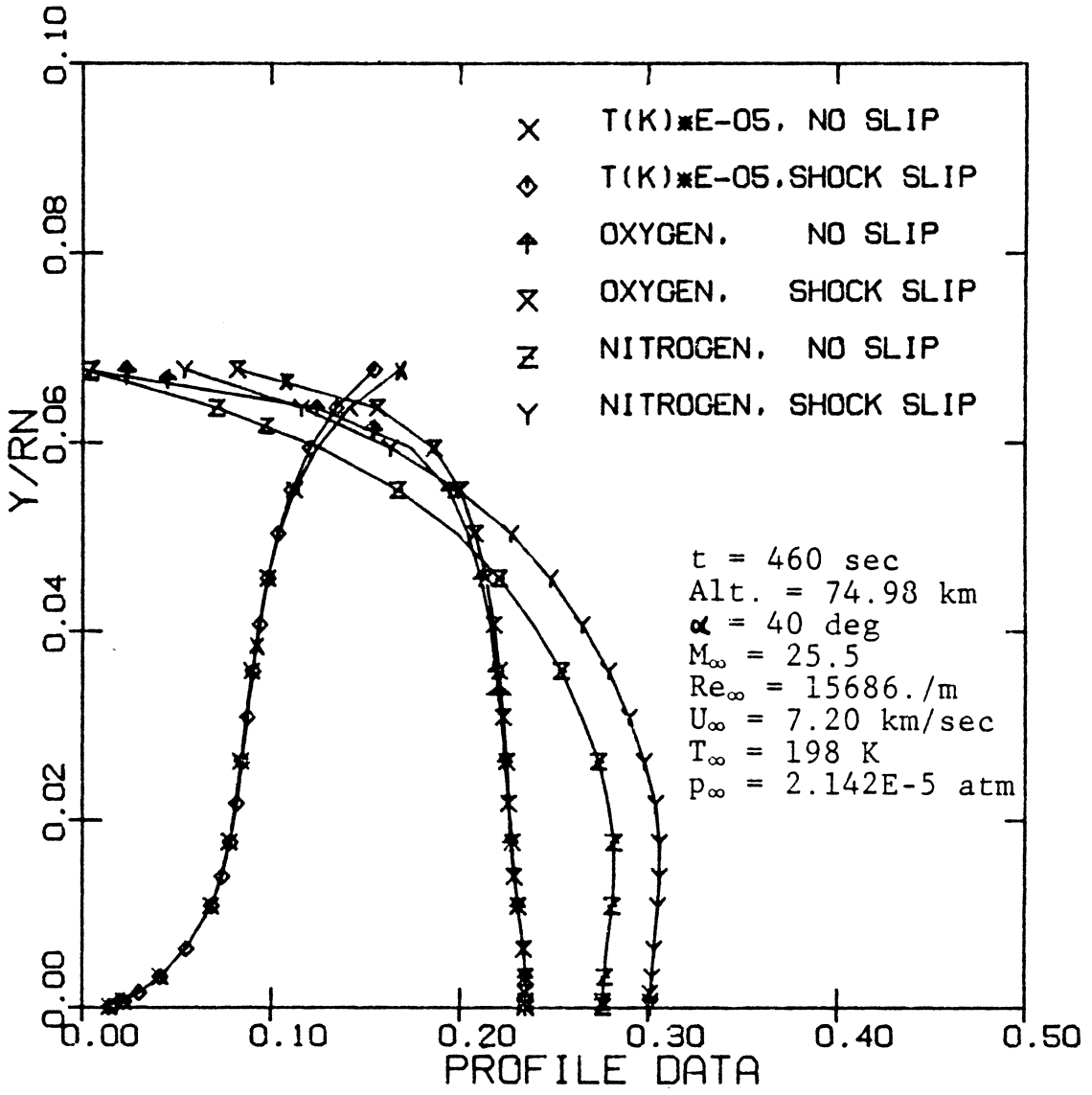

Figure 28. Shock-slip effects on the profiles of temperature and mass-fraction at stagnation point for Case 2

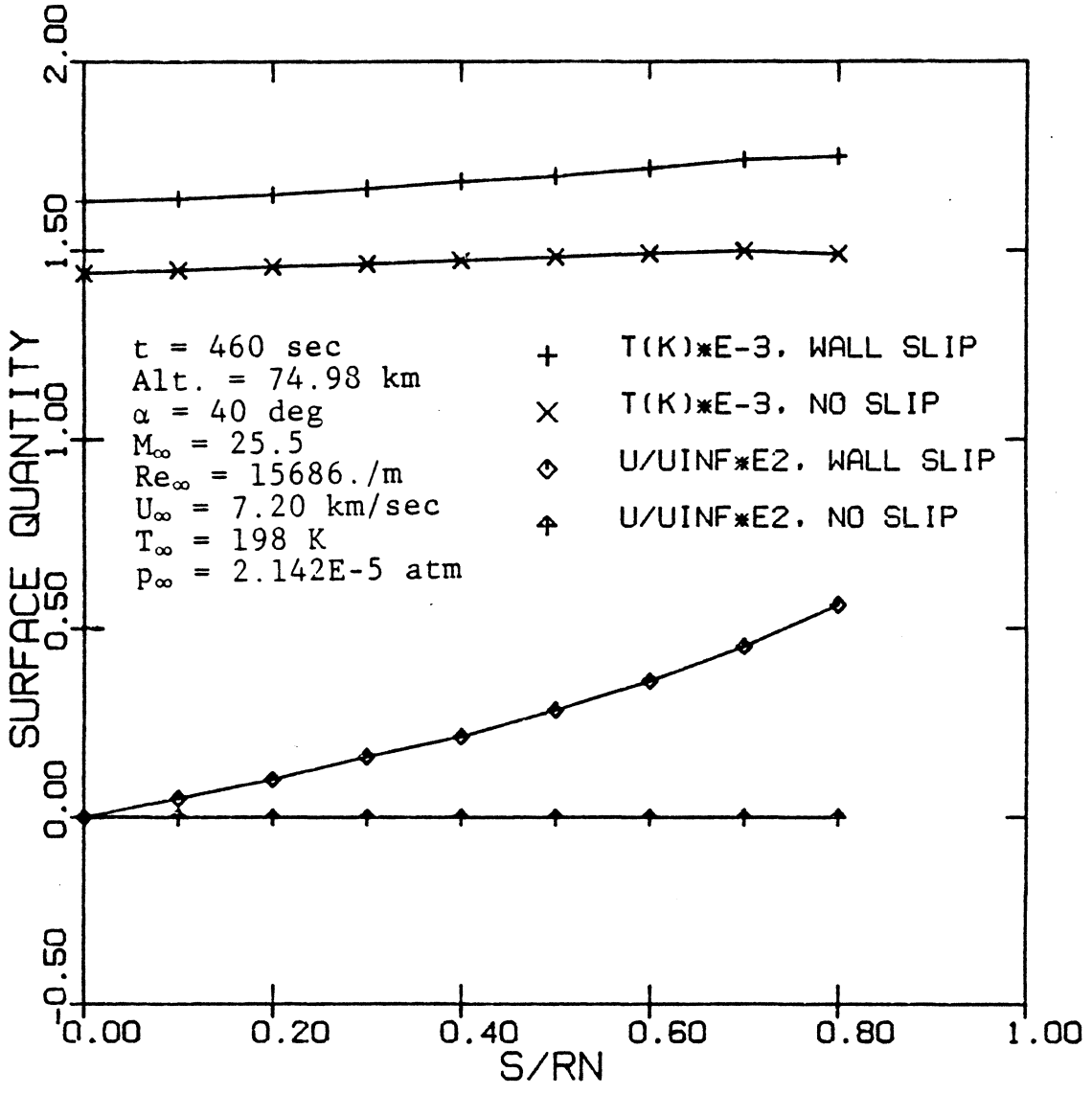

Figure 29. Wall-slip effects on velocity slip and temperature jump on the nose region of Case 2

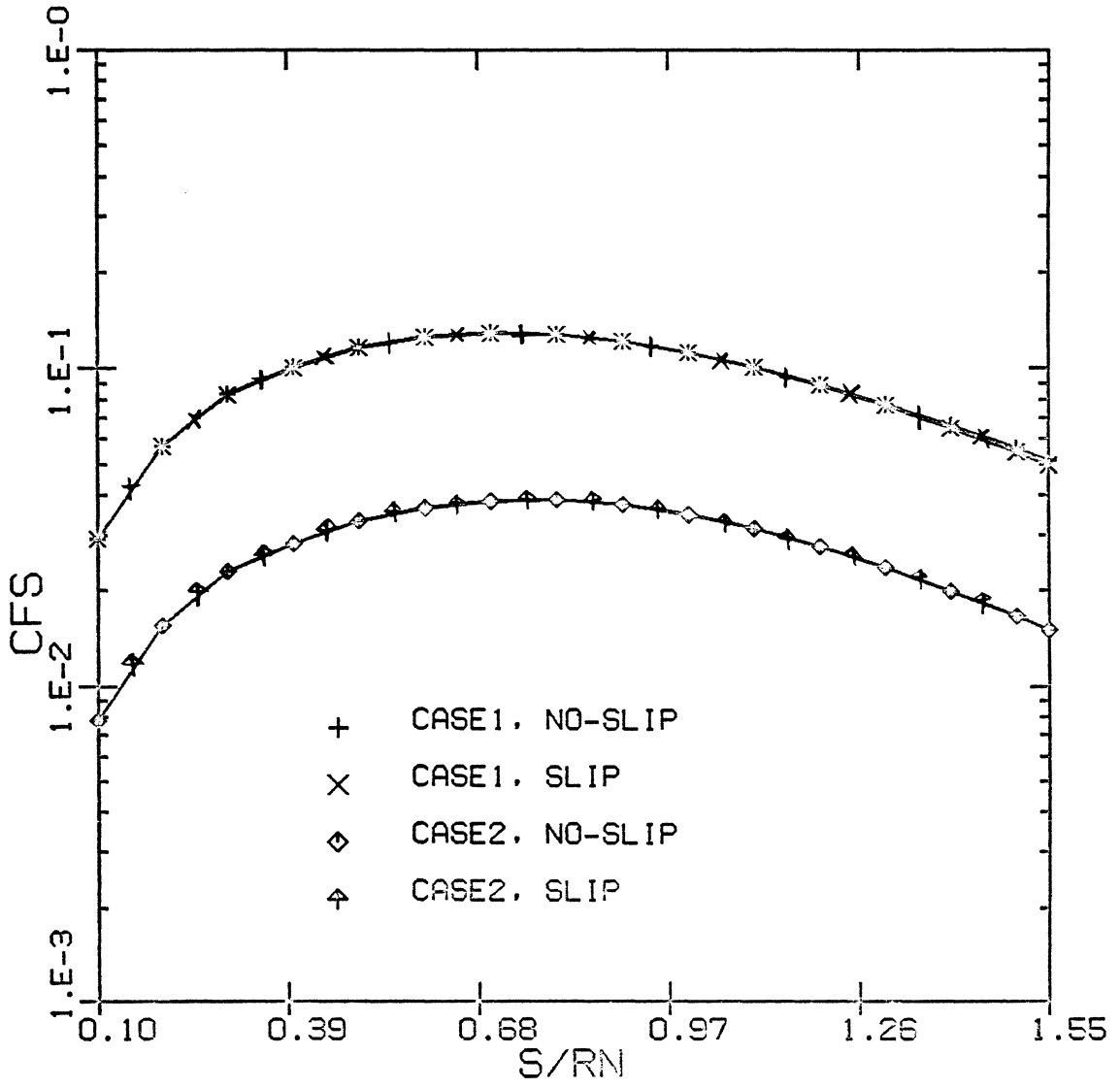

Figure 30. Wall-slip effect on skin friction over the nose for Cases 1 and 2

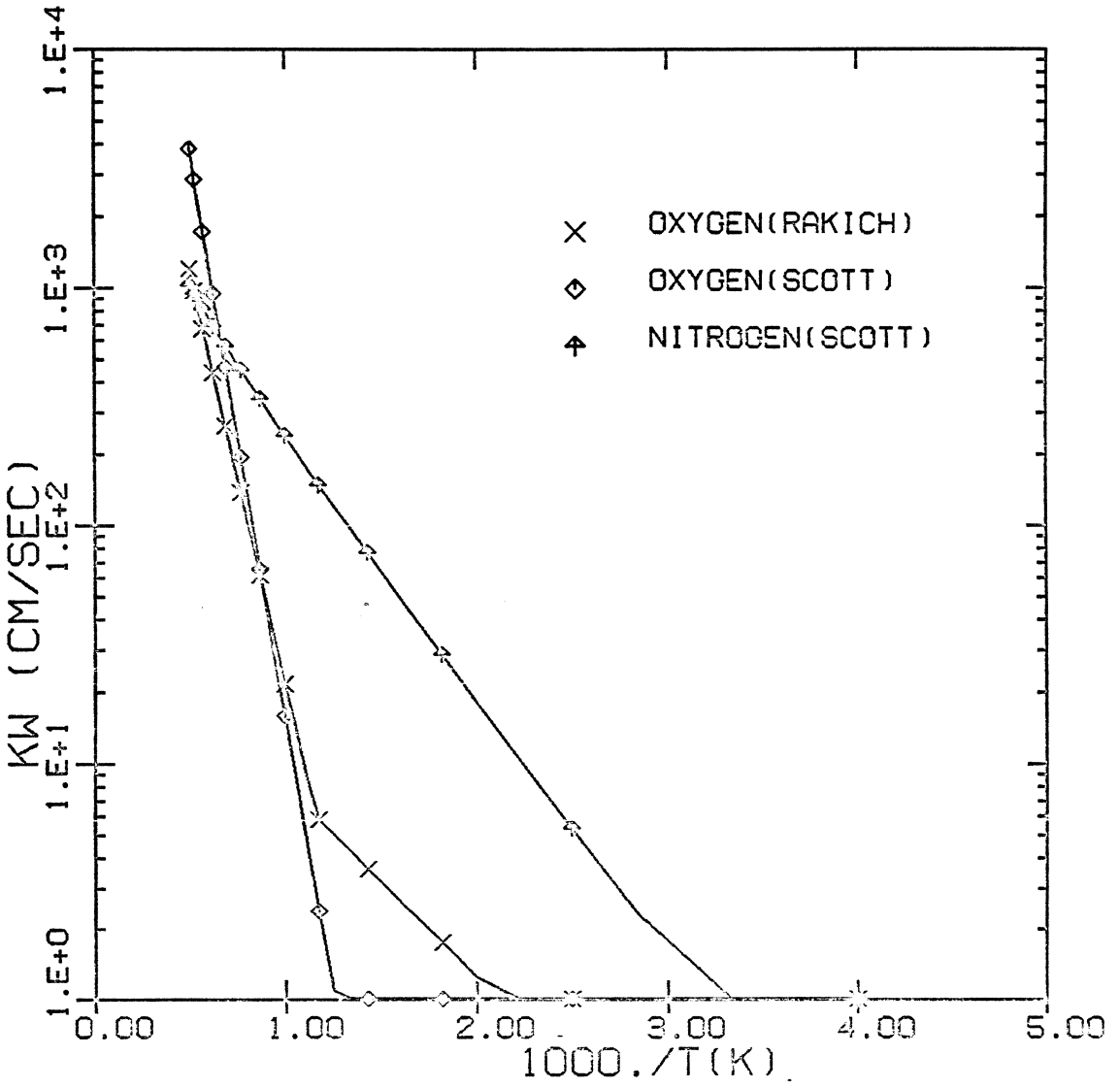

Figure 31. Data for surface catalytic recombination rates for oxygen and nitrogen atoms

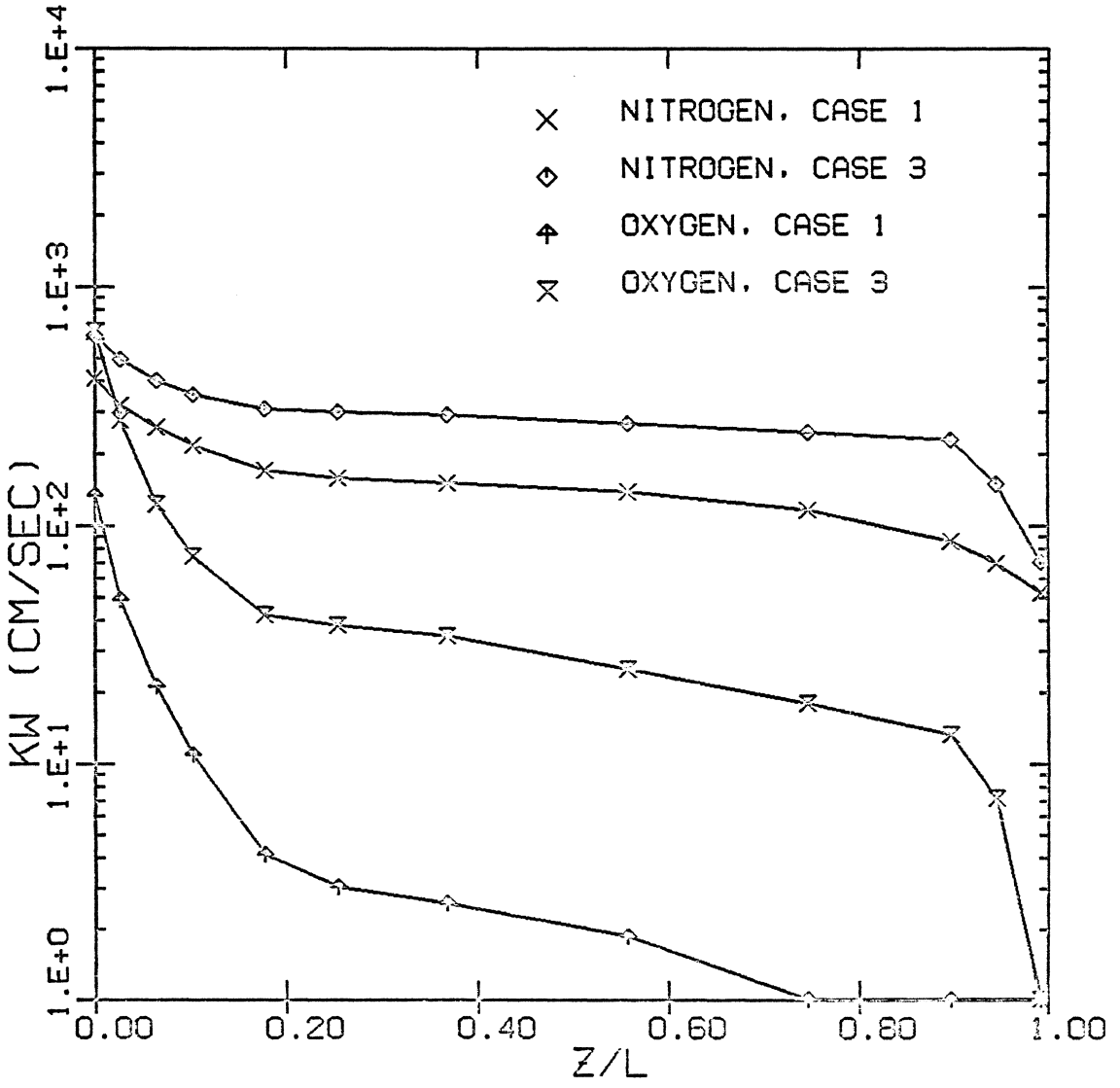

Figure 32. Distributions of surface catalytic recombination rates along the body using Scott's relation

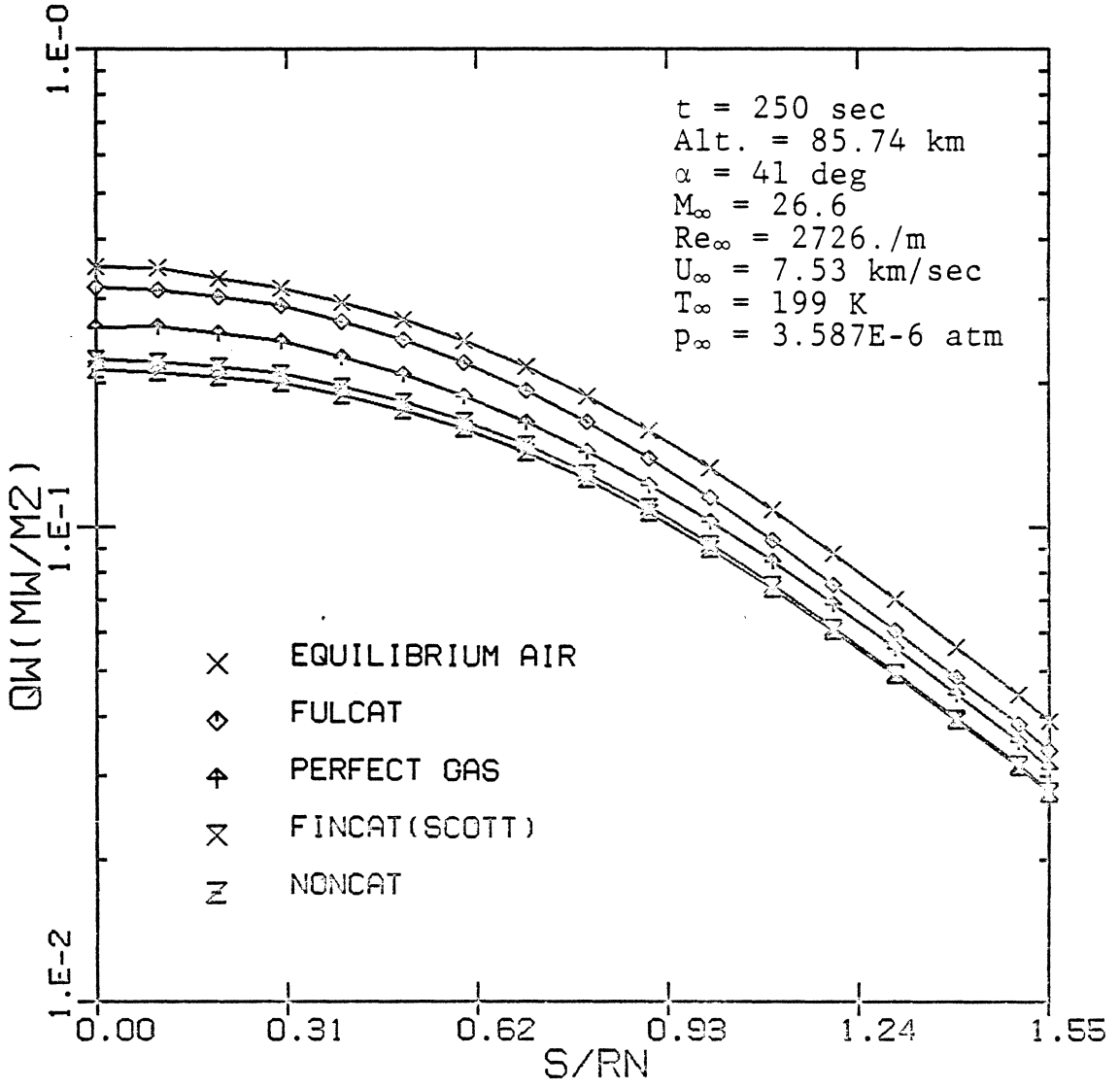

Figure 33. Heating rates over the nose for various surface catalysis for case 1

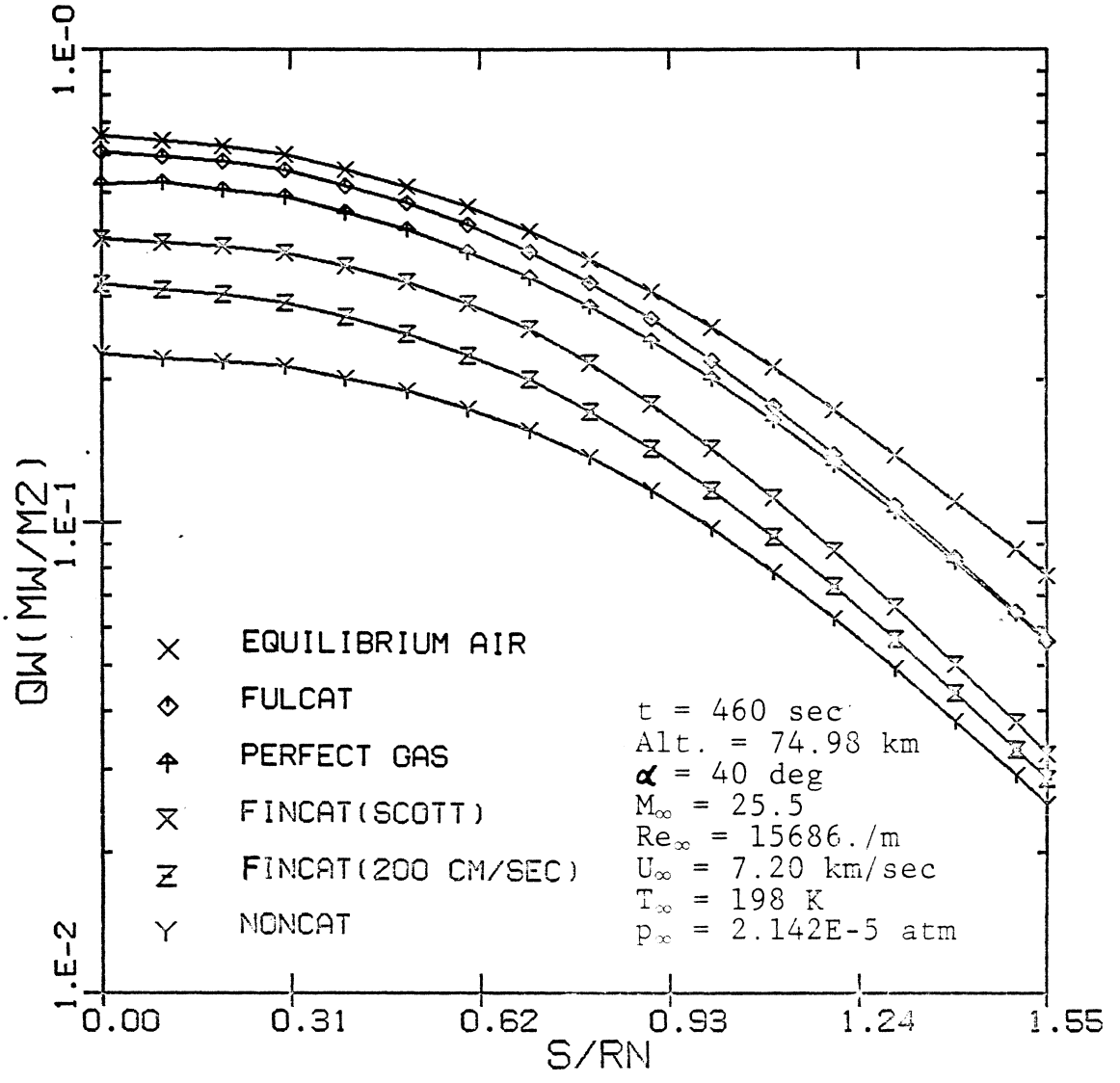

Figure 34. Heating rates over the nose for various surface catalysis for case 2

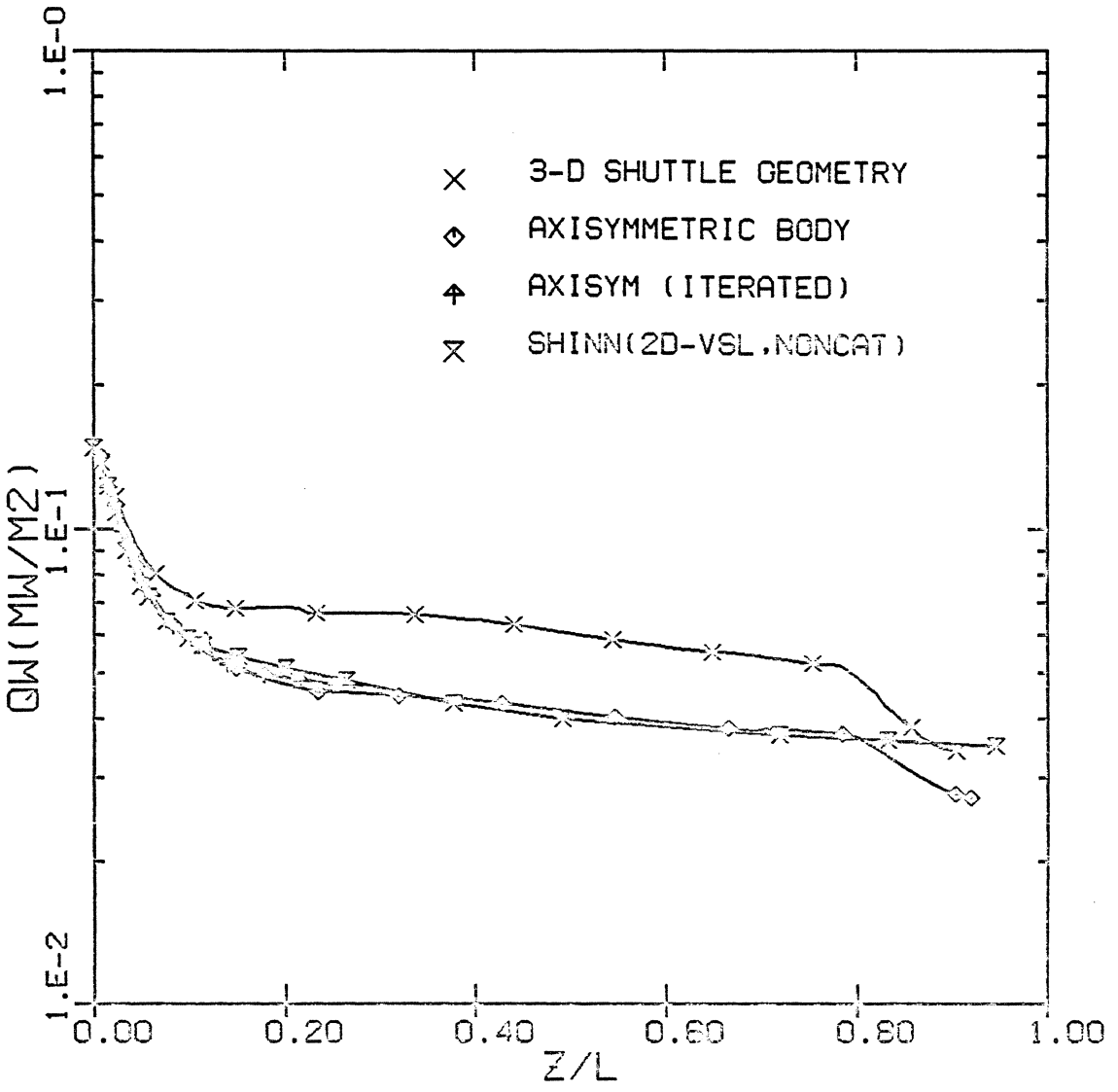

Figure 35. Heating-rate comparison with the equivalent axisymmetric body concept for Case 3

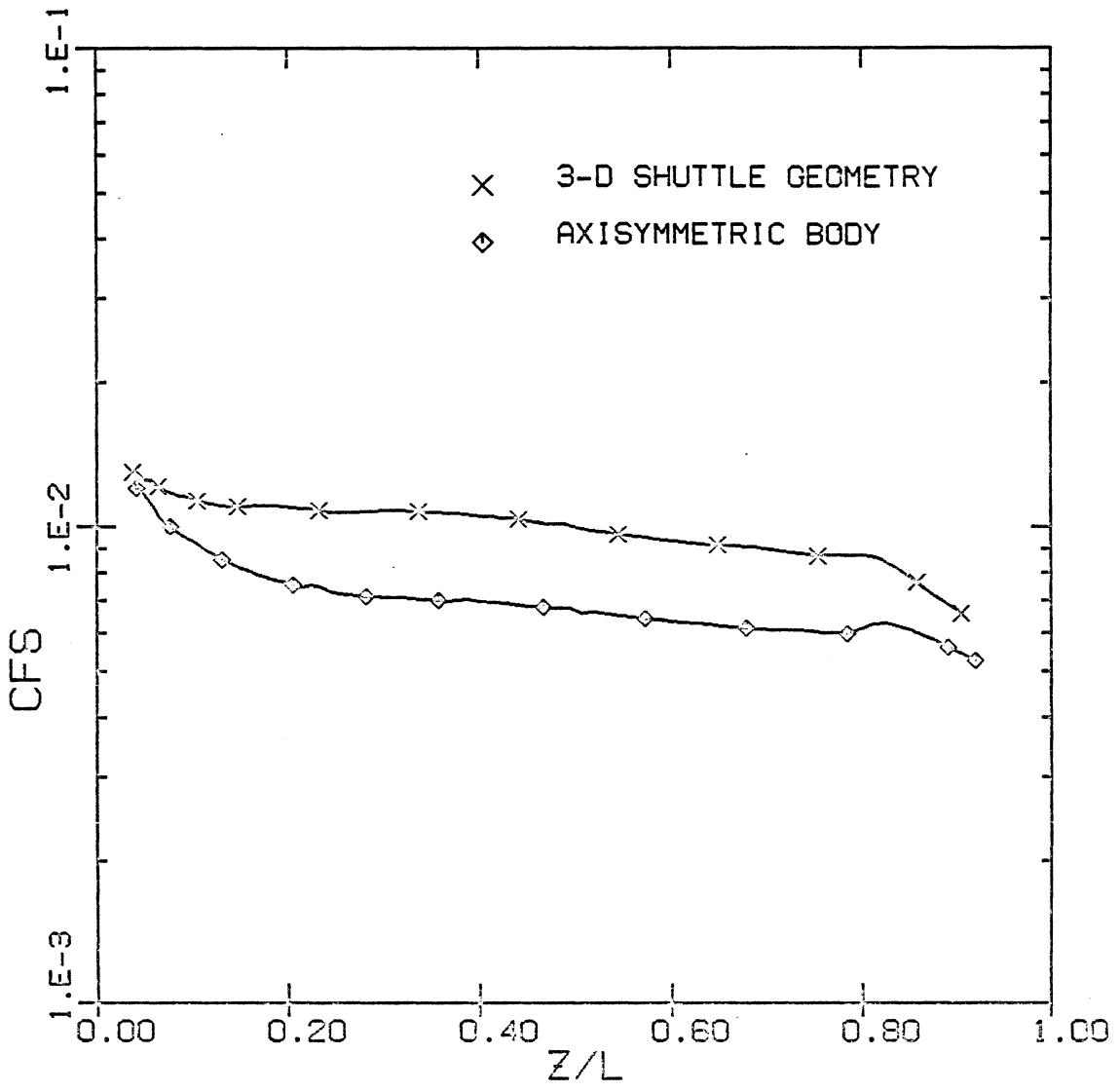

Figure 36. Skin-friction comparison with the equivalent axisymmetric body concept for Case 3

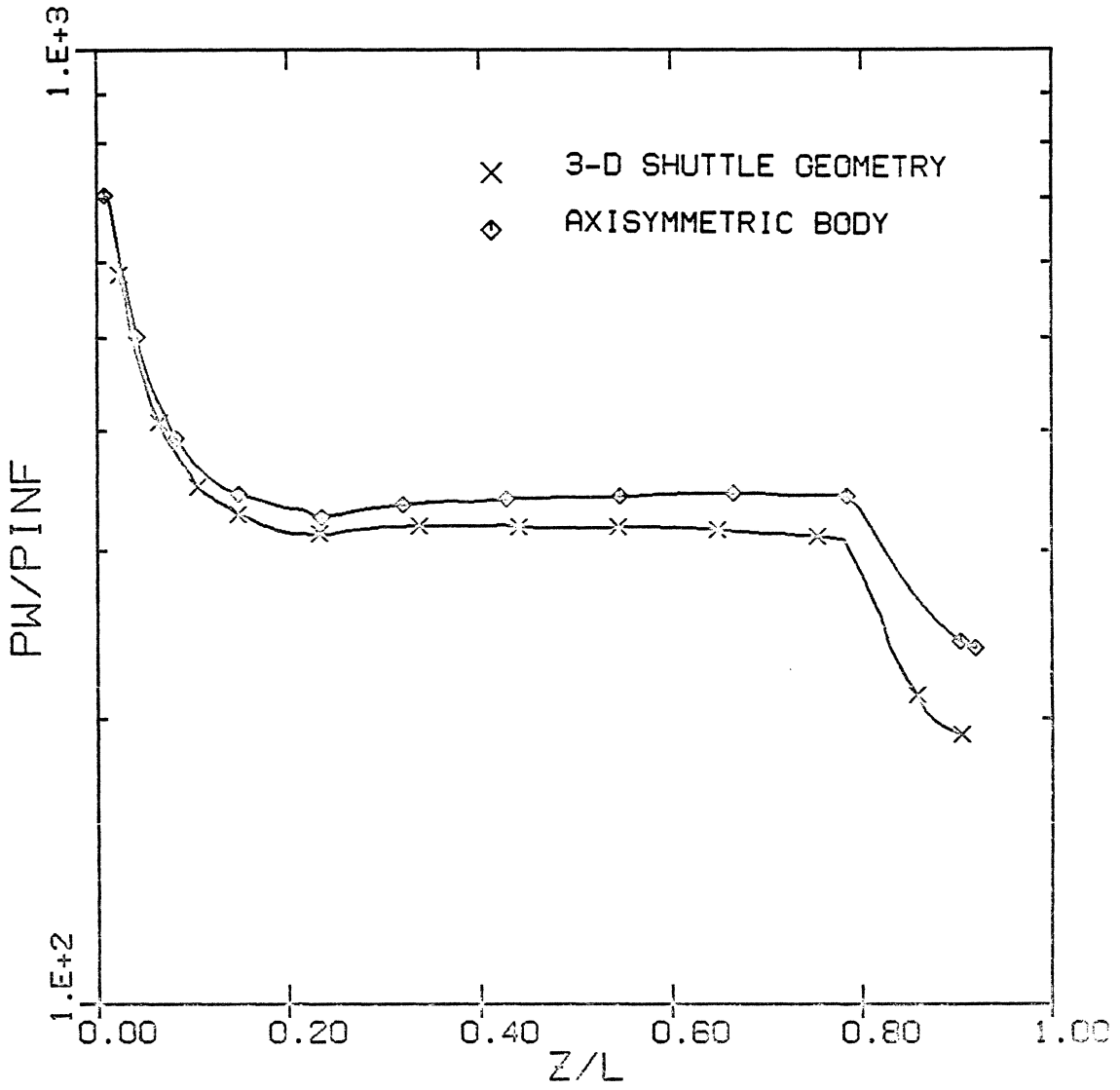

Figure 37. Surface-pressure comparison with the equivalent axisymmetric body concept for Case 3

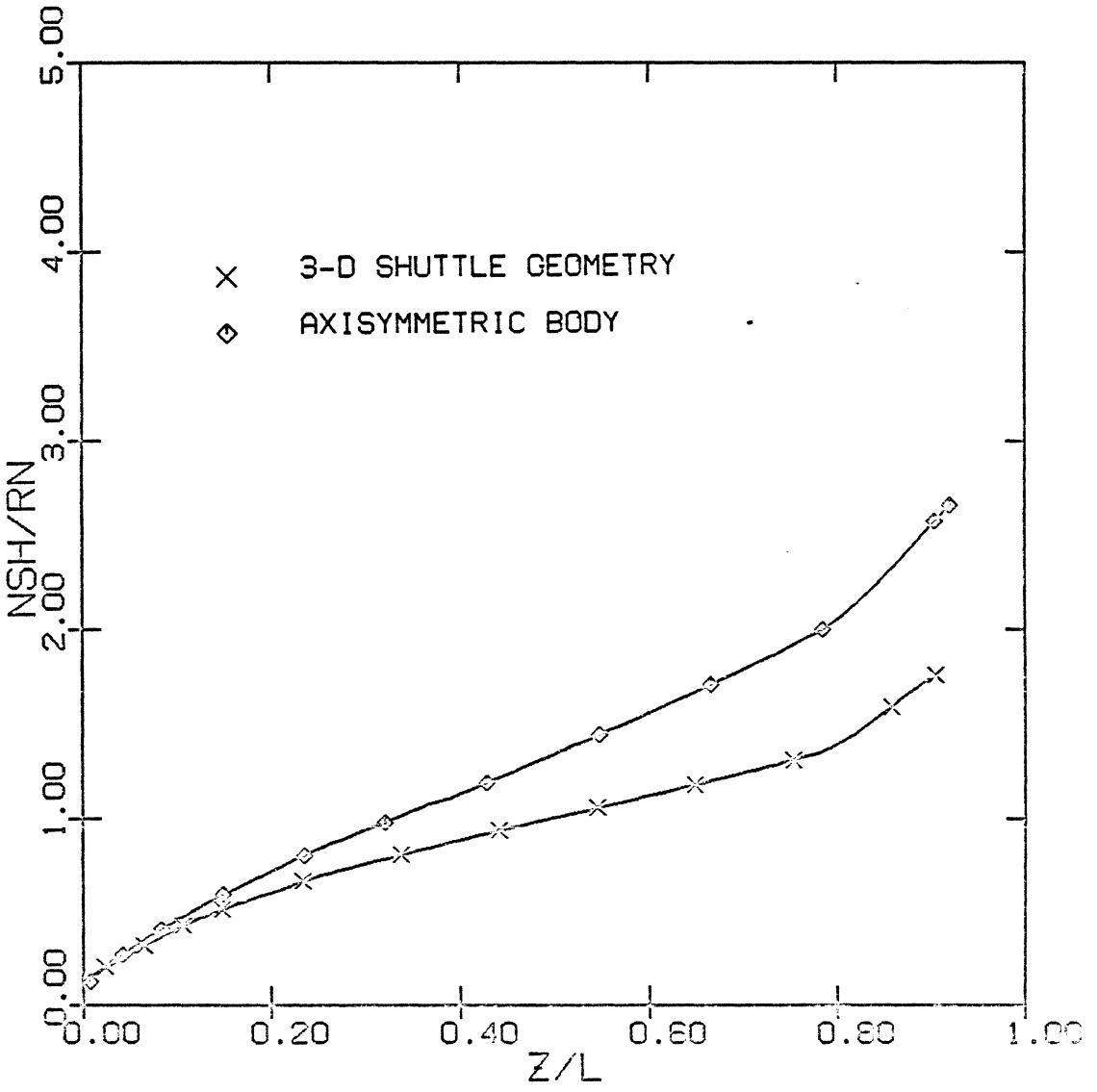

Figure 38. Shock-layer thickness comparison with the equivalent axisymmetric body concept for Case 3

The vita has been removed from the scanned document